UNIVERSITÀ DEGLI STUDI DI PADOVA

UNIVERSITÀ DEGLI STUDI DI PADOVA

Dipartimento di Ingegneria Industriale DII
Corso di Laurea Magistrale in Ingegneria dell'Energia Elettrica

Studies on the application of MMC technology to the Acceleration Grid Power Supply of the Neutral Beam Injector of DTT

Relatore:
Prof. Paolo Bettini

Correlatore:
Ing. Alberto Ferro

Studente:
Francesco Santoro
Matricola 1197575

Anno Accademico 2020/2021

Sommario

Il Divertor Test Tokamak (DTT) è un impianto sperimentale di fusione nucleare a confinamento magnetico che verrà realizzato presso il Centro Ricerche ENEA di Frascati (Roma), con l'obiettivo di testare differenti tipologie di divertore in condizioni fisiche e tecniche che possono essere estrapolate accuratamente per DEMO e altri futuri tokamak. La gestione dell'elevatissimo flusso termico sui materiali a contatto con il plasma è uno tra i principali problemi da risolvere in vista della realizzazione di reattori a fusione come DEMO.

Per poter raggiungere le condizioni necessarie per operare con parametri simili a DEMO, DTT avrà bisogno di una notevole potenza di riscaldamento del plasma, fornita da sistemi di riscaldamento addizionali, tra cui sistemi a radiofrequenza e ad iniezione di fasci di particelle neutre (Neutral Beam Injection, NBI). L'iniettore di particelle neutre che utilizzerà DTT accelererà fino a 500 keV una corrente di circa 40 A di ioni negativi di deuterio, per una potenza iniettata al plasma di 10 MW. L'accelerazione degli ioni negativi avviene in tre stadi, ciascuno composto da una griglia accelerante posta ad una tensione crescente con incrementi di -167 kV. Una volta accelerati, gli ioni vengono neutralizzati per poi proseguire nella loro traiettoria diretti al plasma. Durante l'operazione degli iniettori sono frequenti perdite di isolamento tra le griglie con conseguenti scariche (breakdown).

L'NBI necessita di un dedicato sistema di alimentazione elettrico per le tre griglie acceleranti (Acceleration Grid Power Supply, AGPS). L'AGPS deve fornire 500 kV in tre stadi da 167 kV; è dimensionato per una corrente nominale di circa 70 A. La tensione DC deve poter essere regolata almeno dal 20% al 100% del valore nominale. Il convertitore deve essere in grado all'avviamento di raggiungere il 90% del valore nominale entro 80 ms. Dal punto di vista dell'alimentatore, il breakdown è un corto circuito al lato DC del convertitore; non è da considerarsi come condizione di guasto e il convertitore deve essere in grado di bloccare velocemente le sovracorrenti e riprendere con l'operazione entro 20 ms. È importante limitare il più possibile l'energia scaricata sulle griglie quando avviene questo evento per evitare che si danneggino.

Sono state considerate due soluzioni che possono essere adottate come AGPS per l'NBI di DTT. La prima è basata un sistema di alimentazione simile all'AGPS adoperato per MITICA ed ITER, ma questo sistema presenta alcuni svantaggi. L'AGPS di MITICA utilizza due stadi di conversione, il che comporta potenzialmente una minore efficienza rispetto ad un sistema a stadio singolo. A causa del limite nella frequenza di lavoro dei trasformatori di step-up, la risposta dinamica del sistema non è molto elevata, ed è necessario un filtro lato DC piuttosto significativo per limitare il ripple di tensione, il quale in caso di breakdown rilascia un'elevata energia sulle griglie acceleranti. Inoltre, in questa soluzione tutti i componenti in alta tensione sono isolati in gas SF_6, per un volume totale di gas molto rilevante. Si è quindi considerato di adottare un convertitore modulare multilivello (Modular Multilevel Converter, MMC), il quale porterebbe diversi vantaggi, tra cui un unico stadio di conversione, un controllo diretto sulla tensione lato DC e un basso ripple sulla tensione DC che permetterebbe di adottare un filtro lato DC con capacità ridotta e, di conseguenza, ridurre il contributo del filtro di energia scaricata al breakdown. Tuttavia, questo convertitore, avendo i componenti isolati in aria, occuperebbe un grande spazio, e nel caso di DTT, l'AGPS basato sulla tecnologia MMC verrebbe installato in un edificio già esistente con dimensioni definite. In questa tesi sono indagate diverse topologie di MMC in modo da minimizzarne il più possibile l'ingombro ma mantenendo i requisiti richiesti dall'iniettore di neutri.

L'MMC è composto per ogni fase da due bracci, uno superiore e uno inferiore, i quali sono formati a loro volta da una stringa di sottomoduli e un induttore. Viene analizzato il loro principio di funzionamento e

la strategia di controllo e viene approfondito il comportamento in occasione del breakdown. In risposta a questi eventi, l'MMC classico basato su sottomoduli Full-Bridge è in grado di portare a zero le correnti del lato AC e DC applicando una tensione inversa, ma in questa maniera si provocano importanti sovratensioni sulle induttanze di braccio. Le sovratensioni devono essere minimizzate con opportuni accorgimenti, in quanto influiscono sulle distanze d'isolamento delle induttanze dagli altri componenti. Vengono analizzate in dettaglio tre topologie alternative: MMC unidirezionale (uMMC), MMC ibrido simmetrico e ibrido asimmetrico. Il primo utilizza sottomoduli unidirezionali, che hanno un numero ridotto di componenti rispetto ai sottomoduli convenzionalmente usati. Non è dotato di induttanze di braccio, quindi il volume complessivo occupato da questa topologia risulterebbe molto ridotto. Tuttavia, il range d'operazione dell'uMMC risulta troppo limitato per poter essere utilizzato come AGPS per il NBI di DTT. L'MMC ibrido fa utilizzo misto di sottomoduli Half-Bridge e Full-Bridge e a seconda della loro disposizione nei bracci si può distinguere una topologia simmetrica e una asimmetrica. Si è preferito indagare ulteriormente la topologia simmetrica rispetto a quella asimmetrica poiché la prima necessita di un numero complessivo di componenti minore ed offre la possibilità di ridurre maggiormente le sovratensioni sulle induttanze di braccio al breakdown.

Viene realizzato un modello a scala ridotta dell'MMC ibrido per svolgere delle simulazioni per studiarne le performance. In particolare, viene dimostrata la possibilità di operare nell'intero range di tensione DC con un ripple inferiore al ±5% del valore di tensione determinato. Il modello soddisfa i requisiti dinamici necessari per l'AGPS. Viene simulato un breakdown per confermare le sovratensioni risultanti sulle induttanze di braccio e verificare il valore di carica che verrebbe trasferito alle griglie.

Con le simulazioni si conclude che l'MMC ibrido potrebbe essere una soluzione idonea come AGPS per l'NBI di DTT. Infine, vengono delineati quelli che saranno i prossimi compiti da svolgere, tra cui ottimizzare il sistema di controllo per migliorarne le performance, dimensionare termicamente i componenti, stimare le loro dimensioni e le distanze d'isolamento necessarie e valutare un possibile layout dell'AGPS.

Abstract

The Divertor Test Tokamak (DTT) is an magnetically confined nuclear fusion experimental device that will be realised at the ENEA Frascati Research Centre (Rome) with the aim to test alternative divertor concepts in conditions that can be reliably extrapolated to future tokamaks, such as DEMO. DTT will require additional heating system, such as radio-frequency heating and neutral beam injection (NBI) heating. The NBI that will be installed for DTT will accelerate a current of 40 A of deuterium negative ions to an energy up to 500 keV, with a resulting 10 MW of injected power to the plasma. The negative ions will be accelerated in three stages; each stage consists in an accelerating grid placed at a voltage that increases with steps of −167 kV at each stage.

The accelerating grid of the NBI will be fed by a dedicated power supply (Acceleration Grid Power Supply, AGPS), which is formed by three stages of 167 kV each, for a total voltage of 500 kV, and is rated for a nominal current of about 70 A. There are two possible solutions that have been considered as the AGPS of the NBI of DTT. The first solution is similar to the AGPS that has been used for MITICA and ITER. Such solution would have two conversion stages, which cause a reduction of efficiency with respect to a system with a single stage. Besides, the dynamic response of the system is not very fast, and it would require a large DC-filter to attenuate the voltage ripple. Such filter, in case of the frequent breakdowns on the DC side of the converter, would release an important amount of energy onto the accelerating grids. Also, in this solution all the high-voltage components are insulated in SF_6 gas: the resulting gas volume is very significant. Thus, the alternative solution would consist in a Modular Multilevel Converter (MMC), which, being composed by a single conversion stage, would have a direct control on the DC voltage. Another advantage is a lower ripple on the DC side of the converter, that would ease the requirements on the size of the DC-filter and hence the amount of energy discharged in case of breakdown. The main drawback of the MMC solution is the amount of volume that would necessitate this converter; in the case of DTT the AGPS would have to fit into the limited assigned space.

Therefore, alternative compact MMC topologies are investigated; one of the most promising ones, the hybrid MMC, makes mostly use of Half-Bridge submodules, and just a third of the total number are Full-Bridge. It is studied the behaviour of the hybrid topology in case of breakdown and are proposed some solutions to reduce the impact of the overvoltages on the arm inductors to limit the clearance required to maintain the insulation. A preliminary design of the converter is carried out, in order to determine the parameter that would allow a balanced operation at any operating point required by the AGPS. A scaled-down model of the converter is developed in order to be used in computer simulation to assess its performances and test whether they satisfy the requirements. It is concluded that the hybrid MMC could be a suitable solution as the AGPS of the NBI of DTT; further research is required to optimise its performances, conduct a thermal analysis on the components, make an estimate of their sizes and of the clearances required to maintain the insulation and outline a possible layout of the AGPS.

Contents

Chapter 1

Introduction

1.1 Introduction to thermonuclear fusion

In a future not too far ahead, the production of electric energy will be optimistically performed by renewable, carbon-free sources, mainly to put a stop to the emission of greenhouse gases and the dependence on fossil fuels, which are expected to be depleted in a limited amount of time. Unfortunately, current renewable energies sources such as solar, wind and hydroelectric power have shown limitations that prevent them from being the only participants in the coming energy mix. Hydroelectric power plants can provide a continuous large amount of power, but a further growth of the installed power is limited by the fact that most of the suitable sites have already been used. Solar and wind power have the critical problem that they are not a reliable and predictable source of energy, being strongly dependant on solar and wind intensity. Another issue is that their power intensity is low, they need vast surfaces to produce relevant amounts of power. Finally, an electrical transmission grid requires an adequate inertia, that can only be provided by large synchronous generators, used for conventional fossil fuels plants and various hydroelectric plants, but the contribution of the latter alone is not enough to ensure the stability of the grid. Renewable energies are undoubtedly necessary for the energy transition, but with the present technology is somewhat unrealistic to think that they can completely substitute fossil fuel power by themselves.

Nuclear power, based on fission, while being emission-free, is highly controversial due to safety concerns and the issue of the long-lived radioactive waste. A careful analysis shows that it considerably more desirable than is perceived from the public opinion, as nuclear energy has the potential to be one of the main practical solutions to produce carbon-free electricity in the immediate future, as the technology is already available [1].

Nuclear fusion could theoretically solve most of these issues, as it would provide a source of energy without the emission of greenhouse gases, capable of producing a large amount of power to supply the base load, which is completely reliable and contributes to the grid inertia. There is activated material involved with the operation of the plant, but its half-life is on the order of 100 years, allowing a much easier handling. These are some of the main advantages of fusion power, making it a very attractive solution with respect to fossil, nuclear and renewable sources. However, the science behind a fusion power plant is extremely complex; the possibility of producing a net power from the power balance will be investigated in ITER, which will be presented in section 1.3. Also the engineering and practical feasibility of such system is yet to be proven, the technologies that would guarantee the operation of a fusion power plant are still under research. Finally, it is important that a commercial power plant would be competitive, thus the complexity of the device must be minimised in order for the final price of energy to be comparable with other energy sources.

1.1.1 Nuclear fusion reaction

The nuclear fusion is based on the principle that when combining light elements together, some energy is released, proportional to the mass difference of the regents with the products. The main particles involved with fusion are neutrons (n), three hydrogen isotopes, hydrogen nucleus or proton (^{1}H, indicated as p), deuterium (^{2}H, indicated as D), tritium (^{3}H, indicated as T) and two helium isotopes, helium-3 (^{3}He) and helium nucleus ($^4He^{2+}$, indicated as α). There are three main reactions that are worth considering, which will be now discussed [1].

The first reaction involves two deuterium nuclei, this is the most desirable reaction as the deuterium is easily extracted from the ocean, yet it is one of the most difficult reactions to obtain. The reactions than can occur are actually two, with equal likelihood, and are the following:

$$D + D \longrightarrow {}^3He + n + 3.27\,MeV \tag{1.1a}$$

$$D + D \longrightarrow T + p + 4.03\,MeV. \tag{1.1b}$$

The two reactions produce respectively 0.82 and 1.01 MeV per nucleon. Due to the extreme conditions required to initiate this reaction, it is not currently the primary focus of current fusion research.

Another reaction involves a deuterium nucleus with a helium-3 nucleus, this reaction is hard to achieve but less than the D-D reaction, however helium-3 is a rare isotope and there are no natural supplies on earth. The reaction is:

$$D + {}^3He \longrightarrow \alpha + p + 18.3\,MeV. \tag{1.2}$$

The energy released is 3.66 MeV per nucleon, and the end products are all charged particles.

The easiest fusion reaction to initiate involves a deuterium nucleus with a tritium nucleus, for this reason the D-T reaction is the central focus of fusion research. The reaction is:

$$D + T \longrightarrow \alpha + n + 17.6\,MeV, \tag{1.3}$$

it releases 3.52 MeV per nucleon. The D-T reaction produces a high number of neutrons and it requires a supply of tritium to be capable of continuous operation. Tritium is a radioactive isotope of hydrogen with an half-life of 12.26 years, which means that there are no natural sources of tritium on hearth. The solution to produce tritium is to breed it using lithium in a blanket surrounding the region of where the D-T reactions take place; the neutrons produced by the fusion reaction have the following reactions:

$$^6Li + n \longrightarrow T + \alpha + 4.8\,MeV \tag{1.4a}$$

$$^7Li + n \longrightarrow T + \alpha + n - 2.5\,MeV, \tag{1.4b}$$

where the first reaction is exothermic, while the second consumes energy, so it is applicable only to energetic neutrons. Reaction 1.4a is much easier to initiate, but unfortunately the natural lithium present on earth is mostly ^{7}Li. In a practical reactor in order to have a steady supply of tritium is necessary to breed at least a tritium for each neutron produced, but since neutron losses are present, some sort of neutron multiplication is required to increase the breeding ratio.

The probability for a deuterium and tritium nuclei to fuse with a nuclear reaction is characterised in some quantitative form by the cross section σ. Assuming one D particle is moving towards a T particle with a velocity v, the spherically symmetric force field surrounding T projected perpendicular to the motion of D, is a circle with cross sectional area σ. If the incident particle do not pass through σ, the force is too weak and there is no collision. The experimentally measured cross section for different reactions in function of the deuterium energy are plotted in figure 1.1, as can be seen even for low energies the probability of interaction is not zero, and for very large energies the probability starts to decrease.

The end products of the fusion reaction, α particles and neutrons, contain the whole energy released by the reaction in form of kinetic energy. The kinetic energy distribution between the products is inversely proportional with respect to the mass, since the mass of α particles, m_α, is four times the mass of

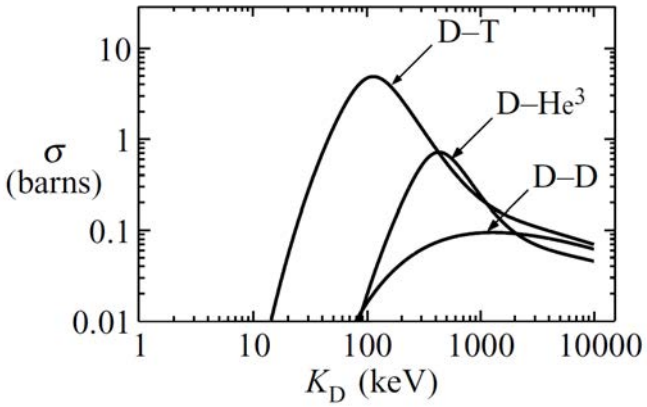

Figure 1.1: Experimentally measured cross section, measured in barns ($1\,\mathrm{b} = 10^{-28}\,\mathrm{m}^2$), for different fusion reactions as a function of the deuterium energy, K_D. Figure from [1].

neutrons, m_n, the result is:

$$\varepsilon_\alpha = \frac{1}{2} m_\alpha v_\alpha = \frac{m_n}{m_\alpha + m_n} \varepsilon = 3.5\,\mathrm{MeV} \tag{1.5a}$$

$$\varepsilon_n = \frac{1}{2} m_n v_n = \frac{m_\alpha}{m_\alpha + m_n} \varepsilon = 14.1\,\mathrm{MeV}, \tag{1.5b}$$

where ε is the energy released by a D-T reaction, 17.6 MeV, and ε_α, ε_n the kinetic energy carried by α particles and neutrons respectively.

1.1.2 0-D power balance and the Lawson criterium

In order to have a initial estimate of the powers involved in a fusion reactor, mainly the power it could produce and the power required to provide to the plasma to sustain the fusion reactions, it can be useful to make a power balance of a simplified reactor, which can be reduced to a 0-D system with power sources and sinks. Even with strong approximations, the balance will provide quantitative requirements in order for a reactor to produce a net power.

The balance of the power produced inside the plasma and externally injected with the power leaving the reactor can be expressed as:

$$P_\alpha + P_n + P_{ohm} + P_{add} = P_n + P_B + P_{syn} + P_{lin} + P_{con}, \tag{1.6}$$

where the terms on the left hand side of the equation are the power sources and on the right hand side are the power losses, more specifically:

- P_α and P_n are the power associated with the α particles and neutrons respectively produced by the fusion reactions;
- P_{ohm} is the power produced by the ohmic heating due to the current flowing into the plasma;
- P_{add} is the power injected into the plasma from additional sources, introduced in 1.2;
- P_B is the power lost due to Bremsstrahlung radiation, which is produced when energetic electrons get accelerated when colliding with ions;
- P_{syn} is the power lost due to synchrotron radiation, which is emitted from electrons that are accelerated in their cyclotron motion;
- P_{lin} is the power lost due to line radiation, the term gets relevant when impurities are present in the plasma boundary region;
- P_{con} is the power lost due to the imperfect confinement of energy over the plasma boundary through convection and induction.

P_{n} is present on both sides of the equation because the term is produced by the fusion reaction, but, as neutrons cannot be confined with electromagnetic forces, they leave the plasma with their associated power. Some terms can be grouped together as follows:

$$P_{\mathrm{ohm}} + P_{\mathrm{add}} = P_{\mathrm{ext}} \tag{1.7a}$$

$$P_{\alpha} + P_{\mathrm{n}} = P_{\mathrm{fus}}, \tag{1.7b}$$

where P_{ext} is the external power used to initiate or sustain the fusion reaction and P_{fus} the total power produced by the fusion reactions. It is possible to define a plasma energy gain factor Q as follows:

$$Q = \frac{P_{\mathrm{fus}}}{P_{\mathrm{ext}}}, \tag{1.8}$$

it indicates how much energy can be produced from the energy supplied to sustain the thermonuclear plasma. With $Q = 1$ there is breakeven, it is produced as much power as it is consumed. A more interesting situation is when $Q > 1$ and it reaches about 10, that would be a reasonable value for a reactor capable of producing electric energy connected to the electrical grid. For $Q \to \infty$ the reactor would reach ignition, there would no be need of P_{ext} as the fusion reactions will produce enough power to sustain themselves.

Most of the terms related to the power losses will now be neglected for the sake of simplicity, as P_{syn}, P_{B} and P_{lin} are generally negligible or not relevant enough to be a serious obstacle to reach the conditions for ignition in a reactor [2].

Equation 1.6 can be then simplified into the following:

$$P_{\alpha} + P_{\mathrm{ext}} = P_{\mathrm{con}}. \tag{1.9}$$

With the optimal ratio of deuterium and tritium densities, respectively n_{D} and n_{T}, (which is $n_{\mathrm{D}} = n_{\mathrm{T}} = \frac{1}{2}\, n$), the thermonuclear power density per unit volume can be expressed as:

$$p_{\mathrm{fus}} = \frac{1}{4}\, n^2 \langle \sigma\, v \rangle\, \varepsilon, \tag{1.10}$$

where $\langle \sigma\, v \rangle$ is the the velocity averaged cross section of the particles, and ε is the energy released per reaction. The fraction of power density associated with the α particles is defined as:

$$p_{\alpha} = \frac{1}{4}\, n^2 \langle \sigma\, v \rangle\, \varepsilon_{\alpha}, \tag{1.11}$$

where ε_{α} is the fraction of energy produced by a nuclear reaction that is carried by α particles. The total can then be expressed as:

$$P_{\alpha} = \int p_{\alpha}\, dV = \frac{1}{4}\, n^2 \langle \sigma\, v \rangle\, \varepsilon_{\alpha}\, V, \tag{1.12}$$

where V is the plasma volume.

The average energy of plasma particles at a temperature T is $\frac{3}{2}\, T$, and since there is an equal number of electron and ions, they have the same density $n_e = n_i = n$, so the total energy can be calculated as:

$$W = \int (n_e + n_i)\, \frac{3}{2}\, T dV = \int 3\, n\, T\, dV = 3\, n\, T\, V, \tag{1.13}$$

The rate of energy lost due to transport effects and a imperfect confinement, can be defined as follows:

$$P_{\mathrm{con}} = \frac{W}{\tau_E} = \frac{3\, n\, T\, V}{\tau_E}, \tag{1.14}$$

where τ_E is the characteristic energy confinement time.

Combining equations 1.9, 1.12 and 1.14, is it possible to obtain the following expression for P_{ext}:

$$P_{\mathrm{ext}} = \left(\frac{3\, n\, T}{\tau_E} - \frac{1}{4}\, n^2 \langle \sigma\, v \rangle\, \varepsilon_{\alpha} \right) V, \tag{1.15}$$

The condition for ignition can be derived from 1.15, being in such case $P_{\text{ext}} = 0$, it can be expressed as:

$$n\,\tau_E > \frac{12}{\langle\sigma\,v\rangle}\frac{T}{\varepsilon_\alpha}, \tag{1.16}$$

which has a minimum $n\,\tau_E > 1.5 \times 10^{20}\,\text{m}^{-3}\,\text{s}$ at $T \approx 30\,\text{keV}$, but the optimal condition is actually for lower temperatures in the range from 10 to 20 keV, and using $\varepsilon_\alpha = 3.5\,\text{MeV}$, the ignition condition becomes:

$$n\,T\,\tau_E > 3 \times 10^{21}\,\text{m}^{-3}\,\text{keV}\,\text{s}. \tag{1.17}$$

The criterion in 1.17,known as the Lawson criterion or also as the triple product, defines clearly the requirements of temperature, density and energy confinement time in order to reach the ignition condition [2]. Figure 1.2 represents the triple product in function of the temperature for different fusion experiments, as it can be noted ITER should operate operate with $Q \gg 1$, as described in section 1.3, it will demonstrate the feasibility of producing net energy from a fusion device.

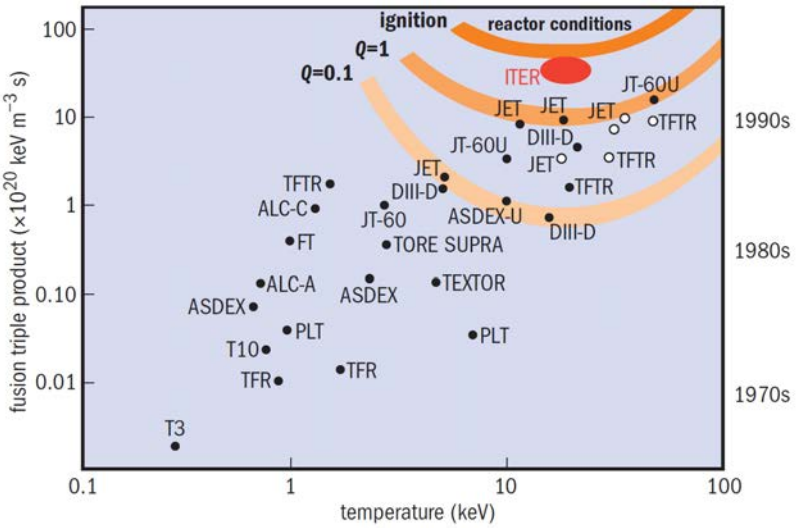

Figure 1.2: Fusion triple product in function of the temperature for different fusion experiments. Black markers indicates the machine is operating with D, instead white ones with D-T. Figure from [3].

1.1.3 Tokamak

In order to achieve the conditions imposed by the Lawson criterion, equation 1.17, a possible method is to magnetically confine the plasma in a magnetic field for a sufficient time. The main focus of the fusion research is currently on magnetic confinement in toroidal geometry, in particular on the tokamak system, which has demonstrated the best overall performances so far. A basic scheme of a tokamak is reported in figure 1.3.

A tokamak has three main sets of coils, they are also indicated in figure 1.3. The toroidal field coils produce a toroidal magnetic field that confines the particles along the toroidal direction. The inner poloidal field coils, or central solenoid, produce a change of flux through the torus that induces a toroidal electric field that drives the toroidal current, they can be seen can be as the primary of a transformer circuit, of which the plasma acts as the secondary. The outer poloidal field coils are used to confine the plasma in the torus, to control its position and shape.

The plasma current is produced by the variation of the magnetic flux over time, but it cannot grow indefinitely, meaning that inductive current drive in tokamaks will work only for a limited amount of time. The high plasma current, which is in the order of 1 to 10 MA, heats the plasma due to the Joule effect. Ohmic heating contributes to reaching high values of temperature in the plasma, but this effect alone is not enough. Plasma resistivity decreases with temperature, so reaching ingition would require a massive quantity of power. In order to drive a plasma for longer periods and heat it to high temperatures, additional heating and current drive systems are required, they will be presented in section 1.2.

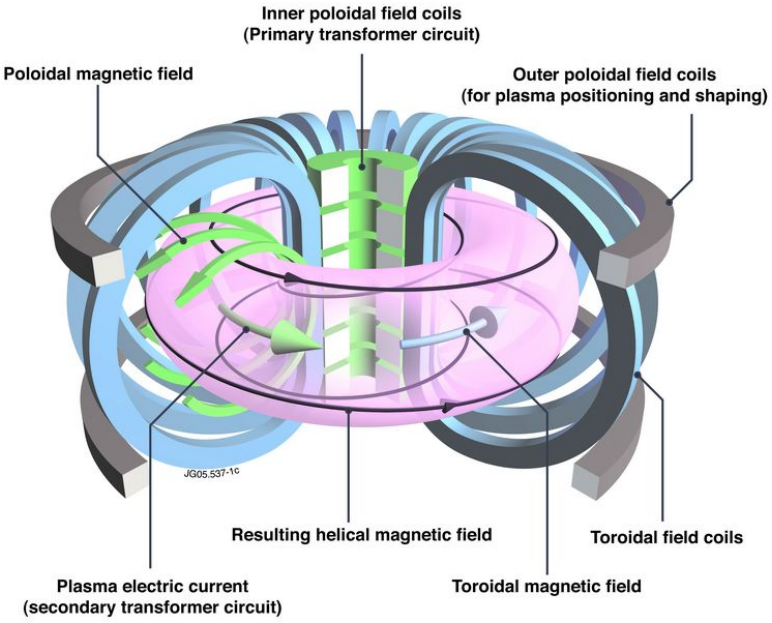

Figure 1.3: Diagram illustrating the tokamak principle. Figure from [4].

In tokamaks, the plasma is separated from the vacuum vessel, which otherwise would lead to the plasma extinction, damage to the walls and creation of impurities, by using two techniques: using a material limiter that defines the outer boundary of the plasma, or a magnetic configuration that causes to exhaust the heat on a device generally positioned at the bottom of the machine, called divertor. The divertor configuration proved to enhance the overall performances of fusion experiments, is thus adopted in most machines.

The plasma is surrounded by a blanket which has three main roles [2]. Firstly, it collects the neutron energy, which cannot be confined inside the plasma, and converts it to heat that is transferred to a coolant. The coolant, liquid or gaseous, enters an heat exchanger and produces steam, which is used in a steam turbine to generate electrical energy as would happen in a conventional power plant. Secondly, it protects the outer components and the coils, which are usually made of superconductive materials that are extremely sensible to neutron irradiation and heating. Thirdly, the blanket is composed by lithium compounds in order to breed tritium with the reactions reported in equations 1.4.

1.2 Plasma heating and current drive

In order for the reactor to reach the conditions of temperatures needed to initiate the fusion reactions, external heating is necessary. The large plasma current produces ohmic heating, but it can reach just about 3 keV, since plasma resistivity decreases with temperature, the resulting temperature scales basically linearly with plasma current [1]. At around 7 keV, α particles heating starts to become dominant to reach the final desired temperature of about 15 keV.

The main methods used in present machines are coupling of resonant radio-frequency (RF) electromagnetic waves and injection of energetic neutral particles into the plasma, Neutral Beam Injection (NBI). RF heating, which will be presented in subsection 1.2.1, consists in delivering energy to electrons or ions by making them resonate at the proper frequencies using radio frequency radiations. The NBI consists in injecting neutral particles at high speed into the plasma so that their high kinetic energy can be transferred to the plasma particles. Those methods, other than bring the 0-D power balance, can provide other benefits, as:

- drive plasma current by accelerating the proper plasma species with RF coupling or injecting neutral particles in a tangential direction;

- localised temperature and current profile shaping to improve the performances and control of the MHD instabilities;
- enhance the confinement of the plasma energy by accessing H-mode operation;
- suppression and control of the plasma instabilities;
- torque generation;
- plasma fuelling, which will be negligible for future reactors.

For fusion experiments where the ignition condition is not reached, the additional heating systems are essential in order to reach and maintain the temperature conditions of the plasma for extended periods of time, while for a fusion reactor ideally the fusion reactions will produce enough heat for maintain itself at fusion conditions, so additional heating systems are required only in the start-up phase.

1.2.1 RF heating

The RF heating make use of the cyclotron resonance phenomena to deliver power to electrons and ions inside the plasma by means of electromagnetic waves at specific frequencies. It is used for raising the plasma temperature and for producing steady state non-inductive current drive. In order to couple the waves with the plasma, is important to match the frequency with the one of the cyclotron motion induced by the magnetic field on charged particles, which is defined as:

$$\omega = \frac{q\,B}{m}, \tag{1.18}$$

being dependant on the mass, it is very different for electrons and ions, in fact for an electron it is about 140 GHz, while for hydrogen ions about 40 MHz. RF coupling is mostly effective for particles with a certain resonant frequency, which is dependant on the magnetic field, so with a defined wave frequency is possible to act on specific resonant layer, a region with the same magnetic field.

The systems used are:

- Electron Cyclotron Resonant Heating (ECRH);
- Ion Cyclotron Resonant Heating (ICRH);
- Lower Hybrid Current Drive (LHCD).

ECRH systems operate in the range of 28 to 170 GHz transferring power to the plasma electrons, which then transfer it also to ions by collisions. They can provide localised heating to the wanted resonance layers, allowing to improve the control over the plasma and improve the MHD stability [1]. Working at such high frequencies with large power is very complicated and appropriate sources have been developed, but it allows to place the source far from the plasma, simplifying the system [5]. Generally for fusion applications are used gyrotrons, which are required to ouput about 1 MW.

ICRH systems operate in the range of 15 to 100 MHz transferring power directly to the plasma ions. Their operating frequency is much lower compared to ECRH, in order to ensure good coupling with the plasma are used antennas placed very close to the plasma surface, inside the vacuum vessel, which can cause arcing and plasma breakdown [1].

LHCD systems operate at intermediate frequencies, in the range of 2.8 to 8 GHz, they are one of the most efficient methods of non-inductive current drive [1]. As ICRH, they need to have the launching structure near the plasma to achieve a good coupling.

1.2.2 NBI heating

Neutral beam injectors are used to launch neutral particles H^0 or D^0, depending on the hydrogen species used in the fusion plasma, into the plasma, where the energy is transferred by collisions. A schematic of a NBI is shown in figure 1.4, its main parts, which will be now presented, are:

- the ion source;

- the extraction and acceleration grids;
- the neutraliser;
- the Residual Ion Dump, RID.

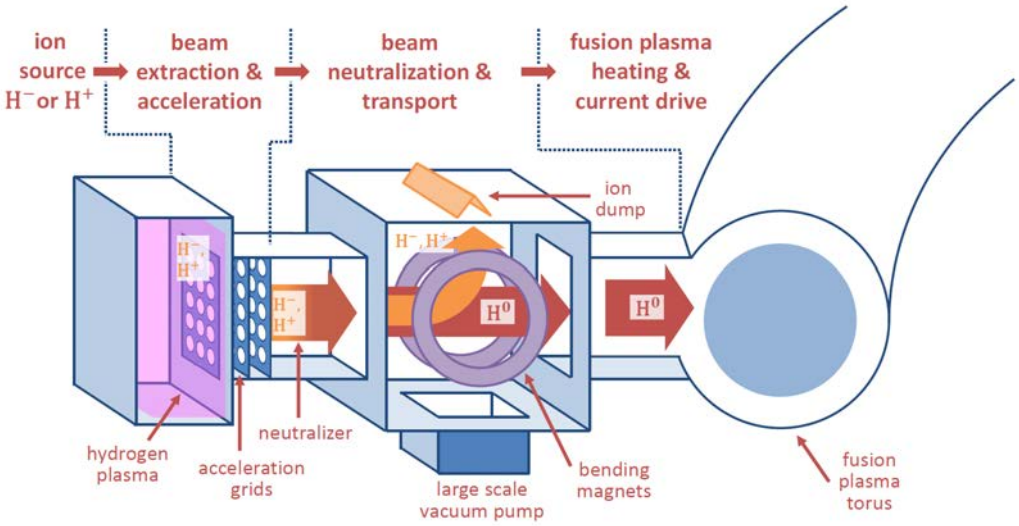

Figure 1.4: Schematic of a neutral beam injector. Figure from [6].

It is possible to realise ion sources based on both positive or negative hydrogen ions, but for the amount of energy required for ITER and other advanced thermonuclear machines, the neutralisation efficiency for positive ion beams drops to extremely low values, as can be seen in figure 1.5. Instead, for negative hydrogen ions, the neutralisation efficiency is about 60% even for very high energies, making them the only feasible choice for beam systems with energy above 100 keV, even if negative ions are more challenging to create and operate with them than positive ions.

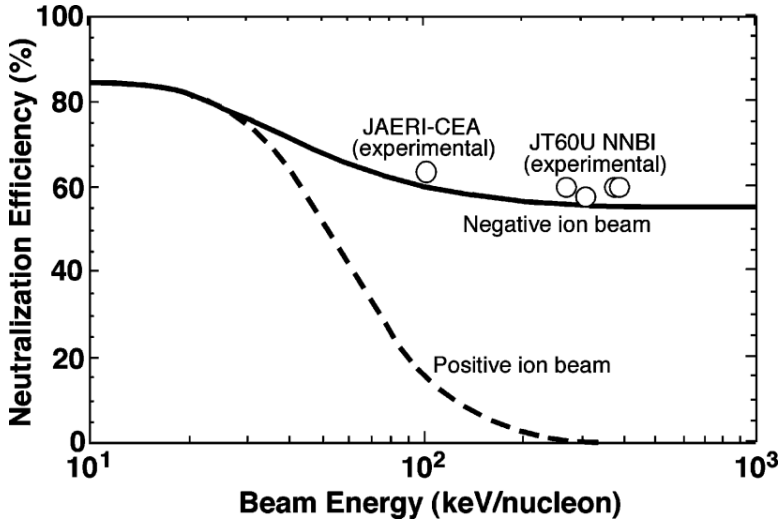

Figure 1.5: Neutralisation efficiency in dependence of the beam energy per nucleon for positive and negative ion beams. Figure from [7].

The H^- or D^- ions are extracted from a plasma that can be produced from a flow of H_2 with the two following methods [7]:

- Magnetic Bucket Ion Source: through filament-arc discharge, typically using tungsten filaments, that emit electrons and, once those electrons gain enough energy, they can ionise the H_2 and

form a plasma. This reaction is performed in a chamber with permanent magnets opportunely placed outside on its walls, with the purpose to improve the confinement of the plasma, as the multicusp field produced by the magnets reduces the particle losses at the walls. This method has the drawback that the filaments needs periodic maintenance and consequent shutdowns of the device.

- High-Frequency Driven Ion Source: after the initial ions are generated from the H_2 using ultraviolet light or a small starter filament, an external coil is excited at radio-frequency (RF) in the range of 1 MHz, driving a high-frequency current in the plasma that induces collisions capable of sustaining the plasma. Permanent magnets are installed also in RF source to minimise the losses.

To increase negative ion yield, as otherwise would be insufficient, a small quantity of Caesium vapour is seeded into the plasma, it deposits on the walls and lowers the work function on the surfaces.

Before the extraction of ions, in negative ion sources is present a magnetic filter producing a magnetic field that prevents high-energy electrons to reach the extraction region, as they would reduce the production rate of negative ions.

The extraction is performed by two grids: the plasma grid (PG) and the extraction grid (EG). The PG faces the plasma, when covered by Caesium it produces negative ions that are extracted from its multiple apertures. The second grid is at a different potential from the first, and the resulting voltage cause the ions to accelerate towards the EG. The ions extracted form a current, which intensity is defined by the following equation:

$$I_{\text{beam}} = p \cdot V^{\frac{3}{2}} \tag{1.19a}$$

$$p = \frac{k}{\sqrt{m}} \cdot \left(\frac{r}{d}\right)^2, \tag{1.19b}$$

where I_{beam} is the extracted current, V the voltage across the PG and EG, p a proportionality constant called perveance, which depends on multiple physical constants, for simplicity grouped into k, on the ion mass, m, and on the ratio of the radius of the apertures on the PG, r, over the distance between the two grids, d. In order to maximise the extracted current, d should be minimised and V maximised, meaning that the gap between the two grids will have a very high electric field. The ratio $\frac{r}{d}$ has been proven to be related to the divergence of the beam, an adequate divergence requires a small ratio. A solution to maintain a high beam current and a good divergence, is to use a high number of small apertures.

The ions are the accelerated by an electrostatic generator composed by many grids at increasing potentials. The voltage from the first to the last grid determines the resulting energy of the particles.

The ion beam gets neutralised by colliding with a background gas, H_2 or D_2, producing charge changing processes that produce mainly high-energy neutrals. It is also possible that from the collisional processes high-energy H^+ or D^+ can be produced, meaning that downstream the neutraliser the beam is composed by H^0, H^+ and H^- or D^0, D^+ and D^-, since some ions can pass through the background gas without collisional processes. The positive and negative ions are deflected by the Residual Ion Dump, RID, that could be based on transversal grids at different potentials or on a magnetic field.

The beam exiting from the RID is composed only by neutrals and can be injected into the plasma. The device is usually quite far from the vacuum vessel of the fusion machine and the surface of the port hole into which is injected is very limited; in order to maximise the energy delivered to the plasma is important that the divergence of the beam is extremely small. In the length that divides the RID from the fusion plasma additional positive ions are created by reionisations, they get deflected before entering the vacuum vessel by the strong magnetic fields present in that region, but they contribute to the overall losses.

1.3 ITER

ITER is an international experimental fusion device currently under construction in Caradache, in southern France, one of the most ambitious energy projects in the world for the time being [5]. The project is being conducted by the collaboration of 35 nations, the 27 European Union countries, Switzerland,

United Kingdom, China, India, Japan Korea, the Russian Federation and the United States. Once in operation ITER will be the largest tokamak ever built and the first fusion device to produce net energy with a gain factor of at least $Q = 10$, thus demonstrating the scientific and technical feasibility of using fusion energy as a energy source.

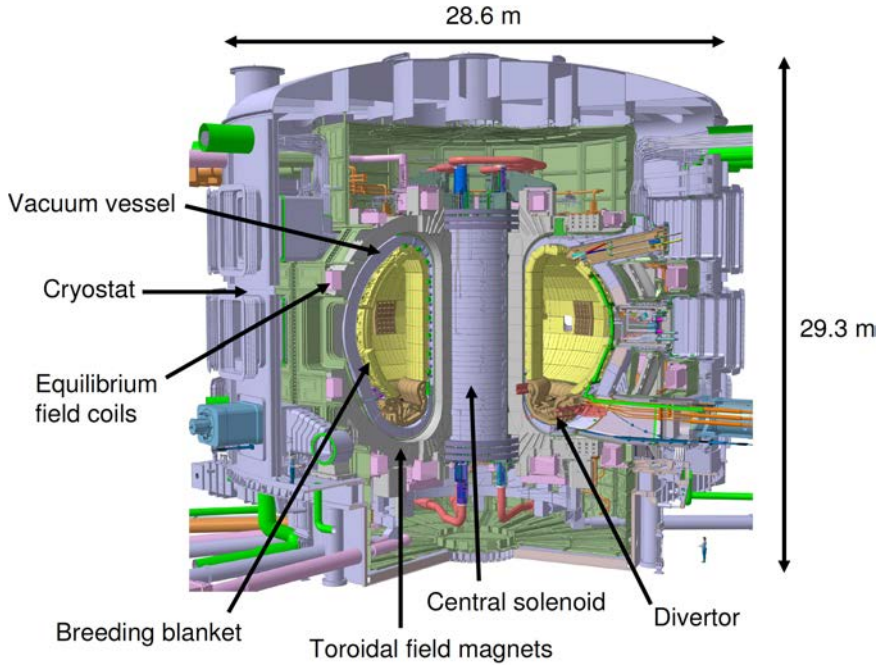

Figure 1.6: Cut-away view of ITER. Figure from [8].

The machine has bees designed in order to achieve the following goals:

- produce 500 MW of fusion power from 50 MW of input heating power for long pulses of 400 to 600 s, while this energy will not converted into electricity, the results will be extremely important for designing future machines that will be able to deliver power to the electrical grid;
- test the technologies for a fusion power plant with operating conditions closer to future fusion power plants than today's smaller-scale experimental fusion devices, such as heating, control, diagnostics, cryogenics and remote maintenance;
- achieve a deuterium-tritium plasma in which the reaction is sustained through internal heating for longer periods of time;
- prove the feasibility of producing a relevant quantity of tritium with the use of tritium breeding blankets in the vacuum vessel;
- demonstrate the safety characteristics of a fusion device and the negligible consequences to the environment.

A cut-away view of ITER is shown in figure 1.6.

The main parameters of ITER are reported in table 1.1; it will be expected to operate with three possible plasma modes, an inductive operation scenario with a burn duration of about 400 s, an hybrid scenario with a burn duration expected over 1000 s, and a steady state scenario where all the heating power is delivered from the NBI and RF-heating systems with no contribution from the central solenoid. In the last scenario the burn duration could be extended up to one hour, limit imposed by the cooling system [9]. As an experimental device, it has been designed in order to be able to operate with variants from the nominal scenarios, allowing to investigate different physical regimes and test advanced technologies, like superconducting magnets, tritium breeding modules and extreme material for the plasma facing components.

Table 1.1: ITER main parameters and operational capabilities. Table from [9]

Parameter	Attributes
Fusion power (P_{fus})	500 MW
Fusion power gain (Q)	≥ 10
Plasma major radius (R)	6.2 m
Plasma minor radius (a)	2.0 m
Plasma current (I_p)	15 MA
Toroidal field at 6.2 m radius (B)	5.3 T
Additional heating and current drive power (P_{add})	50 MW
Plasma volume	830 m^3
Plasma surface area	680 m^2
Plasma cross section area	22 m^2

The first plasma is scheduled for the end of 2025, it will initially operate with an hydrogen plasma, then it will pass to a deuterium plasma and eventually to a deuterium-tritium plasma.

The 50 MW of additional power are provided by 73 MW of installed heating and current drive power, which is the resulting combination of 33 MW of NBI, 20 MW of ECRH and 20 MW of ICRH. The NBI system in ITER will be introduced in the following subsection.

1.3.1 ITER NBI

ITER will be provided with two heating neutral beam injectors that can provide 16.5 MW of heating power each for up to 3600 s. Due to the large volume and high temperature and density of the plasma the particles have to be accelerated up to 1 MeV in order to successfully penetrate far enough into the plasma. Due to the high energy of the beam, the injectors are based on the acceleration and neutralisation of negative ions, due to the reasons presented in subsection 1.2.2. The NBIs can produce H^0 or D^0 beams, the optimal conditions are reached when the accelerator is operating with H^- for an accelerated current of 46 A at 870 kV and when with D^- for an accelerated current of 40 A at 1 MV. Both operation are expected to be essentially the same, so it will only discussed the D^- operation.

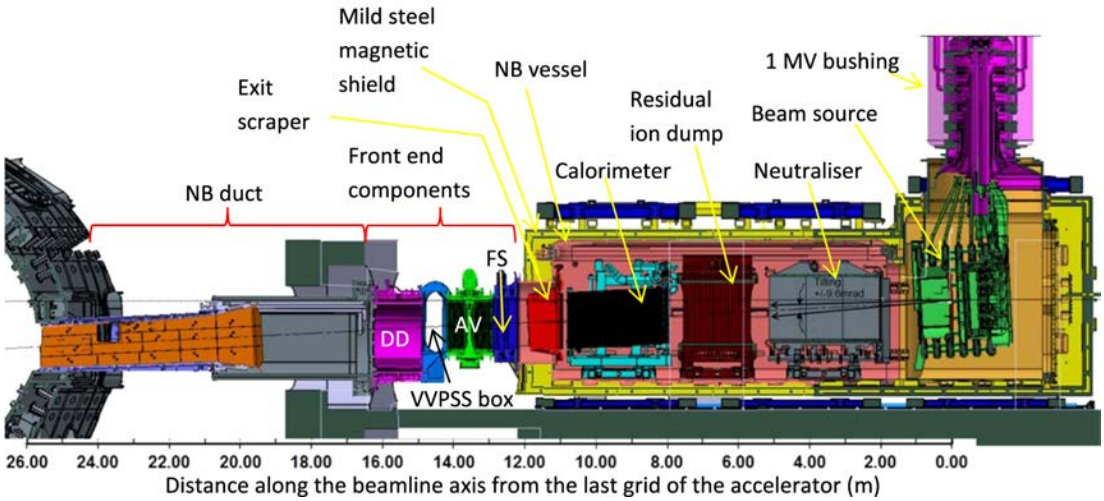

Figure 1.7: Cut-away view of an ITER NBI beam line. Figure from [10].

In figure 1.7 is shown the cut-away view of an NBI with the main components noted and a length scale as reference, the device is about 15 m long. The ion source is composed by eight RF drivers, which have been preferred to filament-based ion source due to less frequent maintenance. The accelerator grids are based on a Multi-Aperture Multi-Grid (MAMuG) configuration, which consists in five grids downstream

the extraction grid with increasing potential, from −1 MV to 0 kV with steps of 200 kV. Each grid has 1280 apertures, arranged in 16 rectangular arrays.

The device is fed by an high-voltage power supply connected through an SF_6 gas insulated transmission line. The high voltage bushing is used to separate the SF_6 of the transmission line from the high vacuum inside the beam vessel. The power supplies, which will be presented in subsection 1.3.3, provide to the NBI an input power of 55 to 59 MW, a fraction of which is dissipated on the power supply, on the transmission line and in the accelerator, leaving with an output power of the ion beam of 40 MW, which in turn is partially lost on the neutraliser and on the RID. The power losses distribution is depicted in figure 1.8.

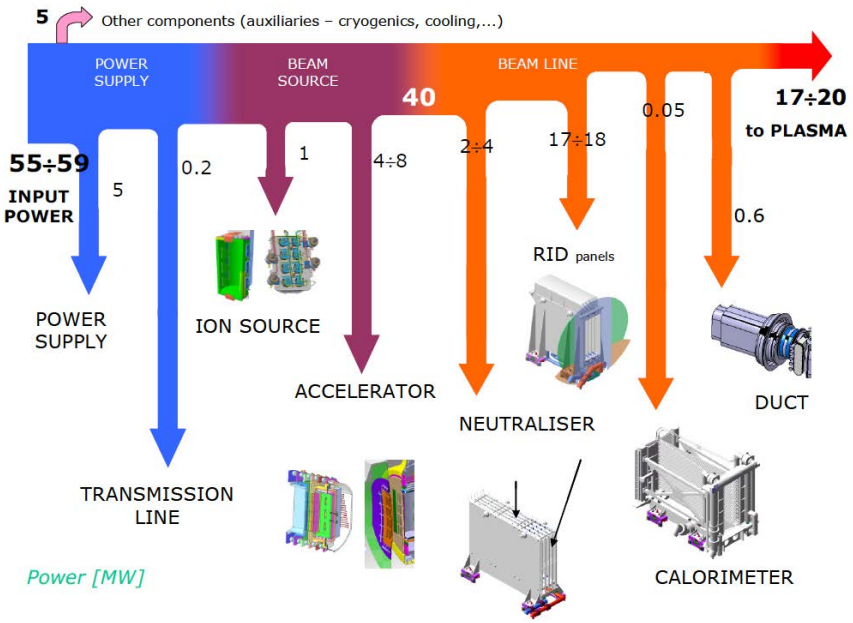

Figure 1.8: Power losses distribution for the ITER NBI. Figure from [8].

1.3.2 MITICA

Due to the ambitious performances of the neutral beams required for ITER, a dedicated test on the ion beam source and accelerator prototypes was considered necessary before the actual realisation of the NBI system. For this reason at Consorzio RFX, in Padua, Italy, has been realised a test facility, Neutral Beam Test Facility (NBTF) also known as Padova Research on ITER Megavolt Accelerator (PRIMA), with the purpose to host two experiments, prototypes of what will then used in ITER. The experiments are an ITER-scale negative ion source, Source for the Production of Ions of Deuterium Extracted from a Radio frequency plasma (SPIDER) and a full-size prototype of the 1 MV heating neutral beam injectors, Megavolt ITER Injector and Concept Advancement (MITICA) [5, 11].

The main objective of SPIDER is to finalise the development of the ion source for ITER and optimising its performances, it has been provided with a wide set of diagnostics in order to characterise the beam produced.

MITICA will serve as a testbed to analyse the design for ITER NBIs and possibly optimise it in order to achieve the full performance. The prototype will be almost identical to the NBIs that will be installed in ITER, with more diagnostics and instead of injecting power into the tokamak, it will be dissipated onto a calorimeter. Its requirements are summarised in table 1.2.

1.3.3 MITICA and ITER NBI power supply

The ITER NBI and MITICA power supplies can be divided into three main systems [8]:

Table 1.2: MITICA main requirements. Table from [11].

Parameter	H	D
Beam energy [keV]	870	1000
Acceleration current [A]	46	40
Max beam source filling pressure [Pa]	0.3	0.3
Max deviation from uniformity	±10%	±10%
Beamlet divergence [mrad]	≤ 7	≤ 7
Beam on time [s]	3600	3600
Co-extracted electron fraction (e^-/H^-) and (e^-/D^-)	<0.5	<1

- the Acceleration Grid Power Supply (AGPS) produces 1 MV in 5 stages of 200 kV to accelerate the Ion Beam, it will be discussed further in subsection 1.4;
- the Ion Source and Extraction Power Supply (ISEPS) feeds the Ion Source and the Extraction Grid, which are referred at the −1 MV potential with respect to ground;
- the Ground Related Power Supply (GRPS) feeds the devices referred to ground, in particular the Residual Ion Dump and the correction coils.

A simplified version of electrical scheme for the power supply system of ITER NBI is shown in figure 1.9; there are some minor differences with the scheme adopted for MITICA due to the different connections to the electrical grid, but they can generally be considered identical. The ISEPS is installed into a dedicated high voltage deck (HVD1) as it needs to operate at the potential of the Ions Source, which is −1 MV. The HVD1 acts as an air-insulated Faraday cage and is supplied by and insulating transformer, rated for the same insulation voltage. The output of the AGPS and of the ISEPS are connected to the Ion Source with SF_6 insulated transmission lines, the connection are made with dedicated bushings.

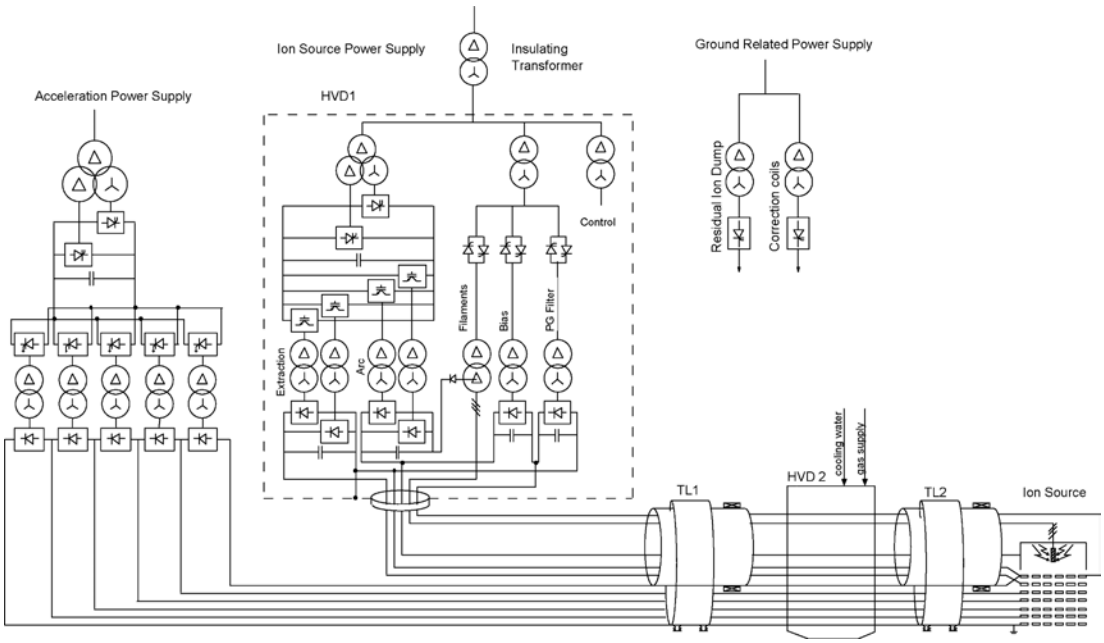

Figure 1.9: The electrical scheme for the power supply system of ITER NBI. Figure from [12].

Figure 1.10 depicts a 3-D view the MITICA system installed, as it can be noted the SF_6 transmission line is quite long, approximately 100 m.

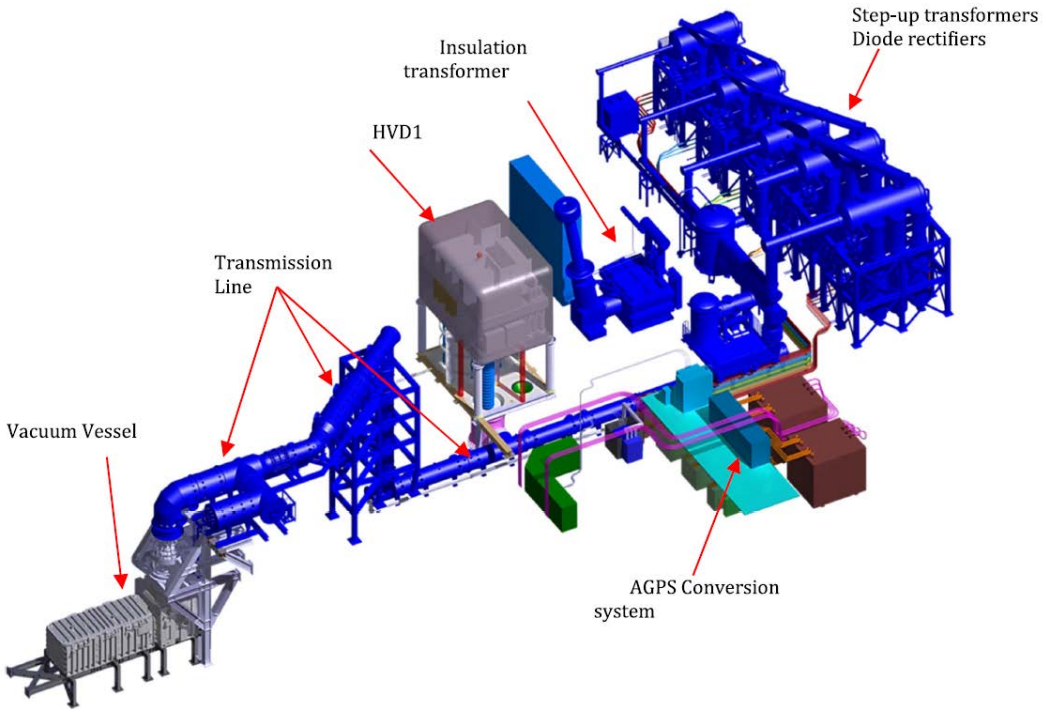

Figure 1.10: 3-D view of the MITICA power supply system. Figure from [11].

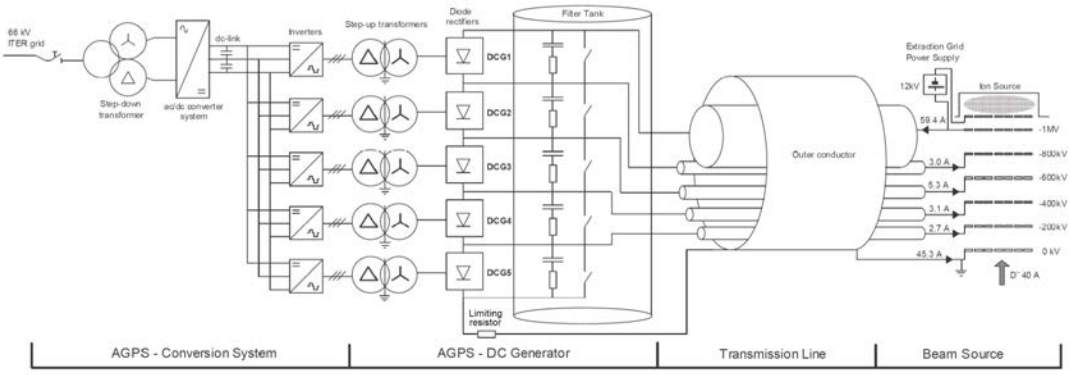

Figure 1.11: Simplified scheme of the AGPS and the connections with the beam source. Figure from [8].

1.4 AGPS of MITICA and ITER NBI

The AGPS installed for MITICA and which will be used for ITER NBI can be divided into two sections, a power conversion stage (AGPS-PC) and a DC generator system (AGPS-DCG). A simplified version of the complete scheme is reported in figure 1.11, the two sub-systems will be reviewed in the following subsections, then the operation of the AGPS during different situation will be analysed.

1.4.1 AGPS-PC

The AGPS-PC is fed by the MV grid, in ITER is connected to a 66 kV grid, then a step-down transformer system with 4 phase-shifted secondary windings reduces the voltage to feed a AC/DC conversion system. In figures 1.9 and 1.11 are presented only two secondary windings as the figures shows an old design and have not been updated yet. A dual DC voltage is produced by means of the series of two 12-pulse

Table 1.3: AGPS main output ratings. Table from [14].

Parameter	D^-, 1 MeV, 40 A		H^-, 870 keV, 46 A	
	Voltage [kV]	Current [A]	Voltage [kV]	Current [A]
DCG1	200	59.4	174	62.8
DCG2	200	56.4	174	60.4
DCG3	200	51.1	174	56.1
DCG4	200	48	174	53
DCG5	200	45.3	174	50.9

rectifiers based on thyristors. At the output of the AC/DC converter is present a DC-link capacitor bank which levels the voltage at 6500 V, 2×3250 V. The dual voltage feeds five DC/AC stages, one for each acceleration stage; each stage is composed by the parallel of two three-phase neutral point clamped (NPC) inverters, based on Integrated Gate Commutated Thyristor (IGCT) semiconductors [13]. The central point of the DC-link is accessible to be used as the neutral point for the NPC inverters. Each inverter output a square wave at a switching frequency of 150 Hz, providing a phase-to-phase voltage of 6500 V and it can switch off a current of 3 kA, a total of 6 kA per stage.

1.4.2 AGPS-DCG

The AGPS-PC is connected to the AGPS-DCG with five cables per phase per stage, for a total of 15 cables. Each stage of the AGPS-DCG is composed by a step-transformer to increase the AC voltage to one required by the accelerating grid, followed by a diode rectifier and a RC DC-filter. The step-up transformer and the diode rectifier are assembled together, as can be depicted from figure 1.10, where the windings are insulated in oil in the transformer tank and the diodes in SF_6 in a cylindrical tank placed on top of the transformer tank. The diode rectifiers provide a 6-pulse rectified DC voltage of 200 kV, their outputs are connected in series in order to reach five decreasing potentials, from -1 MV fo DCG1 to -200 kV of DCG5. The RC DC-filter is composed by five series-connected stages, placed in a single tank insulated with SF_6; the capacitance limits the output voltage ripple and the over-voltage in case of beam-off, while the resistance limits the peak current in case of the discharge of the capacitance during breakdowns.

The outputs of the high-voltage DC-filter are connected to the acceleration grids with a SF_6 transmission line, which is composed by two coaxial cylinders: the inner one is at -1 MV potential, while the outer one is at ground potential. Other tubes at the intermediate potentials are present (-200 kV, -400 kV, -600 kV ,-800 kV), the tubes and the inner cylinder are supported by insulators.

1.4.3 Normal operating sequence

The rated voltage and current outputs of the five stages of the AGPS-DCG are reported in table 1.3, for D^- and H^- operation, with a total rated power of about 52 MW. The grid currents and potentials required for deuterium operation are noted in figure 1.11. The AGPS is required to operate with adjustable voltage in the range from 20 to 100% of the nominal value and with a stable voltage during the whole operation time, which is at maximum one hour. The other requirements in term of dynamic and precision for the AGPS, also in case of a grid breakdown, are presented in table 1.4.

The operating sequence in normal conditions starts with the energisation of the DC-link with the AC/DC converter, then the DC/AC inverters are switched on and feed the respective DCG. The modulation index of inverters is controlled in feedback on the DC output voltage of the respective DCG to produce the required accelerating voltage on the grids. The start-up of the ion current in the Ion Source can be controlled following two possible scenarios [8]:

- start-up in perveance matching: the ion source drivers are controlled to generate an ion current that corresponds to the $80 - 90\%$ of the perveance value of equation 1.19a following the ramp-up of the AGPS output voltage. When the voltage reaches the set value, the current is then increased to reach the 100% of the perveance value.

Table 1.4: Dynamic and precision requirements for the AGPS. Table from [14].

Parameter	D^- or H^- operation
Voltage regulation range	20 – 100%
Voltage resolution	1 kV
Output voltage accuracy for 1 hour operation	±2%
Maximum voltage fluctuation	±2.5% at flat top
Maximum voltage ripple at steady state	±5%
Rise time of the DCG voltage	80 ms
Maximum settling time	50 ms
Maximum undershoot at beam on	15%
Maximum pulse length	3600 s
Maximum breakdown detection time	50 µs
Maximum switch-off time	100 µs
Time to be ready for restart after a grid breakdown	20 ms
Maximum number of grid breakdown	200 per pulse, 50 consecutive

- start-up at maximum voltage: the AGPS output voltage is ramped up to the set value without beam current, then the beam current is increased to the 100% of the perveance value.

At the end of the pulse the inverters are switched off and the DC-link gets de-energized. The sequence of operation of the AGPS is shown in figure 1.12 for perveance matching and maximum voltage start-up, V_{dc} indicates the voltage of the DC-link and V_{DCG} the output voltage of the AGPS-DCG.

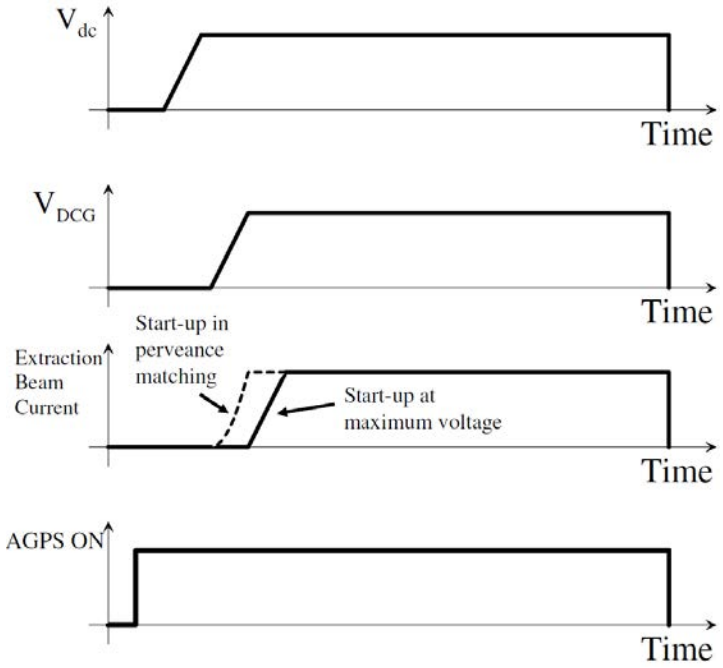

Figure 1.12: Sequence of operation and main waveforms of the AGPS. Figure from [8].

1.4.4 Operation in case of breakdown

The NBI accelerator works close to the withstand voltage capability, so breakdowns between the acceleration grids are frequent and they have to be managed by the AGPS without stopping the operation, as it is not considered a fault condition and the NBI operation has not to be stopped. From the point of view of the AGPS, the breakdowns appears as short-circuits of the load, thus, in order to avoid over-currents at the output of the inverters and large energy discharged onto the grids, the breakdown has to be detected

and the inverters switched off. The arc into the grids is then extinct, so after some ms is assumed that the inverters can safely restart their operation. In case the source of the breakdown is still present, another breakdown will immediately follow, after 50 consecutive breakdowns it will be considered as a fault and the AGPS will be stopped. The sequence of operation in case of breakdown is shown in figure 1.13, as it can be seen the AGPS-DCG and the inverters are switched off, while the AC/DC conversion system continues to operate in order to allow a faster restart. The operative requirements in case of breakdown are reported in table 1.4.

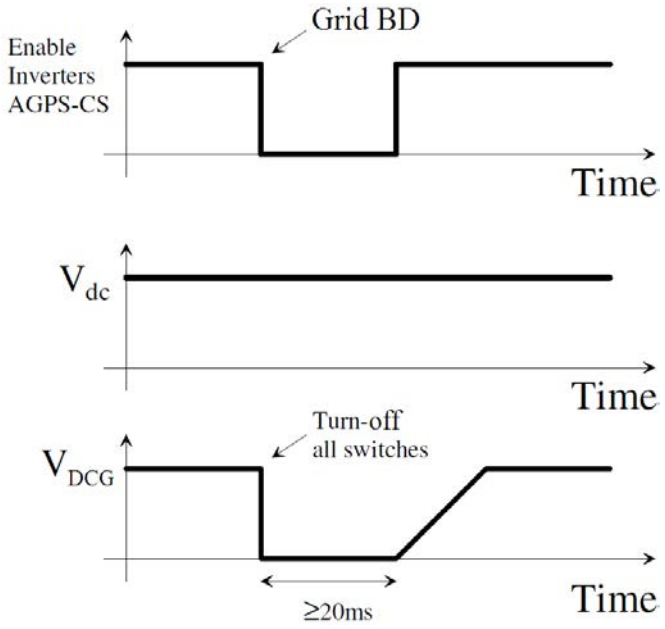

Figure 1.13: Sequence of operation of the AGPS in case of a grid breakdown. Figure from [8].

1.4.5 Operation in case of beam-off

Another possible fault condition is the beam-off, which is the sudden and unintentional loss of beam current without a contemporary and coordinated switch-off of the AGPS. From the point of view of the AGPS is equivalent to a loss of load, and it produces an over-voltage at the output of each DCG, causing electrical stresses on the NBI components. Once the beam-off is detected, the inverters have to be switched off in under 100 µs.

1.4.6 Considerations regarding the AGPS design

After a general overview of the AGPS system, is possible to individuate some critical points with the purpose to possibly find an alternative solution to mitigate them. The main disadvantages are the following [15]:

- Conversion losses potentially improvable: the AGPS firstly rectifies the AC voltage with a AC/DC conversion, then it follows a DC/AC conversion using the NPC inverters and then another AC/DC conversion with the diode 6-pulse rectifier. This double conversion stage brings higher losses in comparison with a single stage conversion.
- Reduced controllability of the DC output voltage: the DC output voltage is controlled by means of the modulation index of the NPC inverters, which due to the multiple conversion stages and components in between, cause delays in the dynamic response of the system. The voltage drops are completely compensated by using a closed-loop control over the voltage on the DC-filters, but nevertheless a direct control over the output voltage would be desirable, providing faster and more precise control.

- High energy discharged during breakdowns: in case of breakdown the current must be quickly interrupted by switching off the inverters, all the storage elements downstream discharge their energy onto the grids without an active control. The contribution to the energy discharge are the DC-filter capacitance, the overall inductance downstream the inverters and stray capacitances and inductances. The DC-filter, which is designed to reduce the voltage ripple to the determined value, cannot have its capacitance reduced by increasing the switching frequency of the inverters since this is limited by the design constraints of the step-up transformers. Thus, passive devices, such as resistors and core snubbers, are placed in the transmission line to limit the current peak and partially dissipate the energy to protect the accelerating grids from being damaged.
- High DC-link energy: the DC-link capacitance has been chosen in order to keep its voltage fluctuation at an acceptable level during load transients, especially when the load is inserted or increased. Since the thyristor rectifiers have a comparatively slow response, the total DC-link capacitance is considerable. This can become problematic in case of failure of an IGCT of the inverter, and the energy of half DC-link gets discharged into the faulty leg. In order to prevent the module explosion from the discharge, a protection based on fuses has been designed [13].
- High use of SF_6 for insulation: the high-voltage diode rectifiers and the DC-filter are place inside SF_6 insulated tanks. This gas has much higher dielectric strength than air or dry nitrogen and it is widely used for high-voltage applications, however it has an extremely high Global Warming Potential (GWP) and it complicates the management and maintenance of the plant.

In order to overcome all these issues, it has been considered to use Modular Multilevel Converters (MMC) as AGPS for future NBI, after a detailed investigation in [15] it has been proved that they can represent a promising configuration for such purposes. Using a MMC system would bring the following advantages:

- modular structure, it would simplify the design and increase the continuity of operation;
- single conversion stage, the conversion efficiency is expected be higher;
- direct control over the DC output voltage, providing a faster and more precise control dynamic response;
- the ripple is expected to be lower, thus a DC-filter could be reduced with one of the main advantages of having a reduced energy discharged into the grids in case of breakdown;
- due to the faster dynamic response, a reduced DC-link could be used with lower energy discharged in case of internal faults;
- air-insulated, it would mean a reduced use of SF_6 gas which would only be used for the transmission line.

Such type of converter presents some drawbacks, the main one is the large volume occupied: due to fact that the converter is air-insulated its components needs to have an appropriate distance between one another. Also it requires a very high number of power semiconductors. While it may initially appear to be a technology well affirmed, it certainly is for applications such as HVDC transmission systems, the application to NBI system have extremely dissimilar requirements: for instance the converter will perform only as a unidirectional rectifier, the DC voltage has to be adjustable over a wide range and the current rating are much smaller than those of HVDC systems. This means that the final solution will be different from conventional MMC systems for what concerns the topology, the control system and the components of the converter.

1.5 DTT

The Divertor Tokamak Test facility (DTT) is a future tokamak that will be realised with the aim to test alternative divertor concepts under integrated physics and technical conditions that can reliably be extrapolated to DEMO [16]. The DTT facility will be constructed at the ENEA Frascati Research Centre (Rome) during the following years. The device is depicted in figure 1.14.

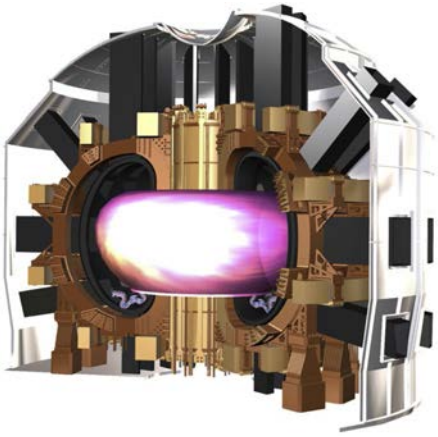

Figure 1.14: 3-D sectional view of DTT. Figure from [17].

The issue of the plasma exhaust is one of the main challenges in view of the construction of a demonstration plant, DEMO, which will be discussed in section 1.7 In a fusion device, the energy produced needs to be extracted: the energy fraction associated with neutrons is collected in the blanket, which has the purpose to convert the heat into electricity, while the one associated with charged particles that manages to escape the confined magnetic field is ultimately delivered on a narrow region, called divertor. The high power and the small surface results with extreme heat fluxes; considering the ITER conditions with $Q = 10$, a net fusion power of 500 MW, with some approximations the expected power exhausted on the divertor is about 90 MW, which would bring a heat flux in the order of 50 MW m^{-2}. At the moment the technological limit for the stationary heat flux on the divertor is about 20 MW m^{-2}, which is much lower than the expected heat fluxes in ITER. In order make such flux bearable to three strategies are foreseen:

- extend the wetted surface by the plasma on the divertor plates by changing the angle tilt of the target;
- enhance the radiation in the divertor area in order to spread the exhausted power on a larger surface;
- research new materials with improved heat resistance capability.

ITER will deal with the power exhaust with a metal divertor operating in a plasma fully detached condition, which reduces the heat and ion flux on the plasma facing components and the plasma temperature in the region near the divertor. This solution is not enough for the more severe operating conditions of DEMO and future reactors, thus different solutions need to be investigated, not just with modelling but with actual experiments on a tokamak. DTT has been proposed as a test bed for carrying out such investigations, and its main objectives can be summarised as follows:

- develop and test plasma facing components capable to withstand very large power fluxes and demonstrate that a closed loop liquid metal heat removal system could be adopted in future tokamaks;
- deepen the understanding on the physics of the exhaust process, with the final aim to further improve the divertor design by extending the wetted surface of the divertor in order to reduce the resulting power flux and by integrating liquid metals as plasma facing components;
- study plasma scenarios where plasma energy is removed by means of impurity radiation before it reaches the plasma facing components, while keeping optimised plasma core performance; this can be obtained by injecting impurities and increase the plasma density in the region nearby the plasma edge;
- improve the experimental knowledge on the heat exhaust for operating conditions that cannot be produced by present devices.

The device is characterised by a minor radius of 0.70 m, major radius of 2.19 m, maximum plasma

current of 5.5 MA, on-axis toroidal magnetic field of 6 T and an auxiliary power coupled to the plasma of 45 MW, provided by ECHR, ICRH and NBI [17]. Its pulses are planned to last 100 s.

DTT will use a significant amount of heating power, it will be installed 16 MW of ECRH at 170 GHz based on two clusters of 8 gyrotrons, 4 MW of ICRH at 60 to 90 MHz and 10 MW of NBI provided by a single tangential injector based on a negative ion source, for a total of 27.4 MW injected into the plasma. On a later stage additional heating power will be required for the full performance of DTT, and the heating mix will be composed by up to 32 MW of ECRH provided by four clusters, up to 12 MW of ICRH and 10 MW of NBI of installed power. Considering the losses, the heating systems will effectively deliver about 45 MW to the plasma. This strategy will leave enough time to verify, evaluate and modify the initial design based on considerations regarding the availability of the technical solutions and on the effective cost of each system.

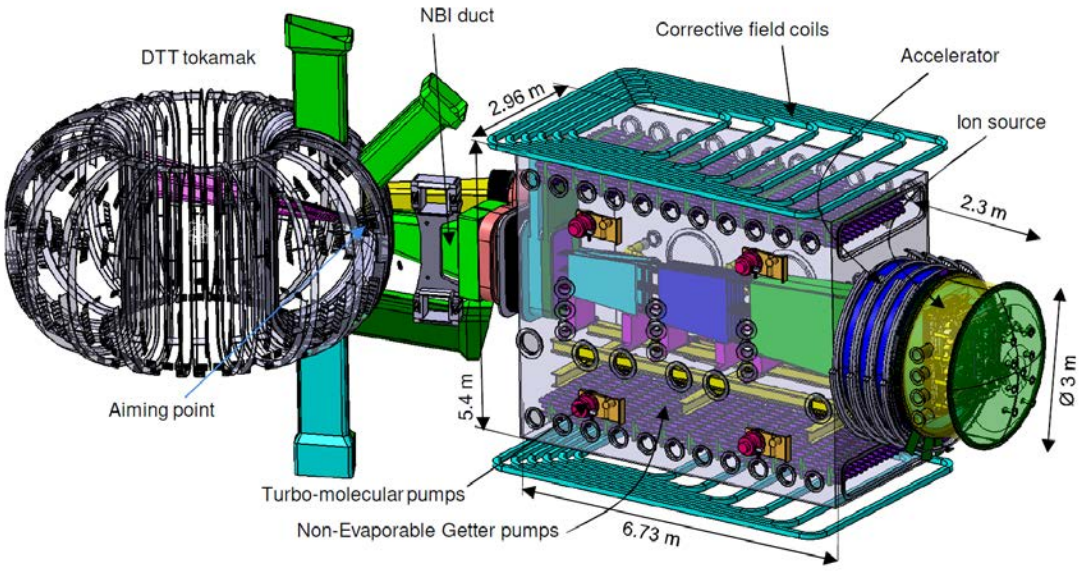

(a) Overall view of the NBI of DTT.

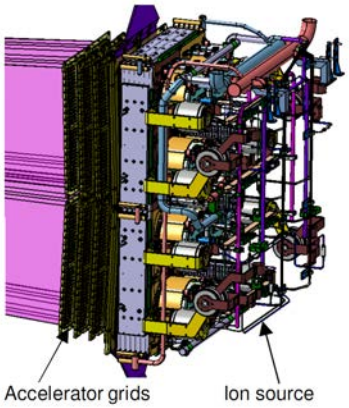

(b) View of the beam source of DTT.

Figure 1.15: 3-D view of the DTT NBI. Figures from [18].

The DTT NBI system conceptual design is rated for 10 MW of injected power, a current of 40 A of D^- with an energy of 500 keV. To reach such acceleration the particles extracted from the extraction grid will pass through grids at the decreasing potentials of −500 kV, −333 kV, −166 kV and 0 kV, respectively three accelerating grids and a grounded grid. It will be required to operate at maximum for 50 s every one hour. A 3-D view of the present design for the NBI is reported in figure 1.15.

The NBI power supplies system will be composed of the same subsystems as the one used for MITICA and ITER: AGPS, ISEPS and GPRS. The AGPS will be further discussed in the following subsection.

1.6 AGPS of DTT

The AGPS for the DTT device will provide up to 500 kV on three acceleration stages of 167 kV each, with a current of about 60 to 70 A. Its main preliminary requirements are reported in table 1.5, as it can be noted most of the dynamic and precision requirements are similar to the values set for MITICA and ITER in table 1.4, since they have been used as reference for the preliminary design.

Table 1.5: Main requirements of the AGPS of DTT. Table from [19].

Parameter	D^- operation
Rated voltage	−500 kV
Number of stages	3 (167 kV + 167 kV + 167 kV)
Voltage accuracy (referred to full voltage)	±2%
Max voltage ripple, referred to set voltage	±5%
Max rise time of the output voltage	80 ms (to reach 90% of set voltage)
Max voltage undershoot at beam on	15% (with 20 ms current ramp-up)
Voltage regulation range	20 ÷ 100% (even lower if possible)
Rated current	60 ÷ 70 A
Duty cycle	50 s every hour
Switch-off delay in case of breakdown	∼ tens of µs
Maximum charge transferred to the arc	250 mC
Maximum number of grid breakdowns in a pulse	50, also consecutive
Time to be ready for restart after a breakdown	20 ms
Input voltage	20 kV ± 10% rms phase-to-phase, 50 Hz

A similar solution to the one used for MITICA could be adopted as AGPS, opportunely adjusted for the requirements of DTT. It would only have three stages and the electrical scheme would be the one depicted in figure 1.16a, consisting in a step-down transformer, an AC/DC thyristor rectifier, a DC-link, three stages with a DC/AC NPC inverter, a step-up transformer and a AC/DC diode rectifier each, followed by the DC-filter.

After the considerations in subsection 1.4.6, the MITICA-like solution could present some issues for the DTT application which could be possibly solved by adopting an alternative solution based on a MMC scheme, of which a simplified version is reported in figure 1.16b. The alternative solution would require three step up transformers, connected to the MV grid, that would feed an AC/DC converted based on the MMC scheme each. As already mentioned, one the main disadvantages of the MMC is the large building volume and clearances to be kept from the walls required. This aspect is even more critical for the case of DTT as the building assigned for the MMC-based AGPS is already existent and the conversion system has to fit into the designated space. The topology investigated in [15] has not been designed with compactness as priority, in fact it make use of large modules and it needs large distances between the components due to the high voltage produced during a breakdown, it will be clarified after an introduction to the MMC technology in section 2.2.

The main goal of this thesis is to optimise the design of a converter based on the MMC technology that satisfies the performances required reported in table 1.5, while reducing the overall size and the clearance required. Different MMC topologies will be investigated in order to verify their compliance with the requisites.

1.7 DEMO

The knowledge and know-how gathered during the research conducted on ITER, DTT and many other experiments, will be used to develop the first next-generation fusion device, DEMO, which will explore

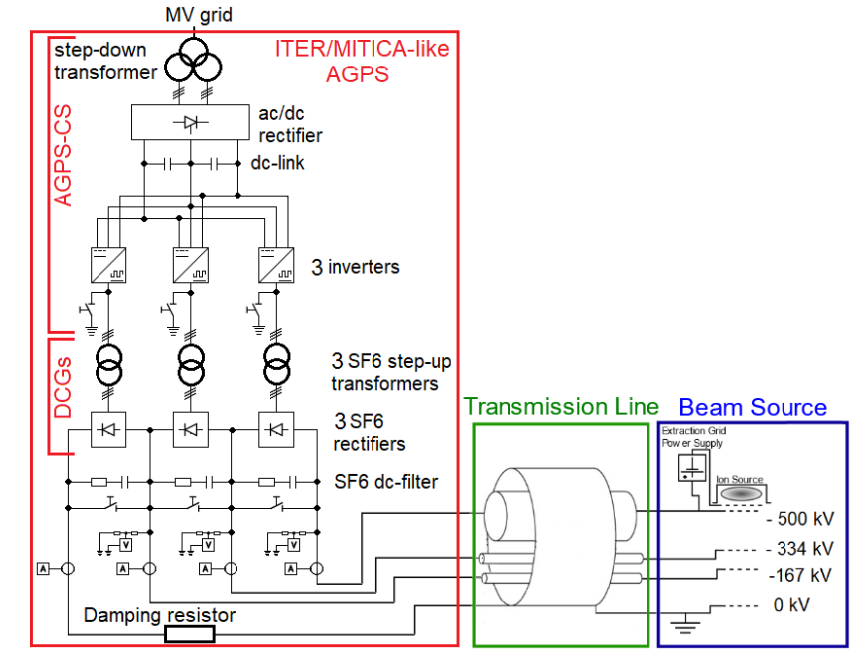

(a) MITICA-like scheme of the DTT NBI AGPS.

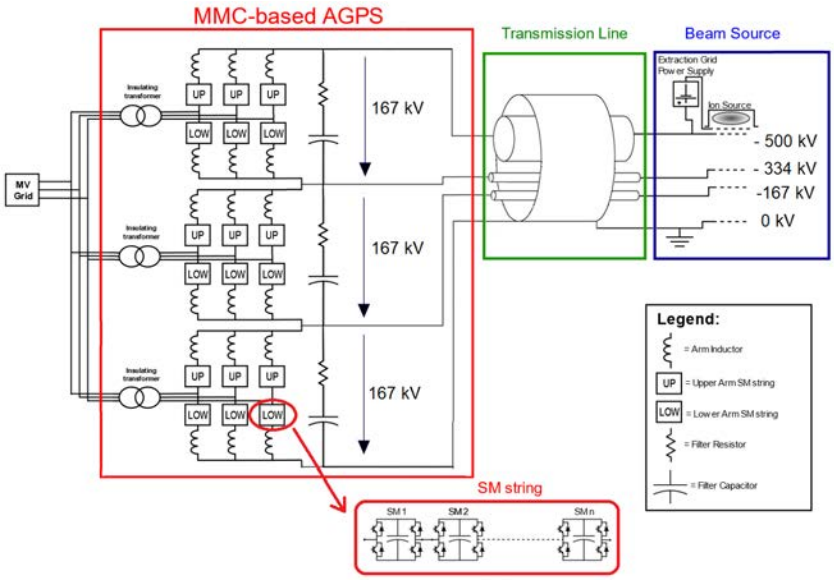

(b) MMC-based scheme of the DTT NBI AGPS.

Figure 1.16: Possible schemes of the DTT NBI AGPS. Figures from [19].

continuous or near-continuous operation, the large-scale production of electrical power and tritium fuel self-sufficiency [5]. It will be the intermediate step from experimental fusion devices to commercial fusion power plants. DEMO is still in its conceptual phase, as the construction is planned to begin in the 2040s and the start of operation in the 2050s, the main goals are [20]:

- resolve all physics and technical issues foreseen on the plant;
- demonstrate the production of 300 to 500 MW of electrical power and injection into the electrical grid;
- reach high power gain, $Q > 30$, by minimising auxiliary heating and current drive systems;
- achieve tritium breeding self-sufficiency;

Table 1.6: Comparison of the main parameters among DTT, ITER and DEMO. Table from [17].

	DTT	ITER	DEMO
Major radius, R [m]	2.19	6.2	9.1
Minor radius, a [m]	0.70	2	2.93
Aspect ratio, A	3.1	3.1	3.1
Plasma current, I_p [MA]	5.5	15	19.6
Toroidal magnetic field, B [T]	6	5.3	5.7
Heating power, P_{add} [MW]	45	50	50
P_{sep}/R [MW m^{-1}]	15	14	17
Pulse length [s]	100	400	7600

- perform long pulses, of at least 2 h;
- achieve adequate availability/reliability operation;
- minimise activation waste.

DEMO will be a simpler machine than ITER, its focus is to demonstrate the feasibility of delivering fusion energy to the electrical grid rather than explore different plasma regimes, so fewer diagnostics will be employed. The main parameters set by the current conceptual design are reported in table 1.6, where are compared with the parameters of ITER and DTT. As can be noted from the table, the ratio between P_{sep}, which is the power flowing through the last closed magnetic surface, and the major radius R for DTT is larger than for ITER, as the former will need to achieve more severe conditions in order to assess whether different divertor solutions would be suitable for DEMO [17].

Chapter 2

MMC technology

2.1 MMC scheme and basic function

The Modular Multilevel Converter (MMC) technology is based on the series of many converter elements, called submodules, which contain each a capacitor and power semiconductor components, able to produce a variable voltage based on the way the capacitor is inserted or bypassed. This class of converter has many advantages:

- it can reach any voltage level just by adding submodules thanks to its modularity and scalability;
- high efficiency on the power conversion;
- good harmonic performance resulting from the large number of voltage levels;
- it needs a small capacitance at the DC side;
- low switching losses due to a low submodule switching frequency;
- it generally has a DC fault blocking capability.

For these reasons it is a valid option for high-voltage and high-power applications, as shows their recent wide usage in the HVDC transmission.

In figure 2.1 is represented a three-phase MMC converter used as a rectifier, it can be distinguished:

- the submodules, indicated with SM, which act as variable voltage sources;
- the converter arms which are the series-connection of several submodules, there are two arms per phase, an upper and a lower one and they include an arm inductor;
- the converter legs, formed by the two arms of the same phase, there are three legs in total.

Since every submodule can output different voltage levels and the resulting arm voltages are simply the sum of its submodule voltages, the converter can produce a controllable AC and DC voltage by properly adjusting the upper and lower arm voltages. The voltage of upper and lower arms of the same phase leg are controlled in such a way that the sum of those voltages is maintained approximately equal to the desired DC-side voltage, instead their difference can be varied. Generally, since the converter produces a pure AC voltage and a pure DC voltage at its input and output terminals,the current will result alternated at the AC side and direct at the DC one, the former will split between lower and upper arms while the latter will split between phase legs.

The voltage capacitor, during normal operation, can approximately be considered constant, as it floats around its nominal value, but with a proper control system is possible to maintain the voltage close to the nominal one. In order to do so the power flow in the submodules is balanced over time, in this way also the capacitor energy will remain controlled to a stable value.

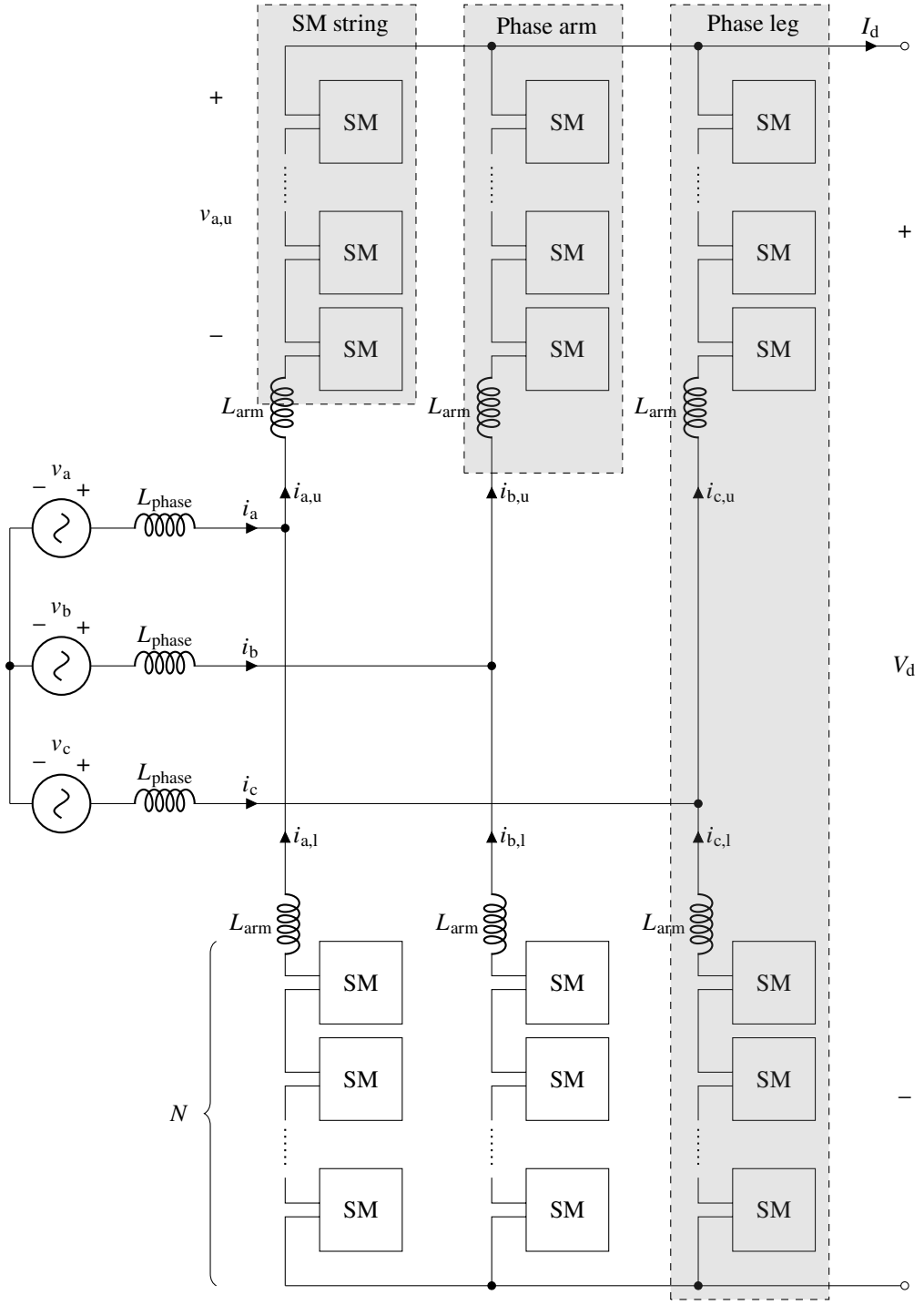

Figure 2.1: Three-phase topology of a MMC converter.

In the next section will be presented different kinds of submodules schemes and their properties that can be adopted for a MMC. In section 2.3 will be provided the main relations that can be used to analyse the operation of this converter. Section 2.4 will be a general overview of the main aspects of the control system and section 2.5 will discuss the operation of the MMC in case of a short-circuit at the DC side of the converter.

2.2 Submodules

The submodules are composed by diodes, controllable switches, generally IGBTs, and a capacitor. In addition to the two conventional topologies, the half-bridge and the full-bridge submodules, different topologies are possible with different characteristics such as configuration, number of IGBTs, number of diodes, power losses or fault-blocking capability, some of them are reviewed in [21]. In the following subsections will be presented respectively the conventional and the unidirectional submodules. Those submodules are the ones employed in the topologies that will be analysed in the following chapters.

2.2.1 Conventional submodules

The Half-Bridge (HB) and the Full-Bridge (FB) submodules, shown in figures 2.2 and2.3, will be presented. Due to their versatility, as the HB can be used for bidirectional currents and the FB for bidirectional currents and bipolar voltages, they are fitting for a large number of applications.

Half-bridge submodule

The half-bridge submodule, shown in figure 2.2, is composed by two switches with an antiparallel diode each. It can produce unipolar voltage for bidirectional currents. During normal operation it can assume two states:

- inserted, where just S_1 is switched on and at the submodule terminals is imposed the positive capacitor voltage;
- bypassed, where just S_2 is switched on and at the submodule terminals is not imposed any voltage.

In case of fault at the DC side, both switches are turned off, and based on the current direction the capacitor will be recharged or bypassed, which makes it not capable of blocking positive fault currents and more generally not able to handle short-circuits at the DC side of the converter. In order to provide the converter with fault-current blocking capability other submodules in the arms are required.

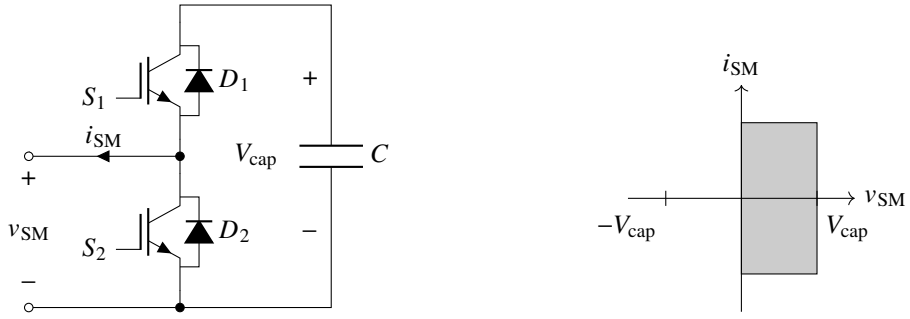

(a) Submodule scheme.

(b) Operating region.

Figure 2.2: Conventional Half-Bridge submodule.

Full-bridge submodule

The full-bridge submodule, shown in figure 2.3, is composed by four switches with an antiparallel diode each. It can produce bipolar voltage for bidirectional currents, making it one of the most flexible submodule since it can operate in the four quadrants. During normal operation it can assume three states:

- inserted, where just S_1 and S_3 are switched on and at the submodule terminals is imposed the capacitor voltage, which results positive;
- counter-inserted, where just S_2 and S_4 are switched on and at the submodule terminals is imposed the capacitor voltage, which results negative;
- bypassed, where just S_1 and S_2, or S_3 and S_4, are switched on and at the submodule terminals is not imposed any voltage.

In case of fault at the DC side, both the switches are turned off, and the capacitor will be recharged independently of the current direction, which makes it appropriate to block fault currents.

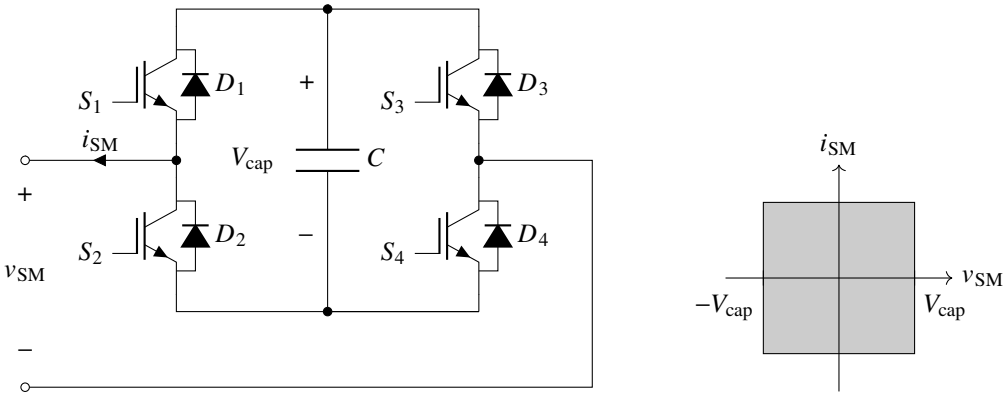

(a) Submodule scheme. (b) Operating region.

Figure 2.3: Conventional Full-Bridge submodule.

2.2.2 Unidirectional submodules

Since the power flow does no need to be reversed, but it will be always flowing from the AC source to the DC load, the converter could, in principle, use unidirectional submodules, as the ones shown in figures 2.4 and 2.5 to reduce the number of power switches. They differ from the conventional submodules in the sense that the current path is controllable just in case of positive current, in case of a negative one it can just flow through the capacitor, recharging it.

The two topologies, the unidirectional half-bridge (uHB) in figure 2.4 and the unidirectional full-bridge (uFB) in figure 2.5 are derived directly from the HB and the FB submodule respectively.

Unidirectional half-bridge submodule

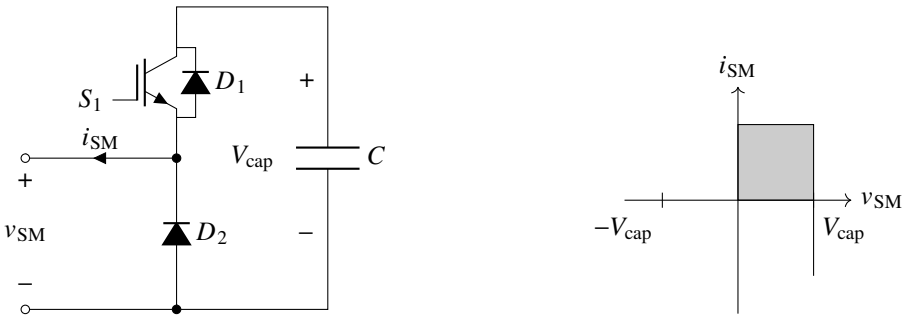

(a) Submodule scheme. (b) Operating region.

Figure 2.4: Unidirectional Half-Bridge submodule.

The uHB submodule can be obtained by removing a switch from the HB submodule, and as a result it cannot be controlled in case of negative current. It can produce unipolar voltage with positive current, in case of negative current the voltage at the submodule terminals is fixed at the capacitor voltage. During normal operation, it has two possible states:

- a positive state, where S_1 is switched on and the current is flowing through the capacitor discharging it, thus imposing a positive voltage at the submodule terminals;
- a bypassing state, where S_1 is switched off and the current is not flowing through the capacitor, thus not imposing any voltage at the submodule terminals.

The capacitor can be charged with a negative current flowing through D_1.

In case of a fault at the DC side, S_1 is turned off and the current will flow through D_2, making the submodule behave like a short-circuit. This means that a converter with just uHB submodules brings no help in case of a fault, so, like in the case of HB submodules, submodules with the capability to reverse the voltage in case of short-circuit are required to be present in the arms.

Unidirectional full-bridge submodule

The uHB submodule can be obtained by removing two switches from the FB submodule, and as a result it cannot be controlled in case of negative current. It can produce bipolar voltage with positive current, in case of negative current the voltage at the submodule terminals is fixed at the capacitor voltage. During normal operation, it has three possible states:

- a positive state, where S_1 and S_4 are switched on and the current is flowing through the capacitor discharging it, thus imposing a positive voltage at the submodule terminals;
- a negative state, where S_1 and S_4 are switched off and the current is flowing through the capacitor charging it, thus imposing a negative voltage at the submodule terminals;
- two bypassing states, where just one between S_1 and S_4 is switched on and the current is not flowing through the capacitor, thus not imposing any voltage at the submodule terminals.

Those states are depicted in figure 2.6.

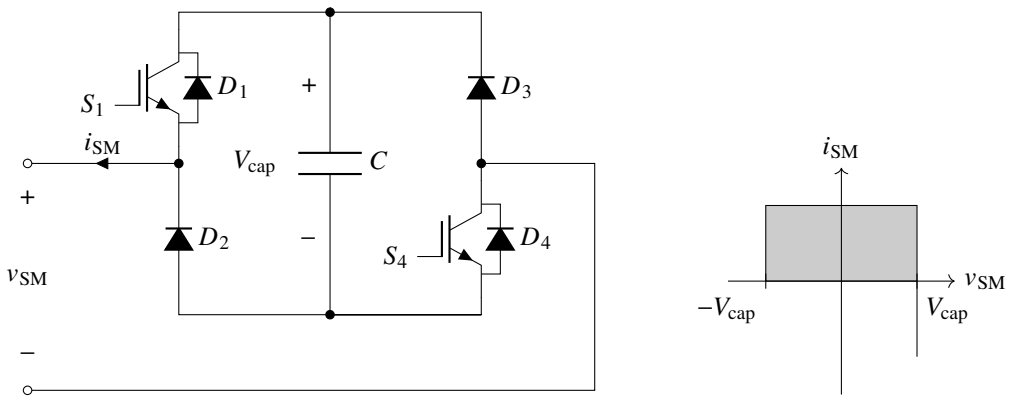

(a) Submodule scheme.

(b) Operating region.

Figure 2.5: Unidirectional Full-Bridge submodule.

The uFB submodule, in figure 2.5, still remains able to block a short circuit at the DC side of the converter, once the fault is detected the two switches are turned off and the current start flowing through D_4, the capacitor C and D_2, charging C until is current is successfully stopped. In fact, during a fault, after all the switches are turned off, all the capacitors of the same arm will result in series with opposite polarity in respect to the AC voltage source, thus blocking the fault current.

The capacitor can be charged when the submodule is in the negative state or with a negative current that has to flow through D_1 and D_3.

In [22] is discussed an identical topology but the antiparallel diodes of the IGBTs, D_1 and D_3, can be removed, thus further reducing the number of components needed. This is possible by controlling the converter in such a way that the arm currents never get negative, as they would have no possible path without the antiparallel diodes. Using this scheme would imply using only this type of submodule for the whole converter as the uHB one would require occasional negative arm currents. The use of this modified uFB would have the following issues:

- while the number of diodes used would be largely reduced, in comparison with an hybrid scheme composed by some uHB and some uFB submodules, the number of IGBTs would be increased;

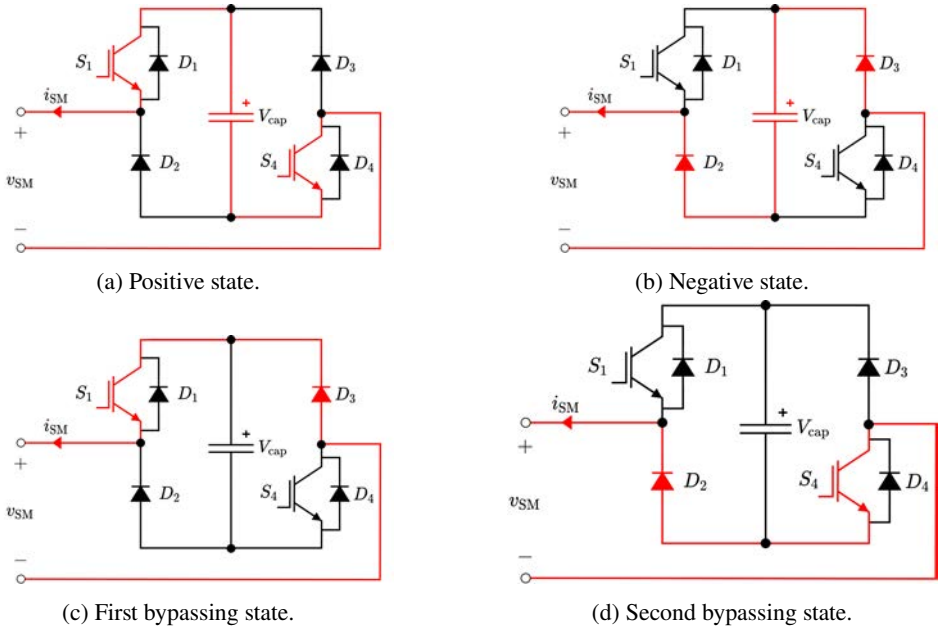

(a) Positive state.

(b) Negative state.

(c) First bypassing state.

(d) Second bypassing state.

Figure 2.6: Possible states of an unidirectional FB submodule.

- the conduction losses would be the same as using just FB submodules, while using a hybrid configuration they would be reduced.

Since there are not enough good reasons to use the uFB submodule without antiparallel diodes, the modified uFB has been disregarded.

The MMC topologies based on the combination of HB, FB, uHB and uFB submodules will be presented in the following subsection and then later investigated in the following chapters.

2.2.3 MMC topologies

Depending on the kind of submodules present in the converter is possible to identify the following MMC topologies:

- The HB-based MMC employs only HB submodules. It requires a low number of components but it is not capable of blocking DC faults. For the latter reason it cannot be employed as AGPS.

- The FB-based MMC employs only FB submodules. It is the most flexible converter in terms of operating conditions and it can block DC faults. In [15] it has been analysed its applicability as AGPS for future NBIs, but since DTT has stricter demands in terms of occupied volume, in this thesis will be investigated different topologies with the purpose to reduce the size of the AGPS.

- The hybrid MMC, it makes use of a mixed number of HB and FB submodules, so the DC-fault blocking capabilities are preserved. Depending on the disposition of the submodules in the legs, it is possible to distinguish the symmetric and asymmetric hybrid MMC, which will be analysed respectively in chapters 4 and 5.

- The unidirectional MMC (uMMC), it makes use of the unidirectional equivalent of HB and FB submodules. In literature it is generally composed by just uHB submodules, but to provide it with DC-fault blocking capabilities it is possible to replace some of the uHB with uFB submodules. It will be analysed in chapter 3.

2.3 Main circuit relations

In this section will be presented the main relations that govern an ideal MMC, useful for studying its operation and understand the control techniques. In figure 2.7 is presented the equivalent circuit of a MMC converter, where the submodules have been replaced by controllable voltage sources. In the figure are indicated the phase arms voltages and currents, where the subscript u stands for upper arm and l for lower arm. The subscript s is used for the AC-side quantities and the DC-side common mode, c for circulating currents and DC-side differential mode, which is generally not present, and d for the DC-side quantities. In the following equations the notation ϕ stands for one of the three phases, a, b or c.

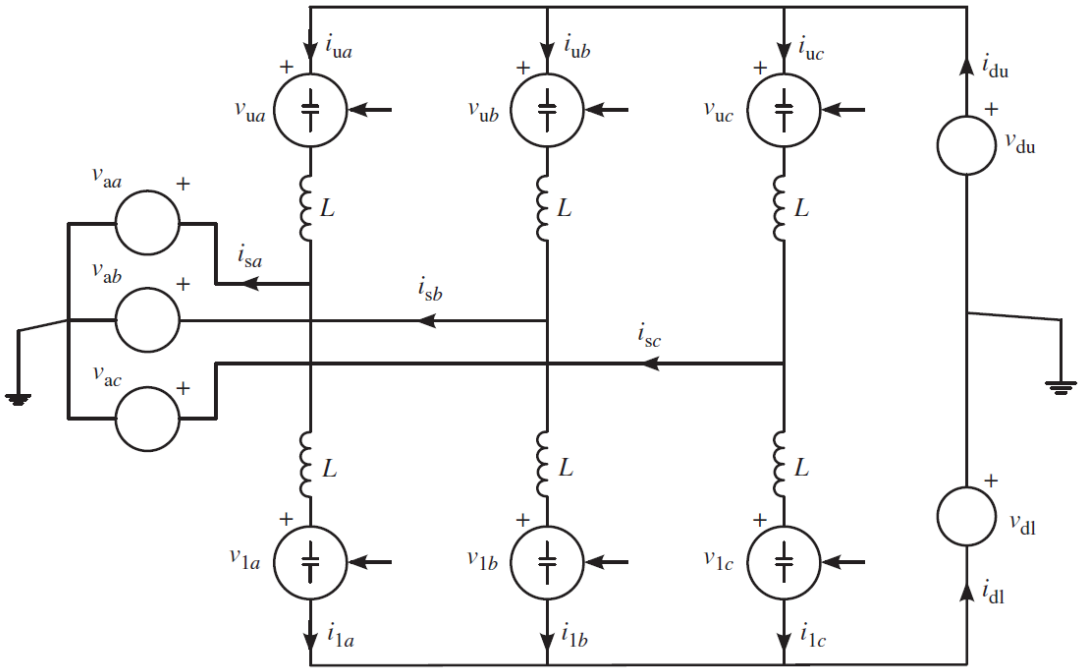

Figure 2.7: Simplified equivalent schematic of a MMC, the converter arms are represented as controllable voltage sources. Figure from [23].

It is possible to define the following quantities:

$$v_{s,\phi} = \frac{v_{l,\phi} - v_{u,\phi}}{2} \tag{2.1a}$$

$$v_{c,\phi} = \frac{v_{l,\phi} + v_{u,\phi}}{2} \tag{2.1b}$$

$$i_{s,\phi} = i_{u,\phi} - i_{l,\phi} \tag{2.1c}$$

$$i_{c,\phi} = \frac{i_{u,\phi} + i_{l,\phi}}{2}. \tag{2.1d}$$

Their physical interpretation is that $i_{s,\phi}$ are the AC-side phase currents and $i_{c,\phi}$ the average currents of each phase leg, while $v_{s,\phi}$ and $v_{c,\phi}$ the voltages that respectively drive those currents.

The voltage equation that governs the loops formed by each phase leg and the DC side is:

$$v_{u,\phi} + v_{l,\phi} + L\frac{di_{u,\phi}}{dt} + L\frac{di_{l,\phi}}{dt} - v_{d,u} - v_{d,l} = 0, \tag{2.2}$$

which can be simplified into the following equation:

$$v_{c,\phi} + L\frac{di_{c,\phi}}{dt} - v_{d,c} = 0, \tag{2.3}$$

with $v_{d,c}$ the average of the upper and lower DC-side voltages, defined as follows:

$$v_{d,c} = \frac{v_{d,l} + v_{d,u}}{2}. \tag{2.4}$$

The two voltage equations, one for the upper and one for the lower part of the converter, that govern the loops going by the midpoint of the AC side to the one of the DC side are:

$$v_{d,u} - v_{u,\phi} - L\frac{di_{u,\phi}}{dt} - v_{a,\phi} = 0 \tag{2.5a}$$

$$-v_{d,l} + v_{l,\phi} + L\frac{di_{l,\phi}}{dt} - v_{a,\phi} = 0, \tag{2.5b}$$

from which is possible to obtain the following equation:

$$v_{s,\phi} - \frac{L}{2}\frac{di_{s,\phi}}{dt} - v_{a,\phi} - v_{d,s} = 0, \tag{2.6}$$

with $v_{d,s}$ the imbalance between the upper and lower DC-side voltages, defined as follows:

$$v_{d,s} = \frac{v_{d,l} - v_{d,u}}{2}. \tag{2.7}$$

Equations 2.6 and 2.3 can be visualised as in figure 2.8, they describe the converter by using two

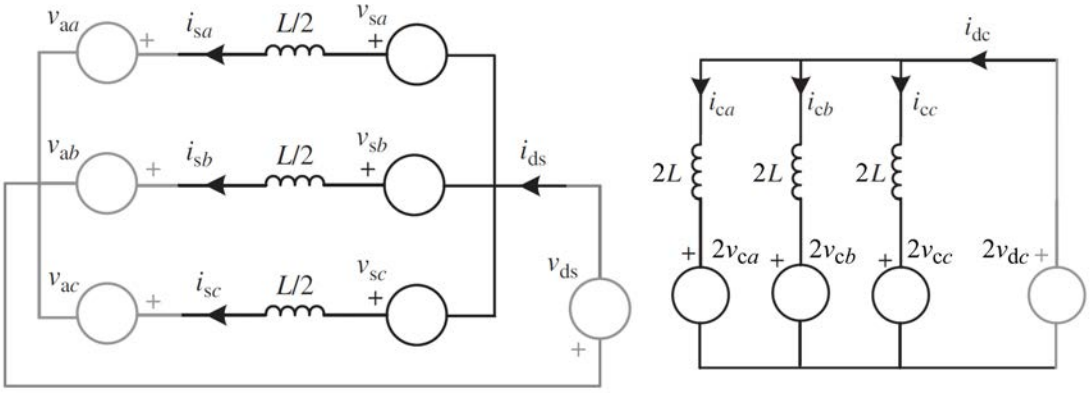

(a) AC-side circuit.

(b) DC-side circuit.

Figure 2.8: Decoupled equivalent schematics of a MMC, the parts related to the converter are drawn in black. Figures from [23].

decoupled equivalent circuits: figure 2.8a describes the AC side, with the AC-side quantities and the DC-side common mode, figure 2.8b the DC side, with the circulating currents and the DC-side differential mode. Figure 2.8a present the circuit considering the two arms per phase in parallel, hence the inductors result $\frac{L}{2}$. Instead, figure 2.8a present the circuit considering the two arms per phase in series, so the inductors and all the voltages result doubled. Generally $v_{d,s}$ and $i_{d,s}$ are zero, as they are not present during the normal operation.

During the operation in steady-state conditions the DC-side differential current and voltage are constant, thus:

$$i_{d,c} = i_{c,a} + i_{c,b} + i_{c,c} = I_d \tag{2.8a}$$

$$v_{d,c} = \frac{V_d}{2}. \tag{2.8b}$$

The AC-side quantities $v_{s,\phi}$ and $i_{s,\phi}$, can be expressed as:

$$v_{s,\phi} = \hat{v}_{s,\phi}\cos(\omega_1 t) \tag{2.9a}$$

$$i_{s,\phi} = \hat{i}_{s,\phi}\cos(\omega_1 t - \varphi). \tag{2.9b}$$

Since the converter has a limited energy storage provided by the submodule capacitors, which are not fed by external sources, the power balance between the AC and the DC side of the converter has to be preserved. The power balance can be expressed as:

$$\frac{3}{2}\,\hat{v}_{\mathrm{s},\phi}\hat{i}_{\mathrm{s},\phi}\cos(\varphi) = V_{\mathrm{d}}\,I_{\mathrm{d}}. \tag{2.10}$$

The ratio between the magnitudes of the AC-side and DC-side voltages indicates the modulation index, it can be expressed as follows:

$$m = \frac{2\,\hat{v}_{\mathrm{s},\phi}}{V_{\mathrm{d}}}. \tag{2.11}$$

Rearranging equations 2.1, is possible to obtain the following relations for the upper and lower arm voltages and currents:

$$v_{\mathrm{u},\phi} = \frac{V_{\mathrm{d}}}{2} - \hat{v}_{\mathrm{s},\phi}\cos(\omega_1\,t) \tag{2.12a}$$

$$v_{\mathrm{l},\phi} = \frac{V_{\mathrm{d}}}{2} + \hat{v}_{\mathrm{s},\phi}\cos(\omega_1\,t) \tag{2.12b}$$

$$i_{\mathrm{u},\phi} = \frac{I_{\mathrm{d}}}{3} + \frac{1}{2}\,\hat{i}_{\mathrm{s},\phi}\cos(\omega_1\,t - \varphi) \tag{2.12c}$$

$$i_{\mathrm{l},\phi} = \frac{I_{\mathrm{d}}}{3} - \frac{1}{2}\,\hat{i}_{\mathrm{s},\phi}\cos(\omega_1\,t - \varphi), \tag{2.12d}$$

it can be noted that in each phase arm are present a DC and an AC component in both currents an voltages.

The upper and lower arm voltages can be controlled by inserting and bypassing the submodule capacitors, thus they range from zero when all capacitors are bypassed, to the sum of all capacitor voltages of that arm, indicated with $v^{\Sigma}_{\mathrm{cap,u},\phi}$ or $v^{\Sigma}_{\mathrm{cap,l},\phi}$, when all capacitors are inserted. At any instant, for a HB-based MMC, the following inequalities are valid:

$$0 \le v_{\mathrm{u},\phi} \le v^{\Sigma}_{\mathrm{cap,u},\phi} \tag{2.13a}$$

$$0 \le v_{\mathrm{l},\phi} \le v^{\Sigma}_{\mathrm{cap,l},\phi}. \tag{2.13b}$$

The operational limits are extended in FB-based MMC, as the inequalities become the following:

$$-v^{\Sigma}_{\mathrm{cap,u},\phi} \le v_{\mathrm{u},\phi} \le v^{\Sigma}_{\mathrm{cap,u},\phi} \tag{2.14a}$$

$$-v^{\Sigma}_{\mathrm{cap,l},\phi} \le v_{\mathrm{l},\phi} \le v^{\Sigma}_{\mathrm{cap,l},\phi}. \tag{2.14b}$$

2.4 Operation and control

In this section will be introduced some techniques used in different stages of the control system of a MMC. For the sake of simplicity, in the following section the quantities will refer to a single phase of a HB-based MMC so some of the subscripts present in the previous section will be disregarded, but the conclusions are valid also for three-phase converters with different kinds of submodules.

Considering the loops formed by the arms, which can be obtained starting from the midpoint of the AC side to the midpoint of the DC side for just a single phase in figure 2.7, gives the following:

$$\frac{V_{\mathrm{d}}}{2} - v_{\mathrm{u}} - R\,i_{\mathrm{u}} - L\frac{\mathrm{d}i_{\mathrm{u}}}{\mathrm{d}t} = v_{\mathrm{a}} \tag{2.15a}$$

$$-\frac{V_{\mathrm{d}}}{2} + v_{\mathrm{l}} + R\,i_{\mathrm{l}} + L\frac{\mathrm{d}i_{\mathrm{l}}}{\mathrm{d}t} = v_{\mathrm{a}}, \tag{2.15b}$$

this time also the arm resistances have been considered and it has been assumed that the DC bus is balanced, thus $v_{\mathrm{d,u}} = v_{\mathrm{d,l}} = \frac{V_{\mathrm{d}}}{2}$. Combining those two equations provides the two following equations:

$$\frac{L}{2}\frac{\mathrm{d}i_{\mathrm{s}}}{\mathrm{d}t} = v_{\mathrm{s}} - v_{\mathrm{a}} - \frac{R}{2}i_{\mathrm{s}} \tag{2.16a}$$

$$L\frac{\mathrm{d}i_{\mathrm{c}}}{\mathrm{d}t} = \frac{V_{\mathrm{d}}}{2} - v_{\mathrm{c}} - R\,i_{\mathrm{c}}, \tag{2.16b}$$

where it has been used the definitions of v_s and v_c from equations 2.1, and the following expression for the upper and lower arms current:

$$i_u = \frac{i_s}{2} + i_c \tag{2.17a}$$

$$i_l = -\frac{i_s}{2} + i_c. \tag{2.17b}$$

As can be seen in 2.16a, the AC current is driven by the v_s voltage, while in 2.16b the circulating current is driven by the v_c voltage. It is desirable that the circulating current should be DC, as it would reduce the converter losses and the currents flowing in the arms. Since, for a three-phase converter, the mean values of the arm currents at steady state should fulfil the following :

$$\overline{i_u} = \overline{i_l} = \overline{i_c} = \frac{I_d}{3}, \tag{2.18}$$

the optimal value for the circulating current is $i_c = \frac{I_d}{3}$. From equation 2.16b, for i_c to be DC its time derivative has to become zero and v_c has to be controlled in order to obtain:

$$v_c = \frac{V_d}{2} - R\, i_c \approx \frac{V_d}{2}, \tag{2.19}$$

since R is generally small it is possible to neglect its term.

The maximum value of v_s that can be produced is obtained by bypassing all submodules in the upper arm and insert all submodules of the lower arm, thus resulting:

$$v_u = 0, \qquad v_l = v^{\Sigma}_{cap,l} \tag{2.20a}$$

$$v_{s,max} = \frac{v^{\Sigma}_{cap,l}}{2}. \tag{2.20b}$$

Instead the minimum value of v_s is obtained by the dual situation, all submodules in the upper arm are inserted and all submodules of the lower arm are bypassed, thus resulting:

$$v_u = v^{\Sigma}_{cap,u}, \qquad v_l = 0 \tag{2.21a}$$

$$v_{s,min} = -\frac{v^{\Sigma}_{cap,u}}{2}. \tag{2.21b}$$

To satisfy $v_{s,max} = -v_{s,min}$, is necessary that $v^{\Sigma}_{cap,u} = v^{\Sigma}_{cap,l}$, meaning that the charge between upper and lower capacitors should always be balanced. Generally $v^{\Sigma}_{cap,u}$ and $v^{\Sigma}_{cap,l}$ are chosen equal to the nominal DC voltage $V_{d,nom}$ to maximise the AC voltage, but since the AGPS will work with a fixed AC voltage, it possible to use a lower value, that will now be calculated. The maximum voltage produced by the upper arm is obtained when:

$$v_u = v^{\Sigma}_{cap,u} = \frac{V_{d,nom}}{2} + \hat{v}_s \tag{2.22a}$$

$$v_l = \frac{V_{d,nom}}{2} - \hat{v}_s \tag{2.22b}$$

$$v_s = \frac{v_l - v_u}{2} = -\hat{v}_s \tag{2.22c}$$

$$V_d = v_u + v_l = V_{d,nom}, \tag{2.22d}$$

and the maximum voltage produced by the lower arm is obtained when:

$$v_u = \frac{V_{d,nom}}{2} + \hat{v}_s \tag{2.23a}$$

$$v_l = v^{\Sigma}_{cap,l} = \frac{V_{d,nom}}{2} + \hat{v}_s \tag{2.23b}$$

$$v_s = \frac{v_l - v_u}{2} = \hat{v}_s \tag{2.23c}$$

$$V_d = v_u + v_l = V_{d,nom}. \tag{2.23d}$$

Then, the minimum voltage required by the total arm capacitors to produce the nominal DC voltage $V_{\mathrm{d,nom}}$ is the following:

$$v^{\Sigma}_{\mathrm{cap,u}} = v^{\Sigma}_{\mathrm{cap,l}} = \frac{V_{\mathrm{d,nom}}}{2} + \hat{v}_{\mathrm{s}}. \tag{2.24}$$

Clearly, the total capacitor voltage cannot remain constant throughout the operation of the converter due to the voltage ripples present, but the mean values must satisfy the equation.

In addition to the balance between upper and lower arm total capacitor voltage, is preferred for a stable operation that also all the capacitors are charged with the same average voltage, the mean voltage is:

$$\overline{v^{i}_{\mathrm{cap,u}}} = \overline{v^{i}_{\mathrm{cap,l}}} = \frac{\overline{v^{\Sigma}_{\mathrm{cap,u}}}}{N} = \frac{\overline{v^{\Sigma}_{\mathrm{cap,l}}}}{N} = \frac{V_{\mathrm{cap,tot}}}{N} \qquad \text{for } i = 1, \ldots, N, \tag{2.25}$$

where $V_{\mathrm{cap,tot}}$ stands for the total capacitor voltage in an arm, and is equal to $v^{\Sigma}_{\mathrm{cap,u}}$ and $v^{\Sigma}_{\mathrm{cap,l}}$.

It is possible to define the insertion indices as the state of insertion of a submodule, if the ith submodule of the upper arm is inserted its insertion index will be $n^{i}_{\mathrm{u}} = 1$, otherwise if it bypassed $n^{i}_{\mathrm{u}} = 0$. Using those indices it is possible to express the arm voltages as follows:

$$v_{\mathrm{u}} = \sum_{i=1}^{N} n^{i}_{\mathrm{u}}\, v^{i}_{\mathrm{cap,u}} \tag{2.26a}$$

$$v_{\mathrm{l}} = \sum_{i=1}^{N} n^{i}_{\mathrm{l}}\, v^{i}_{\mathrm{cap,l}}. \tag{2.26b}$$

Since the mean value of each capacitor, as in equation 2.25, is the same, it is possible to neglect the voltage ripples on the capacitors and consider that their mean value it is a good approximation of the capacitor voltage, thus the new expressions for arm voltages become:

$$v_{\mathrm{u}} = \sum_{i=1}^{N} n^{i}_{\mathrm{u}}\, v^{i}_{\mathrm{cap,u}} \approx \sum_{i=1}^{N} n^{i}_{\mathrm{u}}\, \frac{v^{\Sigma}_{\mathrm{cap,u}}}{N} = \frac{v^{\Sigma}_{\mathrm{cap,u}}}{N} \sum_{i=1}^{N} n^{i}_{\mathrm{u}} = \frac{V_{\mathrm{cap,tot}}}{N} \sum_{i=1}^{N} n^{i}_{\mathrm{u}} \tag{2.27a}$$

$$v_{\mathrm{l}} = \sum_{i=1}^{N} n^{i}_{\mathrm{l}}\, v^{i}_{\mathrm{cap,l}} \approx \sum_{i=1}^{N} n^{i}_{\mathrm{l}}\, \frac{v^{\Sigma}_{\mathrm{cap,l}}}{N} = \frac{v^{\Sigma}_{\mathrm{cap,l}}}{N} \sum_{i=1}^{N} n^{i}_{\mathrm{l}} = \frac{V_{\mathrm{cap,tot}}}{N} \sum_{i=1}^{N} n^{i}_{\mathrm{l}}. \tag{2.27b}$$

The definition of insertion indices can be extended to the whole arm with the following expressions:

$$n_{\mathrm{u}} = \frac{1}{N} \sum_{i=1}^{N} n^{i}_{\mathrm{u}} \tag{2.28a}$$

$$n_{\mathrm{l}} = \frac{1}{N} \sum_{i=1}^{N} n^{i}_{\mathrm{l}}. \tag{2.28b}$$

The insertion indices can assume discrete values from 0, when all the submodules of the arm are bypassed, and 1, when all submodules of the arm are inserted. Using the definition of v_{s} and v_{c}, it is possible to formulate them in terms of the insertion indices using equations 2.27, as follows:

$$v_{\mathrm{s}} = \frac{n_{\mathrm{l}}\, v^{\Sigma}_{\mathrm{cap,l}} - n_{\mathrm{u}}\, v^{\Sigma}_{\mathrm{cap,u}}}{2} \tag{2.29a}$$

$$v_{\mathrm{c}} = \frac{n_{\mathrm{l}}\, v^{\Sigma}_{\mathrm{cap,l}} + n_{\mathrm{u}}\, v^{\Sigma}_{\mathrm{cap,u}}}{2}. \tag{2.29b}$$

Combining these two equations, it is possible to obtain the following expressions for the insertion indices:

$$n_{\mathrm{u}} = \frac{v_{\mathrm{c}} - v_{\mathrm{s}}}{v^{\Sigma}_{\mathrm{cap,u}}} \tag{2.30a}$$

$$n_{\mathrm{l}} = \frac{v_{\mathrm{c}} + v_{\mathrm{s}}}{v^{\Sigma}_{\mathrm{cap,l}}}, \tag{2.30b}$$

which are the basis for selecting the proper insertion indices to produce the reference values of v_s and v_c. Equations 2.30 can be slightly modified to perform different control strategies.

A typical control system for a MMC is generally quite complex, as it composed by multiple stages, as it can be noted from figure 2.9, where is depicted a general simplified diagram of the control system, where are noted the main signals used by each block to compute its output signals. The final output will be the gate signals that command the state of each IGBTs. The quantities involved are vectors, since there is a component for each phase; they will be indicated with letters in bold. The vectorial quantities are generally transformed into their $dq0$ components. The individual blocks, which are based on the control scheme described in [23], will be briefly presented in the following subsections.

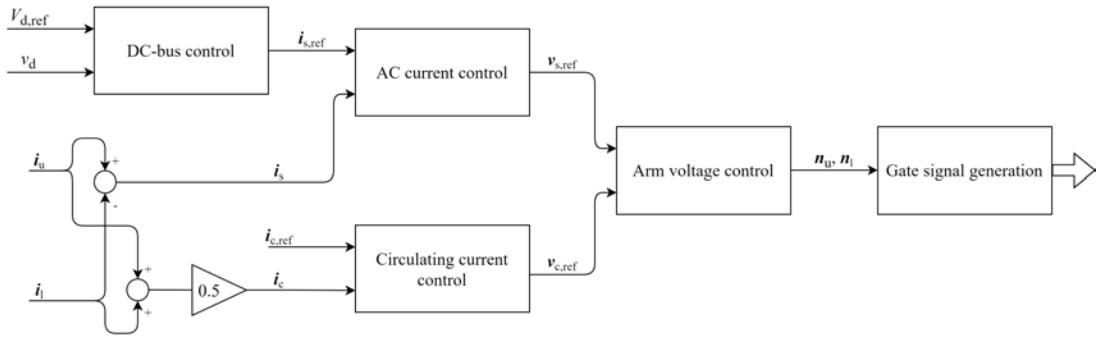

Figure 2.9: Simplified diagram of the control system for a MMC.

2.4.1 DC voltage control

The DC voltage regulation is generally performed by a Proportional Integral (PI) controller, in figure 2.9 is represented by the block "DC-bus control", which is illustrated in more detail in figure 2.10. It computes the error between the square of measured DC voltage v_d and the square of its reference value, $V_{d,ref}$. The measured DC voltage v_d is filtered to eliminate ripple and high-frequencies disturbances. The error is controlled by PI controller, whose output is limited by a saturation block. The scheme includes also an anti-windup feedback of the error before and after the saturation. The output is the reference value of the d component of the AC current, $i_{s,d,ref}$. This stage is significantly slower than the AC currents control, which is the following one.

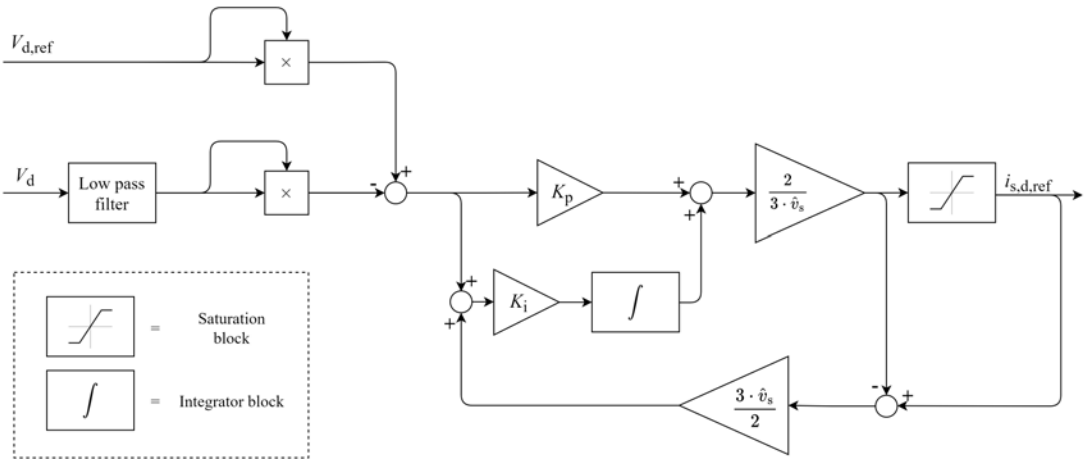

Figure 2.10: DC voltage control diagram.

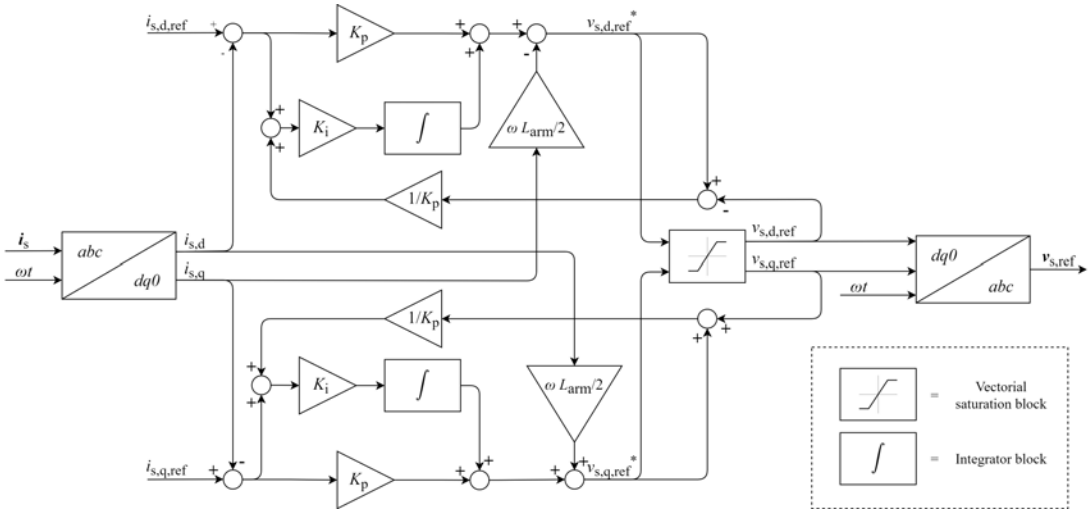

Figure 2.11: AC currents control diagram.

2.4.2 AC currents control

The AC currents control for a three-phase converter can be based on vector control rather that using a single control per phase; the former would be advantageous for the lower computational complexity, and would bring additional control also over the active and reactive powers. In figure 2.9 is represented by the block "AC current control", which is illustrated in more detail in figure 2.11. The AC currents measured, included in the vector $\boldsymbol{i}_s$, are transformed into $dq0$ components. It is also possible to work with $\alpha\beta\gamma$ components, but the former is generally preferred. The d and q components are then subtracted from their respective reference value $i_{s,d,ref}$ and $i_{s,q,ref}$. The reference values are directly related to the active and reactive power respectively. To operate with unit power factor the reference current components can be set as $i_{s,d,ref} = i_{s,ref}$ and $i_{s,q,ref} = 0$. The two errors are controlled with two PI controllers. To help improving the transient performance, at the output of each PI controllers is added a term proportional to the other $dq0$ component which decouples the controls from each other in the steady state. Then the two signals enter a vectorial saturation block to limit the values produced. The scheme includes also an anti-windup feedback of the error before and after the saturation. The signals produced, $v_{s,d,ref}$ and $v_{s,q,ref}$, are the two d and q components of the $\boldsymbol{v}_{s,ref}$, which is the vector containing the AC side voltages. These components are then transformed back into abc components.

2.4.3 Circulating currents control

The circulating current control controls the $\boldsymbol{v}_{c,ref}$ voltage in order to drive the circulating currents $\boldsymbol{i}_{c,ref}$ to their reference value, which is $\frac{I_d}{3}$. In figure 2.9 is represented by the block "Circulating current control", which is illustrated in more detail in figure 2.12. This scheme has to be applied individually to each phase. It make use a Proportional Resonant (PR) controller to control the error of the reference values $\boldsymbol{i}_{c,ref}$ with the circulating currents resulting from the one measured $\boldsymbol{i}_c$. The reference value of the circulating currents $i_{c,ref}$ is computed as one third of the DC current i_d, as proposed in section 2.4, after being filtered to cancel the ripple components.

2.4.4 Arm voltages control

This control is devoted to the selection of the insertion indices in order to make the total capacitor voltages of each arm converge to V_d, as stated in equation 2.25; in figure 2.9 is represented by the block "Arm voltage control". The insertion indices are computed with equations similar to the ones in 2.30. There are four main schemes that can be employed, and will now be presented.

Direct voltage control substitutes the terms $v_{cap,u}^{\Sigma}$ and $v_{cap,l}^{\Sigma}$ from equations 2.30 with their common mean

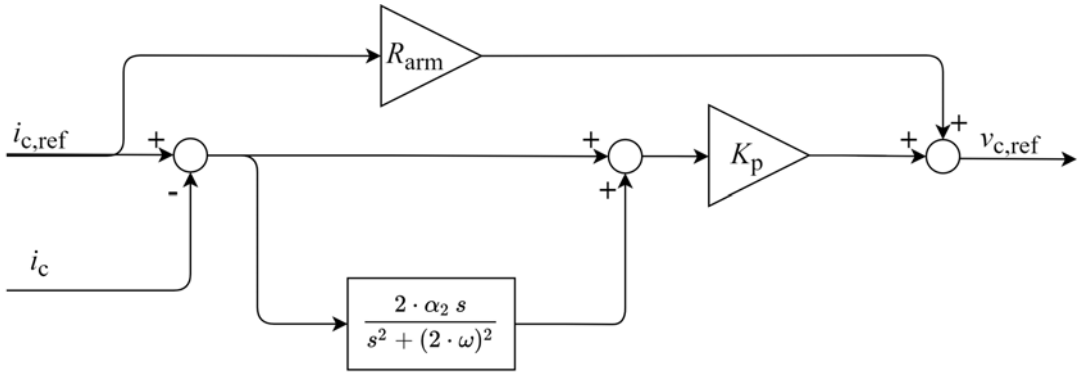

Figure 2.12: Circulating current control diagram.

values $V_{cap,tot}$, as follows:

$$n_u = \frac{v_{c,ref} - v_{s,ref}}{V_{cap,tot}} \tag{2.31a}$$

$$n_l = \frac{v_{c,ref} + v_{s,ref}}{V_{cap,tot}}. \tag{2.31b}$$

The system becomes asymptotically stable and has a low computational complexity, but creates parasitic components on the produced voltages which can be easily suppressed by the upstream controllers.

Closed-loop voltage control uses directly the relations from equations 2.30, as follows:

$$n_u = \frac{v_{c,ref} - v_{s,ref}}{v^{\Sigma}_{cap,u}} \tag{2.32a}$$

$$n_l = \frac{v_{c,ref} + v_{s,ref}}{v^{\Sigma}_{cap,l}}. \tag{2.32b}$$

Parasitic components are no longer produced, but an additional controller is required to regulate the energy of each arm to the reference value.

Open-loop voltage control substitutes the terms $v^{\Sigma}_{cap,u}$ and $v^{\Sigma}_{cap,l}$ from equations 2.30 with their reference values $v^{\Sigma}_{cap,u,ref}$ and $v^{\Sigma}_{cap,l,ref}$, as follows:

$$n_u = \frac{v_{c,ref} - v_{s,ref}}{v^{\Sigma}_{cap,u,ref}} \tag{2.33a}$$

$$n_l = \frac{v_{c,ref} + v_{s,ref}}{v^{\Sigma}_{cap,l,ref}}. \tag{2.33b}$$

The reference values are computed using estimates of the ripple on the total capacitor voltages of each arm. The system becomes asymptotically stable and none, or negligible, parasitic components are produced.

Hybrid voltage control uses at the denominator of equations 2.30 the sum of the mean values $V_{cap,tot}$ with the terms $v^{\Sigma}_{cap,u}$ and $v^{\Sigma}_{cap,l}$ passed through a band-pass filter that removes their mean value but leaves the ripple. The resulting relations are:

$$n_u = \frac{v_{c,ref} - v_{s,ref}}{V_{cap,tot} + \mathrm{BPF}\left\{v^{\Sigma}_{cap,u}\right\}} \tag{2.34a}$$

$$n_l = \frac{v_{c,ref} + v_{s,ref}}{V_{cap,tot} + \mathrm{BPF}\left\{v^{\Sigma}_{cap,l}\right\}}, \tag{2.34b}$$

The system becomes inherently asymptotically stable.

2.4.5 Modulation and submodule balancing

Once that the arms voltages have been computed as described in the previous subsection, the single submodules power switches have to be controlled in order to produce such voltages. This stage has two main roles, to choose how many capacitors insert to produce the required voltage and to balance the capacitor energies of the single submodules by properly selecting which ones to insert or to bypass. In figure 2.9 these actions are performed by the block "Gate signal generation", which directly outputs the signals that command the IGBTs.

For this purpose is usually adopted the Pulse Width Modulation (PWM) technique. It can be adapted for MMC by using multiple carriers and one single voltage reference. Basically it consists in comparing a reference signal with a triangular signal with fixed frequency, the carrier. When the former is over the latter, is produced a 1 as output, otherwise a 0. There are different methods employed, which depend on how the reference and the carriers are arranged, the main ones will now be presented.

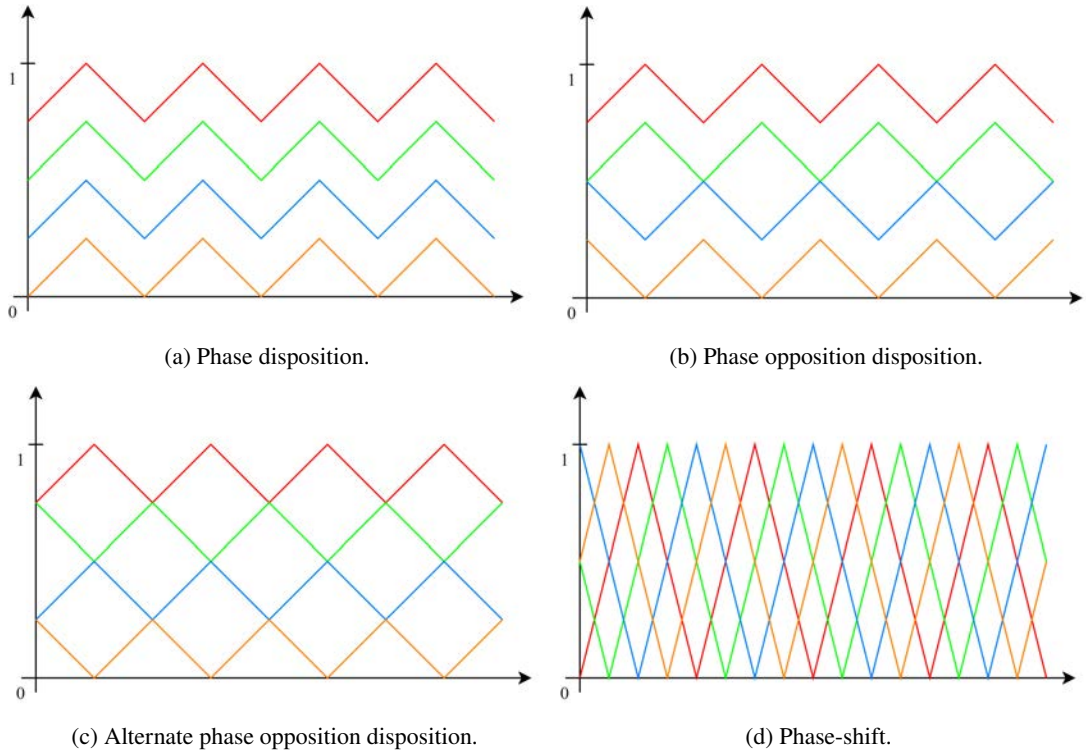

(a) Phase disposition.

(b) Phase opposition disposition.

(c) Alternate phase opposition disposition.

(d) Phase-shift.

Figure 2.13: Schemes of different multilevel carriers techniques.

Level-shifted carrier modulation

Level-shifted carrier modulation make use of carriers that are placed with different levels of offset one another, in order to split the voltage range into a number of sub-ranges, one for each submodule. Depending on how the carriers are disposed between each other, it is possible to identify the following possible schemes:

- Phase Disposition (PD), where all carriers have the same phase angle but are placed at different levels of offset;
- Phase Opposition Disposition (POD), where the upper half of the carriers are in anti-phase with respect to the lower half;
- Alternative Phase Opposition Disposition (APOD), where the carriers have alternating phase angles of zero and π, adjacent carriers will result in anti-phase.

The carriers dispositions of such schemes are illustrated in figures 2.13a, 2.13b and 2.13c. Even if the

numbers of levels corresponds to the number of submodules, in practice each level cannot be assigned to a submodule, as the switching distribution and loading would result extremely uneven between the submodules, in addition there would be no balancing of the capacitors. So with level-shifted schemes is mandatory an algorithm for selecting the submodule insertions.

Phase-shifted carrier modulation

Phase-Shifted (PS) carrier modulation make use of $2\,N$ carriers, one for every submodule, which are symmetrically phase shifted one another, as indicated in the following:

$$\varphi^i = \frac{2\,\pi}{N}\,(i-1) \qquad \text{for } i = 1, \ldots, N. \tag{2.35}$$

It is possible to use a displacement angle between the upper and lower arm carriers in order to reduce the harmonics. Depending on the angle chosen the harmonic content will be alternatively reduced in the AC voltage v_s or in the circulating voltage v_c. The disposition of the carriers are illustrated in figure 2.13d. PS modulation can be directly assigned to submodules, with no need of additional submodule selection algorithm, and the energy balancing of the capacitors will be maintained. There is a requirement regarding the ratio of the carrier frequency with the reference frequency: it has to be non-integer to guarantee the energy balancing. The average switching frequency of the submodules will result similar to level-shifted schemes, since for the latter the carrier frequency is N times higher but is split among N submodules.

Nearest-level control

Nearest-level control (NLC) is an alternative method to carrier-based PWM, it consists in sampling the reference signal at an high frequency and approximating it with the nearest level that can be produced by the submodules. Since the approximation can only assume discrete values, the reference waveform becomes a staircase. As for the level-shifted carrier modulation, NLC requires a sorting algorithm. The resulting spectrum contains more or less all harmonic orders, and the amplitude of the harmonic content can be reduced only by increasing the number of submodules, given a sufficiently high sampling frequency. It has the advantage to be simple to implement.

2.5 DC-side short circuit

In case of a short-circuit on the DC side of the converters, MMCs have generally two ways of dealing with it. MMC topologies with enough FB or uFB submodules are inherently able to block the AC currents, while MMCs based on HB or equivalent submodules will have to open the circuit breakers on the AC side. Such breakers are inadequate for dealing with frequent breakdowns since they intervene with a delay in the order of 10 ms. During such time a lot of energy could be discharged onto the accelerating grids of the NBI, causing important damages. Also, their number of switching operations is limited and they would be required to close the circuit to resume the operation of the NBI in a interval of time too short.

Therefore, for the AGPS application it is mandatory to use MMCs with enough FB or uFB submodules, to nullify the short-circuit current in short time, repetitively. This ability in literature is often referred as fault-blocking capability. Even if for the AGPS a DC-side short-circuit is not generally considered a fault condition, as discussed in 1.4.4, this designation will still be used for coherence with the common MMC terminology. Once the breakdown is detected, all the IGBTs are commanded to turn off and the capacitors of the submodules with fault-blocking capabilities are then inversely inserted so that the opposing voltage can drive the currents to zero. The arm inductors helps in limiting the rate of increase of the current, and the time required to block the AC currents is related to the number of components with fault-handling capability in series. A higher number of submodules produces an higher opposing voltage, thus faster current-blocking time. All the arm currents have to be blocked.

To analyse the breakdown event from the point of view of the converter, it can be useful to divide it in two subsequent phases: the former lasts from the instant of the breakdown to the moment in which the IGBTs are turned off, the latter lasts until all arm currents are nullified. The two phases are depicted in

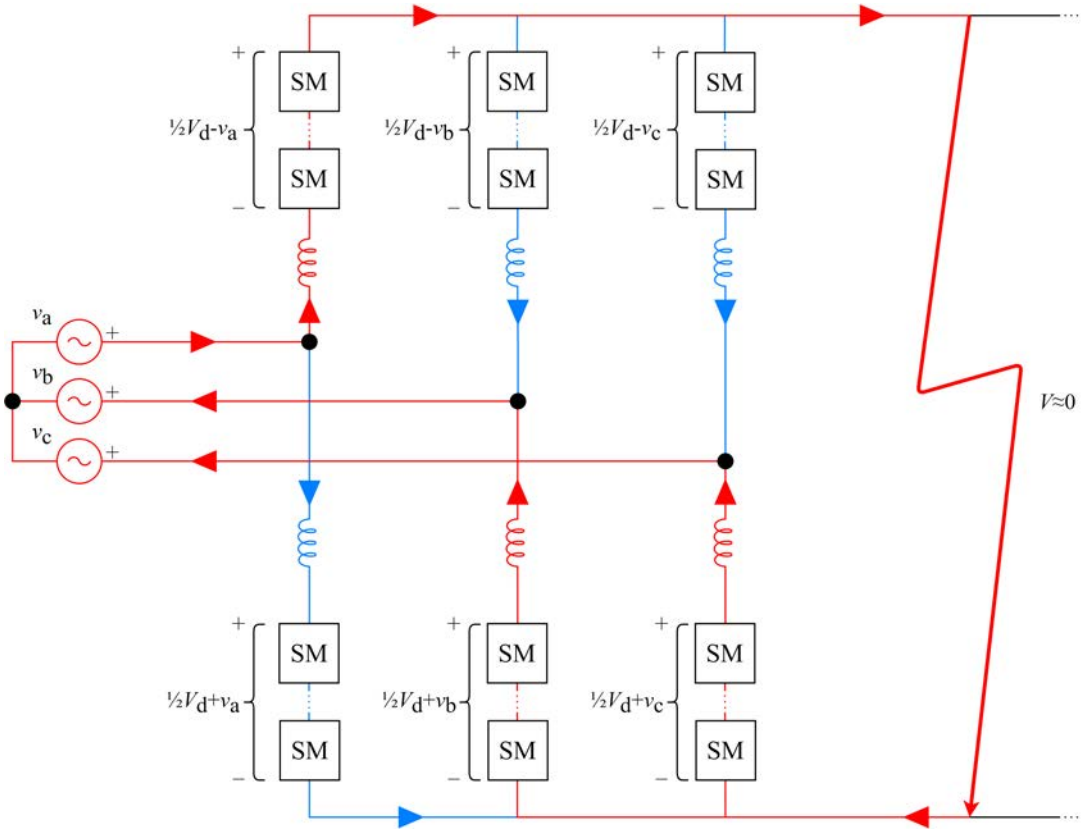

Figure 2.14: Possible schematic of a MMC in case of a short-circuit at the DC side before the IGBTs have been turned off. The current paths are drawn in red and blue.

figures 2.14 and 2.15. The red paths represent the current loops that link the AC side of the converter to the DC side, while the blue paths represent the current loops of the others arms. It is also noted the arm voltage of each arm, where $V_{\text{cap,tot}}$ is the total capacitor voltage in a arm. The direction of the current in each arm is determined by their direction in the moment that the short-circuit takes place.

The first phase is much shorter than the second one: after the time required to detect the breakdown, which is about 5 µs, the IGBTs takes some µs to turn off, depending on their characteristics. The total time results generally less than 10 µs. The circuit during this period appears similar or equal to the one illustrated in figure 2.14, as the direction of the currents may differ. The arms are still producing the voltage imposed by the control system, as indicted in the figure, because the submodules have not yet received the command to turn off. Since the voltage at the DC side of the converter drops to values close to zero, the voltage resulting from the series of the AC voltage sources and the submodules inserted is applied to the inductors. The maximum voltage that can result applied on a inductor is:

$$V_{\text{L,max,1}} \approx \frac{V_{\text{d,ref}} + \hat{v}_{\text{ll}}}{2}. \tag{2.36}$$

where $V_{\text{d,ref}}$, which is corresponds to the reference voltage on the DC side, is also the DC voltage just before the breakdown and $\hat{v}_{\text{ll}}$ is the peak value of the line to line voltage on the AC side.

The second phase begins once the IGBTs are turned off and lasts until all arm currents are driven to zero, which usually takes in the order of 100 µs. The direction of the currents remains the same from the previous phase, so the circuit that follows the circuit in figure 2.14 is illustrated in figure 2.15, which depicts the situation for a FB-based MMC. The resulting current loops are composed by two arms and two AC voltage sources. Depending on the topology of the converter and on the sign of the current flowing in the loop, a number of capacitors will result in series in this loops and the voltage difference between the series of the capacitors and the sum of the instant values of the AC voltages in the path will be applied to the two inductors. In a FB-based MMC, depicted in figure 2.15, all the submodules

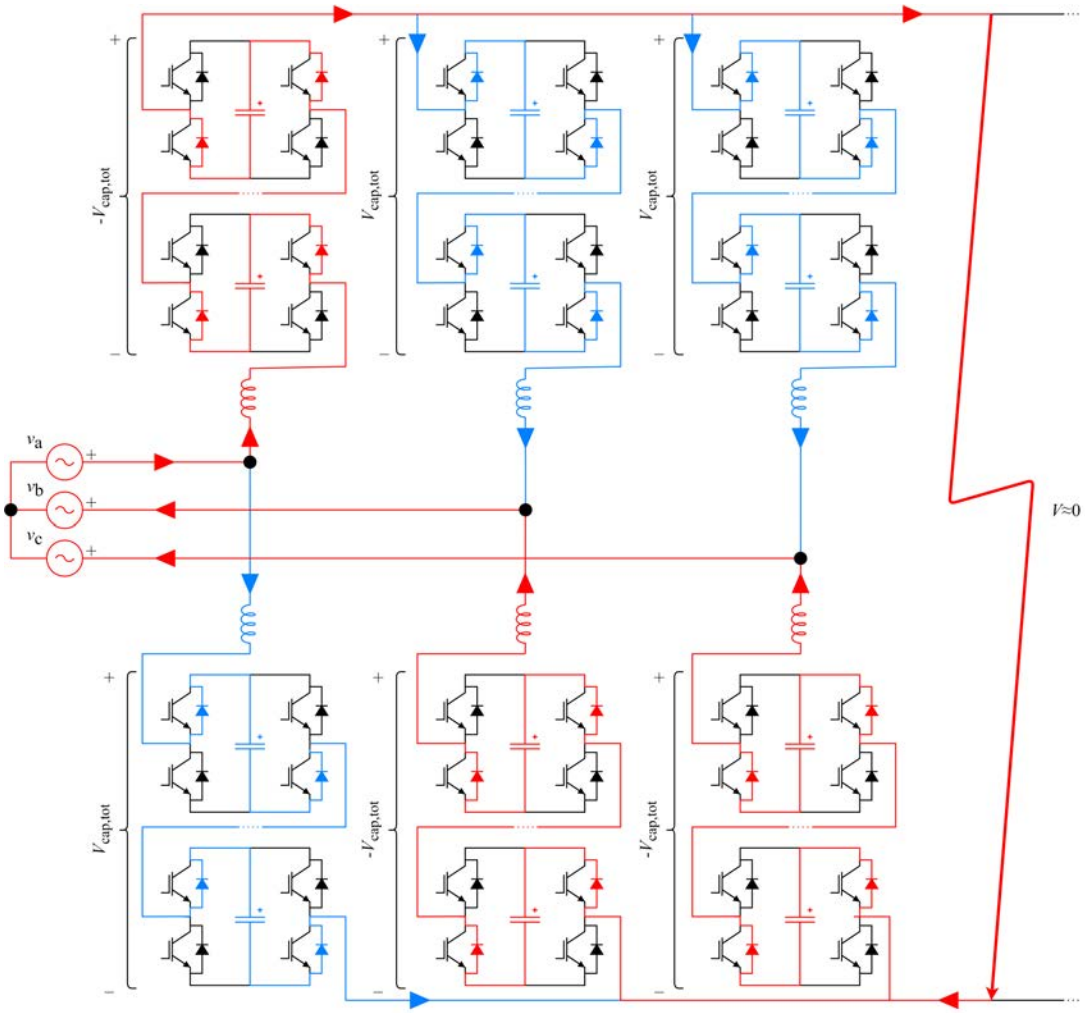

Figure 2.15: Possible schematic of a MMC in case of a short-circuit at the DC side after the IGBTs have been turned off. The current paths are drawn in red and blue.

capacitors will result in series and the arm voltage will result $-V_{\text{cap,tot}}$ with positive arm current, and $+V_{\text{cap,tot}}$ with negative arm current. For hybrid MMCs the situation is slightly different and will be analysed in section 4.3. In any case, the voltage resulting from series of the AC voltage sources and the submodule capacitors is applied to the inductors. The maximum voltage that can result applied on a inductor is:

$$V_{\text{L,max,2}} \approx V_{\text{cap,tot}} + \frac{\hat{v}_{\text{ll}}}{2}, \tag{2.37}$$

which is much more severe than what results from 2.36 since it is larger and will last much longer. Also, $V_{\text{L,max,1}}$ is dependent on the operating point of the converter, for lower DC voltages the overvoltage becomes lower, while $V_{\text{L,max,2}}$ is the same for any value of DC voltage, as $V_{\text{cap,tot}}$ does not change for different DC voltages.

The overvoltage over the arm inductors requires to use an adequate distance from the others components of the MMC, thus this should be minimised as possible in order to reduce the area occupied. Two solutions to mitigate the issue of the large space required by the arm inductors will be proposed for the hybrid topology in section 4.3.

Once the current starts to flow through the capacitors, those will be charged until the total voltage will

be enough to block the current, so until the following inequality will be satisfied [21]:

$$\sum_{i=1}^{N_\mathrm{f}} \left(v^i_{\mathrm{cap,u}} + v^i_{\mathrm{cap,l}} \right) \geq \hat{v}_{\mathrm{ll}}, \tag{2.38}$$

where $\hat{v}_{\mathrm{ll}}$ is the peak of the line to line AC voltage, and N_f the number of submodules with fault-blocking capabilities. In order to ensure that the capacitors in case of breakdown are not charged too much and the voltages remain close to their nominal value, N_f has to be opportunely chosen with the following inequality:

$$N_\mathrm{f} \geq \frac{\hat{v}_{\mathrm{ll}}}{2\, V_{\mathrm{cap,nom}}}. \tag{2.39}$$

Using a larger number of submodules with fault-blocking capabilities will ensure a faster blocking of the arm currents.

Chapter 3

Unidirectional MMC

3.1 Introduction to the uMMC

Since the output current in the AGPS should be always flowing in the same direction, using a unidirectional scheme would simplify the system and reduce the number of components used. A unidirectional MMC (uMMC) would employ the submodules described in subsection 2.2.2. Such submodules are very different from conventional ones, and the control strategy must be opportunely modified. The scheme of the converter is similar to the one in figure 2.1, with the only difference that uMMC lacks of the arm inductors L_{arm}, while the phase inductors L_{phase} are still present. For this reason, this converter would be very attractive to be used as AGPS for the NBI of DTT. The volume occupied would be remarkably reduced, as the arm inductors take a significant fraction of the total space.

The uMMC has been deeply reviewed in [24], where a suitable control strategy has been developed and tested with simulations. In [24, 25, 26] the unidirectional converter makes use of just uHB submodules, but those alone cannot provide the DC-fault blocking capability, so to make the converter able to block the arm currents in case of breakdown uFB submodules would be added, which would operate as the other uHB in normal conditions. This kind of topology, even if it presents appealing advantages for unidirectional converters, has not yet been tested on a physical prototype and further research would be required. In this chapter will be presented this topology, its operating principles and the control system, in order to asses his capabilities. As will be explained in section 3.3, it has been proved that the uMMC cannot satisfy all the requirements of the AGPS of the DTT NBI, specifically regarding the DC voltage regulation from 20 to 100% of the nominal value.

3.2 Operation and control strategy

In subsection 2.2.2 it has been stated that unidirectional submodules require a negative arm current to charge the capacitors and, while the current is negative, the submodule would not no longer be controllable. In order to have a zero net energy flow in the capacitor in each period, the uMMC has to synthesise suitable arm currents that have also to produce AC currents on one side and a DC current on the other at the same time. In [26] it has been proposed a possible set of current waveforms, depicted in figure 3.1a. In the figure the subscripts p and n are the respective equivalent of the u and l subscripts that stand for upper and lower arm.

The current flows through four arms at every time, three of them with positive current and the fourth with negative current, while the remaining two arms do not conduct. In this way three arms are controlled and able to impose the input and output voltages, while the other has its capacitors recharged by the negative current. Dividing the grid period in six sectors, from s_1 to s_6, every arm will conduct negative current once every period for a whole sector, will conduct positive current for three sectors and will be not used for two sectors. In the sector when the arm current is negative, each capacitor has to receive as much energy as it provides during the three sectors when the arm current is positive, so the resulting energy flow is zero and the capacitors remain balanced. In figure 3.1b are plotted the resulting current,

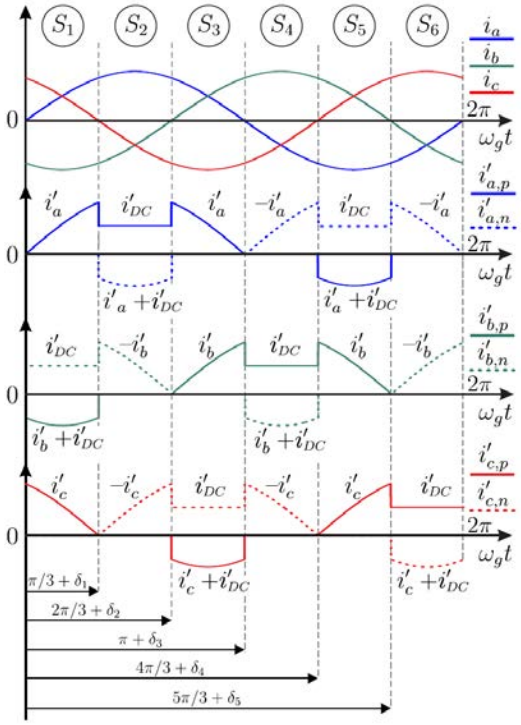

(a) Ideal arm current waveforms.

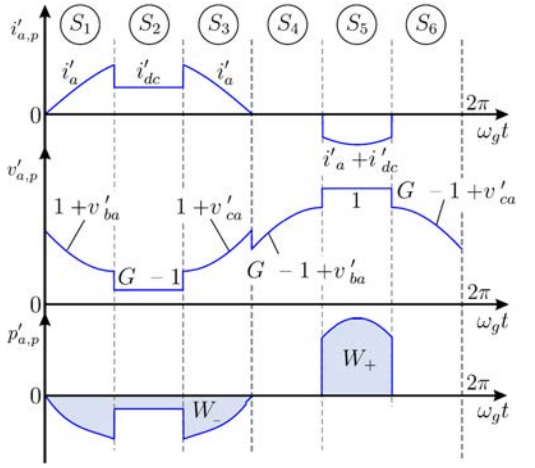

(b) Ideal current, voltage and power waveforms of the upper arm of phase a.

Figure 3.1: Ideal current, voltage and power waveforms in a uMMC. Figures respectively from [25, 26].

voltage and power for the upper arm of phase a. The voltage values have been normalised in respect to the total capacitor voltage of an arm $V_{\text{cap,tot}}$ and G corresponds to the normalised DC voltage. As can be noted from the picture, during the sector with negative arm current, the arm voltage is the total capacitor voltage of the arm as all capacitors of the arm are resulting in series without the possibility of being bypassed.

By properly adjusting the duration of each sector is possible to control the charge and discharge times of the capacitors of each arm and thus control the energy balancing among the arms. The nominal length of each sector is $\frac{\pi}{3}$, modified by the values of δ_i, with $i = 0, \ldots, 5$, as depicted in figure 3.4a. The value of the δ_i are computed each period in order to balance the energy, and at steady-state they should get close to zero. As a consequence of this strategy, there are no circulating currents.

In figure 3.2 is illustrated the diagram of the control system for a uMMC, whose blocks will be described in the following subsections.

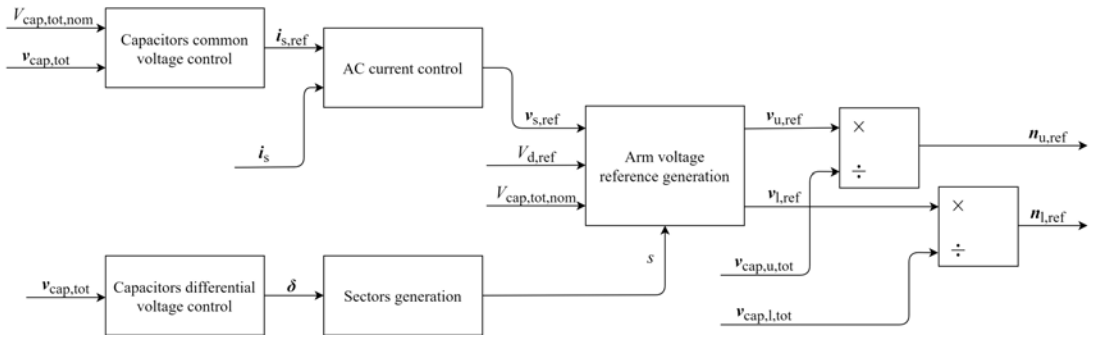

Figure 3.2: Simplified diagram of the control system for a uMMC.

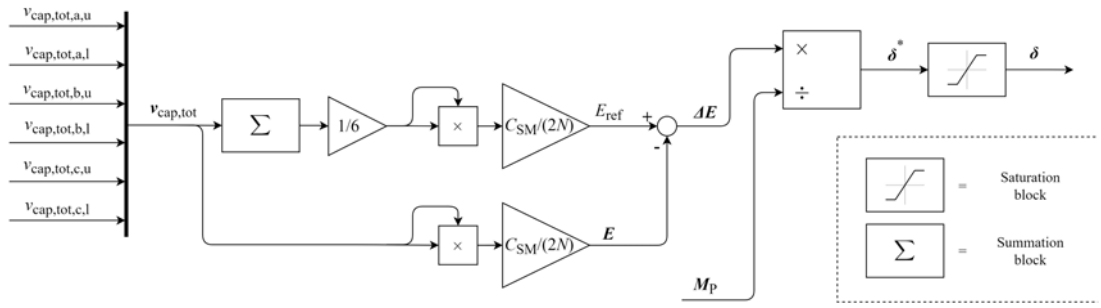

Figure 3.3: Capacitor differential voltage control diagram for a uMMC.

3.2.1 Capacitor differential voltage balance

In order to maintain the total arm capacitors voltage balanced it is possible to control the sector time shifts δ_i in order to vary the energy flow in the capacitors each grid period. This control has the purpose of converging the total capacitor voltage of each arm to the average value of all arms. Its diagram it is represented in figure 3.3. The sector time shifts can be gathered as in the following:

$$\boldsymbol{\delta} = \begin{pmatrix} \delta_0 & \delta_1 & \delta_2 & \delta_3 & \delta_4 & \delta_5 \end{pmatrix}^\top. \tag{3.1}$$

The influence of δ_1 on the phase a is reported as an example in figure 3.4a. At the beginning of every grid period it is computed the mean energies stored in the previous period in the capacitors of each arm, and its difference with the average value of all arms. The energies in the arms are computed as follows:

$$\boldsymbol{E} = \frac{1}{2}\frac{C_{SM}}{N}\boldsymbol{v}_{cap,tot}^2, \tag{3.2}$$

where $\frac{C_{SM}}{N}$ corresponds to the equivalent capacitance of an arm and $\boldsymbol{v}_{cap,tot}$ is the vector containing the total capacitor voltage of each arm. The average energy of all arms is computed as follows:

$$E_{ref} = \frac{1}{2}\frac{C_{SM}}{N}\left(\sum_{\phi=a,b,c}\frac{v_{cap,tot,u,\phi} + v_{cap,tot,l,\phi}}{6}\right)^2. \tag{3.3}$$

The difference between E_{ref} and the components of $\boldsymbol{E}$, denoted with $\boldsymbol{\Delta E}$, indicates how much energy every arm would need in order to reach the average value in the following grid period, and it has a component per arm, as follows:

$$\boldsymbol{\Delta E} = \begin{pmatrix} \Delta E_{u,a} & \Delta E_{l,a} & \Delta E_{u,b} & \Delta E_{l,b} & \Delta E_{u,c} & \Delta E_{l,c} \end{pmatrix}^\top. \tag{3.4}$$

It can be also expressed as:

$$\boldsymbol{\Delta E} \approx \boldsymbol{M}_P \cdot \boldsymbol{\delta}, \tag{3.5}$$

where $\boldsymbol{M}_P$ is a matrix which contains coefficients that approximate the variation of power flowing in each arm after every sector change. The multiplication of the matrix by the vector containing the time shifts gives as result an approximation of the net energy which flows into each arm in that period, which in ideal conditions should be zero. The variation of the net energy caused by a sector shift can be observed in the lower plot in figure 3.4b. The matrix $\boldsymbol{M}_P$ can be calculated as:

$$\boldsymbol{M}_P = \begin{pmatrix} 0 & k_1 & -k_1 & 0 & k_2 & -k_2 \\ 0 & k_2 & -k_2 & 0 & k_1 & -k_1 \\ k_2 & -k_2 & 0 & k_1 & -k_1 & 0 \\ k_1 & -k_1 & 0 & k_2 & -k_2 & 0 \\ -k_1 & 0 & k_2 & -k_2 & 0 & k_1 \\ -k_2 & 0 & k_1 & -k_1 & 0 & k_2 \end{pmatrix}, \tag{3.6}$$

where k_1 and k_2 are defined as follows:

$$k_1 = -\frac{\sqrt{3}}{2} V_{\text{cap,tot}} \cdot \hat{i}_\text{s} + (V_\text{d} - V_{\text{cap,tot}}) \cdot I_\text{d} \tag{3.7a}$$

$$k_2 = \left(I_\text{d} - \frac{\sqrt{3}}{2} \cdot \hat{i}_\text{s} \right) \cdot V_{\text{cap,tot}}. \tag{3.7b}$$

The expression for k_1 derives from the the difference between the power at the end of s_1 and the start of s_2 in figure 3.1b. Analogously, the expression for k_2 derives from the the difference between the power at the end of s_4 and the start of s_5. All the power differences, for each combination of arm and δ_i, can be considered substantially equal in module to k_1 or k_2, expect when they negligible, e.g. between s_3 and s_4 and between s_6 and s_1 in figure 3.1b. They represent an approximation of the power absorbed by the arm during δ_i. It has been considered that, for small values of $\boldsymbol{\delta}$, the power remains approximately constant in the instants before the sector change or in the instants after. Depending on the signs of the variation of power at the end of the ith sector and of the δ_i, the net energy of an arm will result positive or negative, thus the capacitors will be charged or discharged.

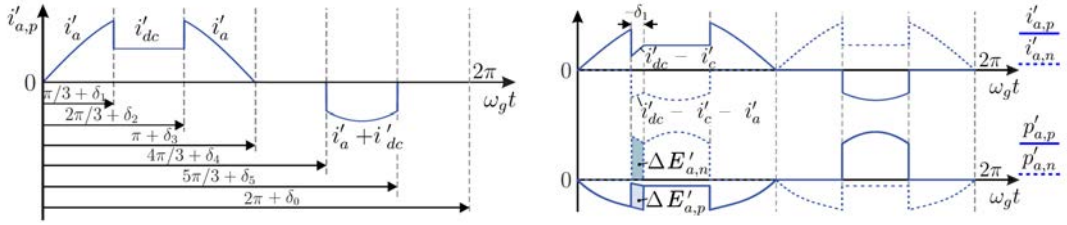

(a) Definition of the sectors shifts with respect to an arm reference current.

(b) Example on the influence of δ_1 on the current and power of a phase.

Figure 3.4: Definition and effects of the δ_i. Figures from [26].

The two coefficients k_1 and k_2 and the matrix $\boldsymbol{M}_\text{P}$ can be computed once and are valid throughout the whole operation, if the DC voltage reference remains constant. The vector $\boldsymbol{\delta}$ is obtained by solving the matrix equation 3.6.

The components of the vector $\boldsymbol{\delta}$ has to pass through a saturation block to limit the values, as the approximations used to calculate $\boldsymbol{M}_\text{P}$ in equation 3.6 are valid just for small values of $\boldsymbol{\delta}$. The "Sectors generation" in figure 3.2 uses the sector time shifts to divide the grid period into 6 sectors and outputs the current sector s.

3.2.2 Capacitor common voltage balance

This block controls the common component of the capacitor voltages, which corresponds to the average total capacitor voltage of all arms, and makes it converge to the nominal total capacitor voltage in an arm, $V_{\text{cap,tot,nom}}$. The control diagram is present in figure 3.5. After computing the average value of the total capacitor voltage of all arms, the value is subtracted from the nominal total capacitor voltage in an arm. The error is regulated by a PI controller, which outputs the reference value of the AC currents $\boldsymbol{i}_{\text{s,ref}}$.

3.2.3 AC currents control

For the control of the AC currents it has been used a similar scheme to the one used in conventional MMCs, which is explained in subsection 2.4.2. The main difference is that, instead of multiplying the $dq0$ components of the AC current vector by $0.5 \cdot \omega\, L_\text{arm}$, they are multiplied by $\omega\, L_\text{phase}$, since the arm inductors are no longer present in this topology.

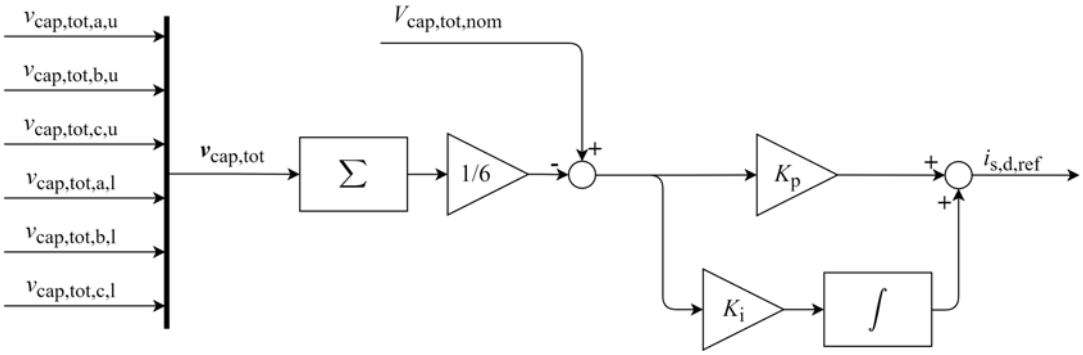

Figure 3.5: Capacitor common voltage control diagram for a uMMC.

3.2.4 Arm voltage references generation

In order to produce the current waveforms depicted in figure 3.1a, the control system needs to compute the reference arm voltages as reported in table 3.1. During each sector the voltage references assume different expressions, which are combinations of the input signals $V_{d,ref}$, $V_{d,ref}$ and $V_{cap,tot,nom}$. The resulting voltage of the upper arm of phase a is plotted in figure 3.1b.

Each arm voltage reference of $\boldsymbol{v}_{u,ref}$ and $\boldsymbol{v}_{l,ref}$ is then divided by the total capacitor voltage of its arm to reduce the oscillations caused by the ripple of the discharging capacitors. The result are the insertion indices $\boldsymbol{n}_{u,ref}$ and $\boldsymbol{n}_{l,ref}$, which will be used to generate the gate signals.

Table 3.1: Expressions of the arm voltage reference signals for each sector. Table from [24].

	s_1	s_2	s_3
$v_{u,a,ref}$	$V_{cap,tot} + v_{s,b} - v_{s,a}$	$-V_{cap,tot} + V_d$	$V_{cap,tot} + v_{s,c} - v_{s,a}$
$v_{l,a,ref}$	$-V_{cap,tot} + V_d + v_{s,a} - v_{s,b}$	$V_{cap,tot}$	$-V_{cap,tot} + V_d + v_{s,a} - v_{s,c}$
$v_{u,b,ref}$	$V_{cap,tot}$	$-V_{cap,tot} + V_d + v_{s,a} - v_{s,b}$	$V_{cap,tot} + v_{s,c} - v_{s,b}$
$v_{l,b,ref}$	$-V_{cap,tot} + V_d$	$V_{cap,tot} + v_{s,b} - v_{s,a}$	$-V_{cap,tot} + V_d + v_{s,b} - v_{s,c}$
$v_{u,c,ref}$	$V_{cap,tot} + v_{s,b} - v_{s,c}$	$-V_{cap,tot} + V_d + v_{s,a} - v_{s,c}$	$V_{cap,tot}$
$v_{l,c,ref}$	$-V_{cap,tot} + V_d + v_{s,c} - v_{s,b}$	$V_{cap,tot} + v_{s,c} - v_{s,a}$	$-V_{cap,tot} + V_d$

	s_4	s_5	s_6
$v_{u,a,ref}$	$V_{cap,tot} + V_d + v_{s,b} - v_{s,a}$	$V_{cap,tot}$	$-V_{cap,tot} + V_d + v_{s,c} - v_{s,a}$
$v_{l,a,ref}$	$V_{cap,tot} + v_{s,a} - v_{s,b}$	$-V_{cap,tot} + V_d$	$V_{cap,tot} + v_{s,a} - v_{s,c}$
$v_{u,b,ref}$	$-V_{cap,tot} + V_d$	$V_{cap,tot} + v_{s,a} - v_{s,b}$	$-V_{cap,tot} + V_d + v_{s,c} - v_{s,b}$
$v_{l,b,ref}$	$V_{cap,tot}$	$-V_{cap,tot} + V_d + v_{s,b} - v_{s,a}$	$V_{cap,tot} + v_{s,b} - v_{s,c}$
$v_{u,c,ref}$	$-V_{cap,tot} + V_d + v_{s,b} - v_{s,c}$	$V_{cap,tot} + v_{s,a} - v_{s,c}$	$-V_{cap,tot} + V_d$
$v_{l,c,ref}$	$V_{cap,tot} + v_{s,c} - v_{s,b}$	$-V_{cap,tot} + V_d + v_{s,c} - v_{s,a}$	$V_{cap,tot}$

3.2.5 Gate signals generation

The insertion indices $\boldsymbol{n}_{u,ref}$ and $\boldsymbol{n}_{l,ref}$ are used to produce the gate signals to command the IGBTs with a PS carrier modulation.

Since the unidirectional submodules are not controllable in case of negative arm current, the gate signals are disabled during the sectors when an arm is supposed to stay inactive. With a positive phase current, the relative upper arm will remain active and the lower arm will be deactivated, and vice versa with a negative phase current, the relative upper arm will be deactivated and the lower arm will remain active.

3.3 Considerations on the uMMC

The main advantages provided by the uMMC converter are the reduction of components needed by the converter and the lack of arm inductors, which translates on a more compact converter. It would be the MMC topology with the lowest number of IGBTs by a considerable margin among the HB-based, the FB-based and the hybrid MMCs. Removing the arm inductors would reduce the volume of the converter significantly. However, the reduced number of components have repercussions on the flexibility of the operation of the converter. Since there are no circulating currents, the voltage balancing of the capacitors is mainly accomplished by the AC currents. When operating with lower currents, it would be harder to balance effectively the capacitors. The main limitation is the operational range of such converters, which in [24] has been shown to be much narrower than that of HB-based MMCs.

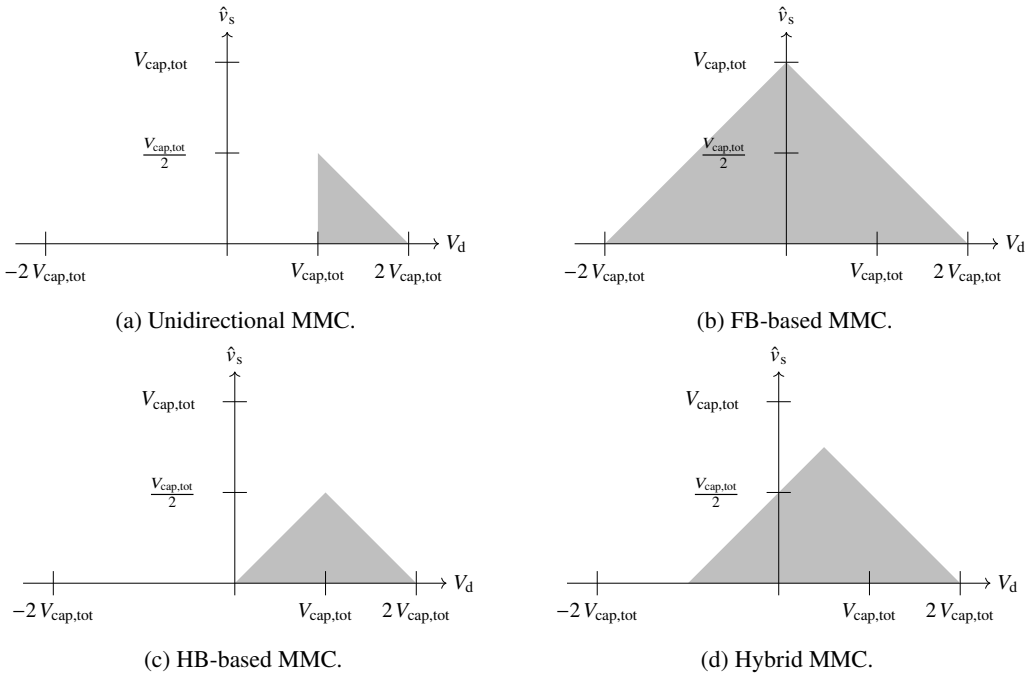

(a) Unidirectional MMC.

(b) FB-based MMC.

(c) HB-based MMC.

(d) Hybrid MMC.

Figure 3.6: Operating regions of different MMCs.

In figure 3.6 are reported for comparison the operating regions of different MMCs: the uMMC, the FB-based MMC, the HB-based MMC and a hybrid MMC with half FB and half HB submodules. For the uMMC, the minimum DC voltage that can be produced is limited by the value of the total capacitor voltage in an arm and it cannot be produced a DC voltage below that value.

An important requirement of the AGPS is the adjustment of the DC voltage within a range from 20% to 100% of the nominal DC voltage $V_{d,nom}$. In theory, a possible way to produce a voltage which is 20% of the nominal voltage would be to discharge all the capacitors until they reach a total capacitor voltage equal to 20% of $V_{d,nom}$ in each arm. The AC voltage peak value would have to be maximum 10% of $V_{d,nom}$, which would be very low. To operate with DC voltages higher than the minimum voltage, the capacitors would have to be charged to a level where the total capacitor voltage in each arm is equal at least to half the value of the desired DC voltage, even somewhat higher. This choice does not seem very practicable for a variety of reasons. A very low AC voltage implies large currents on the AC side of the converter and in the arms, and consequently a considerable ripple on the capacitors. The capacitors would require a large capacitance to attenuate the voltage fluctuation during the operation nearby the nominal DC voltage to avoid having voltage fluctuations also in V_d. The voltage on all capacitors would have to be ramped up from a low value to the nominal voltage at the beginning of every operation in relatively short times, in less than 80 ms, which may be impossible to accomplish in just four grid periods while keeping the arms balanced with the modulation method proposed. Operating with variable voltage on the capacitors is generally avoided in MMC applications.

An important thing to consider is that the uMMC is not, yet, at a development stage advanced enough to be used as a high-voltage power supply, since it has not yet been tested on physical prototypes. In [24, 25, 26] it has been tested with just numerical simulations.

Due to the above-mentioned reasons, it has been chosen to not pursue the study of the uMMC and instead continue with the analysis of the hybrid MMCs, which is a topology more affirmed and has proved to be capable of operating with the requirements in table 1.5.

Chapter 4

Hybrid symmetric MMC

4.1 Introduction to the hybrid MMC

A hybrid MMC is composed by both FB and HB submodules. It maintains some features of the FB-based MMC while using a smaller number of power components. There are two categories of hybrid converter: the symmetric hybrid MMC, which presents an equal number of HB and FB submodules in upper and lower arms, and the asymmetric hybrid MMC, which presents only HB in the upper arms and only FB in the lower arms, or vice versa. The symmetric hybrid MMC is generally a much popular solution, in fact in literature is it usually referred just as hybrid MMC. In the following, the symmetric version will referred just as hybrid MMC, while the asymmetric version, which will be discussed in chapter 5, will be referred as hybrid asymmetric MMC. A general schematic of the hybrid topology is reported in figure 4.1.

In case of a breakdown all the HB submodules are bypassed, and the blocking of the AC currents is carried out by the FB modules, but since their number is lower than in FB-based MMCs, it is important to verify that their total voltage is enough. The capacitor voltage balance strategy for HB-based MMCs does limit the operational capabilities of the hybrid MMC and the one for FB-based MMCs is not compatible with the HB submodules present, therefore an appropriate control technique must be adopted.

HB submodules can charge their capacitors only when a negative current is flowing in the arm and discharge them with a positive current, instead FB submodules can charge and discharge them with current of any polarity. In order to maintain balanced the submodule capacitors, it is fundamental that the arm currents become positive and negative during each period, otherwise there is the risk that the capacitors of the HB submodules are no longer balanced with the FB submodules, and in the more severe cases the imbalance can diverge.

Hybrid MMC are generally researched for applications, such as HVDC transmission, that require little flexibility, as the operation of the converter in normal conditions remain close to the nominal parameters. Instead, for the application to the AGPS for DDT NBI, the converter needs to produce a wide range of DC output voltages with a fixed input AC voltage.

In the following subsection will be investigated the main requirements of this topology in order to guarantee a stable operation. In section 4.2 will be presented the control scheme of an hybrid MMC. After the overview of the hybrid topology in this chapter, in chapter 6 will be carried out an preliminary design of the main parameters required by an hybrid MMC in order to be used as the AGPS for the NBI of DTT. Then, in chapter 7 will be presented and discussed the results of the computer simulations of such converter. In its last section, 7.4, will be given some considerations regarding the hybrid MMC with the hindsight of the results obtained.

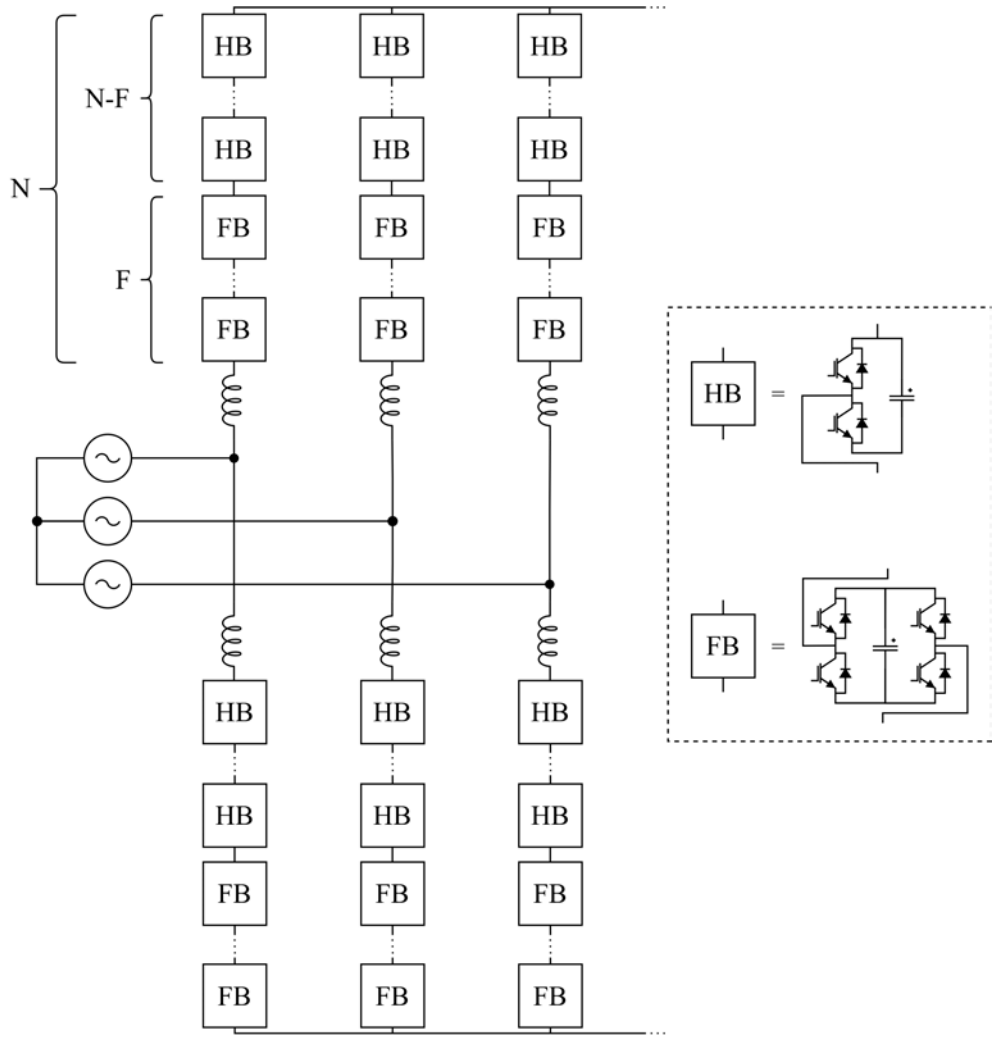

Figure 4.1: Schematic of a three-phase hybrid MMC converter.

4.1.1 Operational requirements

When analysing hybrid MMC is useful to introduce additional parameters: N is the total number of submodules in each arm, F is the number of FB submodules in each arm and M the number of FB submodules allowed to produce a negative voltage in each arm; it is clear that $F \geq M$.

An HB-based MMC can work with modulation index up to 1; additional FB submodules are required in order to overcome this limit, while a FB-based MMC could, in theory, work with any modulation index. In [27] it has been proven that the modulation index m for a hybrid MMC must be lower than 2 and the maximum number of submodules allowed to produce a negative voltage is $M \leq \frac{N}{3}$ in order to operate with balanced energy in the capacitors. The HB submodules require an arm current with positive and negative values in each period and this condition is satisfied only for $m \leq 2$. It is important to note that in practical applications m should be even somewhat lower, since for the border condition $m = 2$ the arm current does not become negative, but just reaches zero [28]. In figure 4.2 is plotted the minimum number of FB submodules required for an optimal operation in a hybrid MMC, for different values of m and the minimal DC voltage obtainable, $V_{\mathrm{d,min}}$, normalised with respect to the DC voltage obtained with modulation index equal to 1. For lower values of $V_{\mathrm{d,min}}$, the HB submodules are simply bypassed and most of the operation is carried out by the remaining submodules, hence the required number of FB submodules for low or negative $V_{\mathrm{d,min}}$ becomes very high, about 80% of the total submodules. In order to avoid using a large fraction of FB submodules, it has been considered to use $M = \frac{N}{3}$, which is a good compromise between the minimum DC voltage producible and an acceptable number of FB

submodules. F should be chosen equal to the largest between M and N_f, since the former value may not be large enough to nullify the arm currents in case of breakdown.

The AGPS needs to be able to adjust the DC voltage at least from 20 to 100% of the nominal value, $V_{d,nom}$, as noted in table 1.5. This means that the modulation index m, since the AC voltage cannot be adjusted, has to be varied to produce the required DC voltage levels. The MMC cannot generate a DC voltage with an arbitrary AC voltage, which means that the voltage on the AC side has to be carefully chosen. To guarantee the operation also for low levels of V_d, the AC voltage has to be relatively low with respect to common applications. The AC voltage is determined in the condition with the lowest DC voltage that needs to be produced, $V_{d,min}$, using a reasonable modulation index that could guarantee the energy balance. The hybrid MMC will operate with a modulation index within 1 and 2 for $V_{d,min}$, and below 1 for $V_{d,nom}$. In the latter operation all submodules would work equivalently to HB submodules, producing just positive voltage. Increasing the AC voltage helps in reducing the ripple on the submodule capacitors. The nominal total capacitor voltage of the arms $V_{cap,tot}$ is determined in the condition with the highest DC voltage that needs to be produced. Due to the presence of FB modules, the operating region of a hybrid MMC is slightly larger than for a HB-based MMC, but still less than for a FB-based MMC.

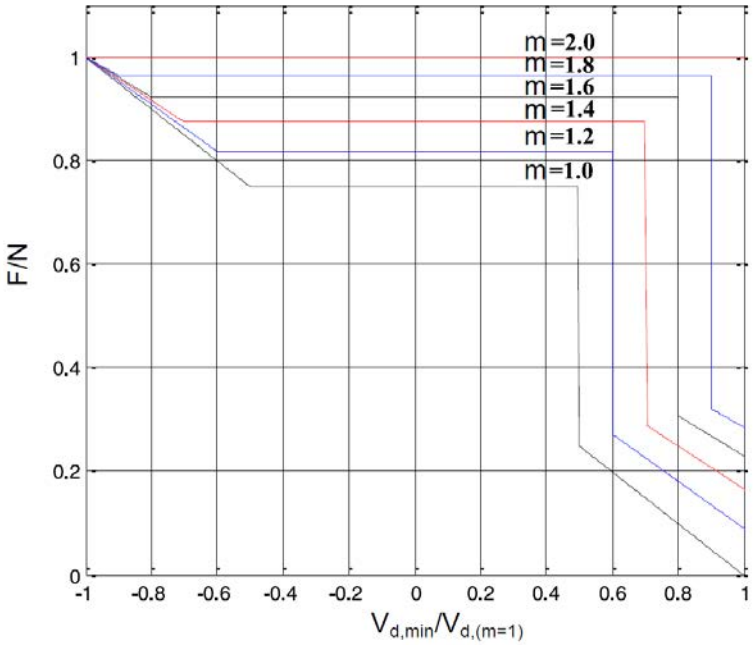

Figure 4.2: Minimum number of FB submodules in function of the minimum DC voltage producible and of the modulation index. Figure from [28].

4.2 Control strategy

The control strategy that has been employed for the hybrid MMC follows the same diagram depicted in figure 2.9. The blocks upstream the "Arm voltage control" are based on conventional control schemes, presented in 2.4, that are valid also for HB and FB-based MMCs. The remaining part of the control has to be specific for hybrid topologies. Most of the control techniques proposed for hybrid MMCs, which are based on Phase Shifted carriers, are not valid with a modulation index over 1. In [29] it has been proposed a solution to adapt the PS control to operate with larger m. The improved technique involves a modification of the reference waves, a different arrangement of the carriers and a modified capacitor sorting algorithm, which will be presented in the following subsections.

4.2.1 Arm voltage control

The reference waves are generally computed as follows:

$$v_{\mathrm{u,ref}} = \frac{1}{2} V_{\mathrm{d}} - v_{\mathrm{s,ref}} - v_{\mathrm{c,ref}} \tag{4.1a}$$

$$v_{\mathrm{l,ref}} = \frac{1}{2} V_{\mathrm{d}} + v_{\mathrm{s,ref}} - v_{\mathrm{c,ref}}, \tag{4.1b}$$

where $v_{\mathrm{u,ref}}$ is the reference for the upper arm and $v_{\mathrm{l,ref}}$ for the lower arm. The reference waves are turned into their absolute value: when the signal becomes negative the negative part is turned over. With this modification, the reference signals are now between 0 and 1 as the PWM carriers. The resulting insertion indices, which have been normalised with respect to $V_{\mathrm{cap,tot}}$, are:

$$n_{\mathrm{u}} = \frac{\left|\frac{1}{2} V_{\mathrm{d}} - v_{\mathrm{s,ref}} - v_{\mathrm{c,ref}}\right|}{V_{\mathrm{cap,tot}}} \tag{4.2a}$$

$$n_{\mathrm{l}} = \frac{\left|\frac{1}{2} V_{\mathrm{d}} + v_{\mathrm{s,ref}} - v_{\mathrm{c,ref}}\right|}{V_{\mathrm{cap,tot}}}. \tag{4.2b}$$

The insertion indices are then sent to the block "Gate signal generation" as in figure 2.9, which has been modified as will be explained in the following subsection.

4.2.2 Gate signal generation

The number of modules to be inserted are generated using the PS carrier modulation. As the phase shift angle between the N carriers of the same arm it has been used $\frac{2\pi}{N}$, and the angular displacement between the upper and lower arm is chosen as follows:

$$\theta = \begin{cases} 0, & \text{if } (N - F) \text{ is even.} \\ \frac{\pi}{N}, & \text{if } (N - F) \text{ is odd.} \end{cases} \tag{4.3}$$

When the reference signal, n_{u} or n_{l}, is larger than the carrier the submodule is commanded to produce $+V_{\mathrm{cap,nom}}$ in case the original signal was already positive, otherwise $-V_{\mathrm{cap,nom}}$ if the original signal was negative. When the reference signal is smaller than the carrier the submodule is bypassed. With such control, the FB submodules are controlled as they were HB submodules at low values of m and high DC voltages. Their capability to produce negative voltage is exploited when the original signal becomes negative for higher values of m and lower DC voltages.

4.2.3 Capacitor voltage balance algorithm

After the number of submodules to be inserted has been computed to synthesise the requested voltage levels in the arms, it is possible to adopt a sorting algorithm to keep the capacitors voltage balanced [28]. When the voltage to be produced is positive, HB and FB submodules are equally considered by the control system. If the arm current is positive, it will be inserted the submodules with the highest voltage. Otherwise, if the arm current is negative, it will be inserted the submodules with the lowest voltage. When the voltage to be produced is negative, HB submodules will be bypassed as only FB submodules are able to produce a negative voltage. If the arm current is positive, will be negatively inserted the FB submodules with the lowest voltage, otherwise, if the arm current is negative, will be negatively inserted the FB submodules with the highest voltage. The diagram of such algorithm, which has to be implemented separately for each arm, is illustrated in figure 4.3.

4.3 Handling of breakdowns

In case of breakdown the AC current has to be blocked in order to limit the discharging of energy onto the accelerating grids. In the instant when the breakdown take place, half of the six arms currents are positive and half are negative. Counter-voltages have to be applied in order to drive the AC current to zero. Conventionally, in such situation, the procedure is to turn off all the IGBTs.

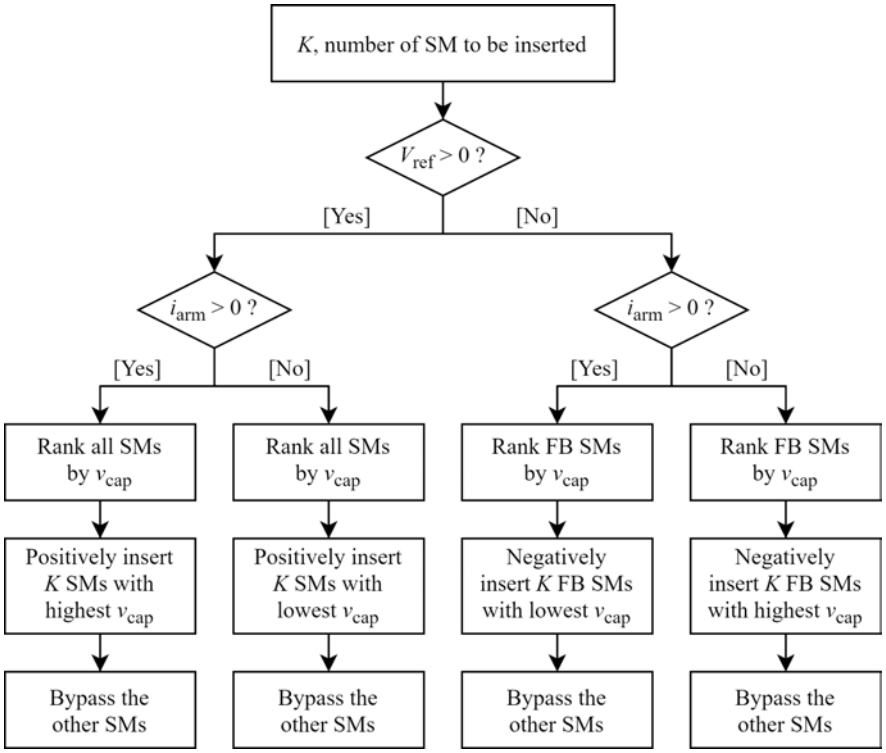

Figure 4.3: Diagram of the capacitor voltage balance algorithm.

Of two phases described in section 2.5, before and after the turn-off of the IGBTs, the first is equal also for hybrid MMCs, while the second is different. When all the IGBTs are turned off, in the arms where the current is positive only the capacitors of the submodules with fault-blocking capabilities, the FB, will appear in series, whereas the HB will be bypassed. Instead, in the arms where the current is negative all the capacitors of the arm will appear in series, of both FB and HB submodules. This will result on a very high voltage produced by the arms with negative current, equal to the total arm capacitors voltage $v^{\Sigma}_{\text{cap,u}}$ or $v^{\Sigma}_{\text{cap,l}}$, which is approximately $V_{\text{cap,tot}}$. This aspect can be considered positive for blocking the arm currents, as in those arms the current is blocked at a sensibly faster rate. On the other hand, part of this voltage will be applied to the arm inductors, causing a large overvoltage on such components. Two solutions have been proposed in order to overcome such problem.

Instead of switching off all the IGBTs, the HB submodules could be commanded into the bypass state, so, in the arms where the current is negative, the resulting voltage is no longer the total $v^{\Sigma}_{\text{cap,u}}$ or $v^{\Sigma}_{\text{cap,l}}$, but just the contributions of the capacitors of the FB modules. The overvoltage in the second phase would be greatly reduced. For example, using $F = \frac{N}{3}$ FB submodules, the maximum voltage on the inductors in any arm can reach up to:

$$V_{\text{L,max,2}} \approx F\, V_{\text{cap}} + \frac{\hat{v}_{\text{ll}}}{2} \approx \frac{V_{\text{cap,tot}}}{3} + \frac{\hat{v}_{\text{ll}}}{2}. \tag{4.4}$$

Since the overvoltage would reach a much smaller value than that found in equation 2.37, the clearance distance with the other components would be reduced. The maximum resulting arm voltage in the second phase would be the same for all the arms. In the arms with negative current, the current will decrease slower than before. It is important to verify that the time used to nullify the arm currents is still small enough to limit the discharged energy onto the accelerating grids to an acceptable value.

Instead of using a single inductor per arm, another solution could be to split it into multiple inductors with the same total equivalent inductance and assign them one to each submodule. Since the submodules are placed at proper distances to ensure the insulation during the operation and the overvoltage on the single inductors will be reduced N times, being the overvoltage on the single inductor approximately equal to the voltage of the submodule capacitor, the distances would be already suitable to guarantee the insulation. The submodules would grow in size as they would require an additional component, the

total volume occupied by the submodules would increase, but this would be counterbalanced by the fact that the inductors are already integrated in the submodules. The resulting volume of the converter could be reduced significantly by removing the single inductors and replacing them with smaller inductors distributed between the submodules. Such inductors would have to be compact in order to avoid to increase too much the volume of the submodule, and be rated for the full arm current, which can be in the order of 100 A.

Generally, conventional applications of MMC does not have strict limitations on the volume occupied, so the overvoltage on the inductors in case of a DC-fault is simply overcome by using adequate clearing distances with the other components, it does not pose as a problem. Further research is needed to assess whether these solutions could be employed and how much volume they could effectively save, as nothing similar has been found in literature.

Chapter 5

Hybrid asymmetric MMC

5.1 Introduction to the asymmetric hybrid MMC

A different topology of hybrid MMC has been proposed in [30], which introduces an asymmetric disposition of the HB and FB submodules in the converter legs: one arm per leg is composed by just HB submodules and the other is composed by just FB. The arms with HB submodules operates as a conventional HB-based MMCs, the arms with FB submodules operates as a conventional HB-based MMCs when operating at nominal conditions or slightly below, and as a FB-based MMCs when the DC voltage is further reduced. A scheme of such converter is depicted in figure 5.1. The upper arm is capable of producing a voltage from 0 to $N\,V_{\text{cap,nom}}$, while the lower arm from $-N\,V_{\text{cap,nom}}$ to $N\,V_{\text{cap,nom}}$.

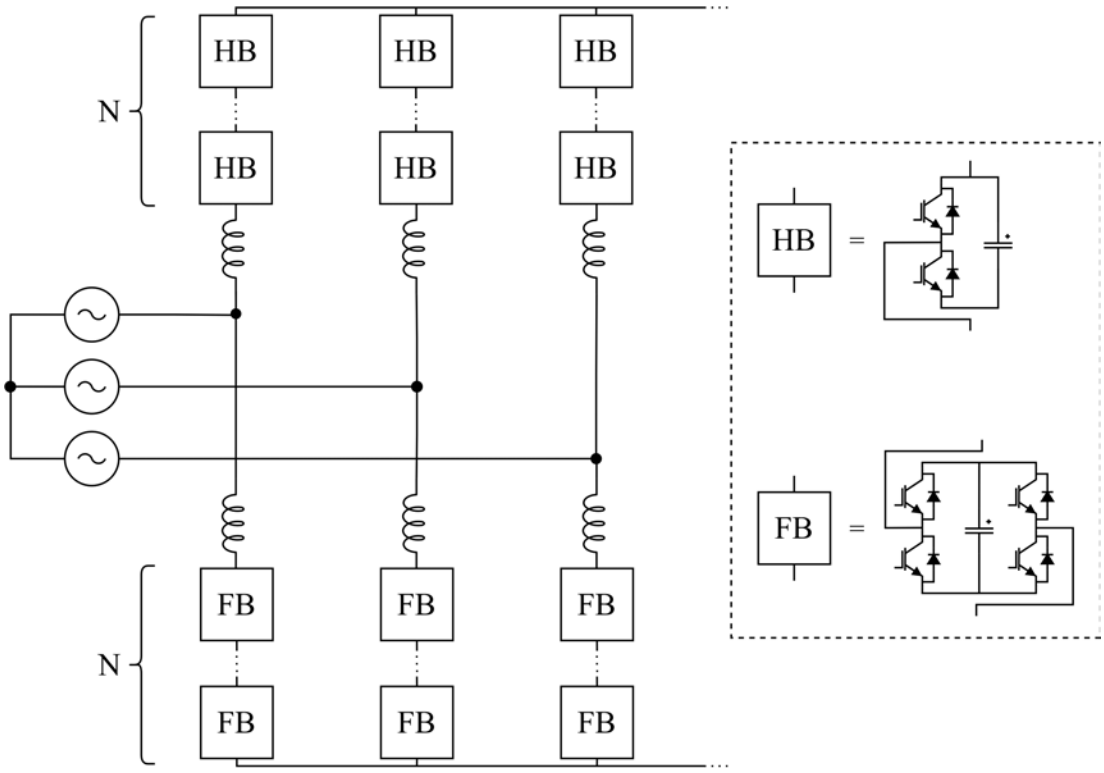

Figure 5.1: Schematic of a three-phase hybrid asymmetric MMC converter.

In figures 5.2 are presented the arm voltage reference and arm currents of both kind of hybrid MMC, the symmetric and asymmetric one, operating at a DC voltage lower than the nominal, specifically $V_{\text{d}} = 0.5\,V_{\text{d,nom}}$. The symmetric hybrid MMC, when it operates at lower voltages the arm voltage

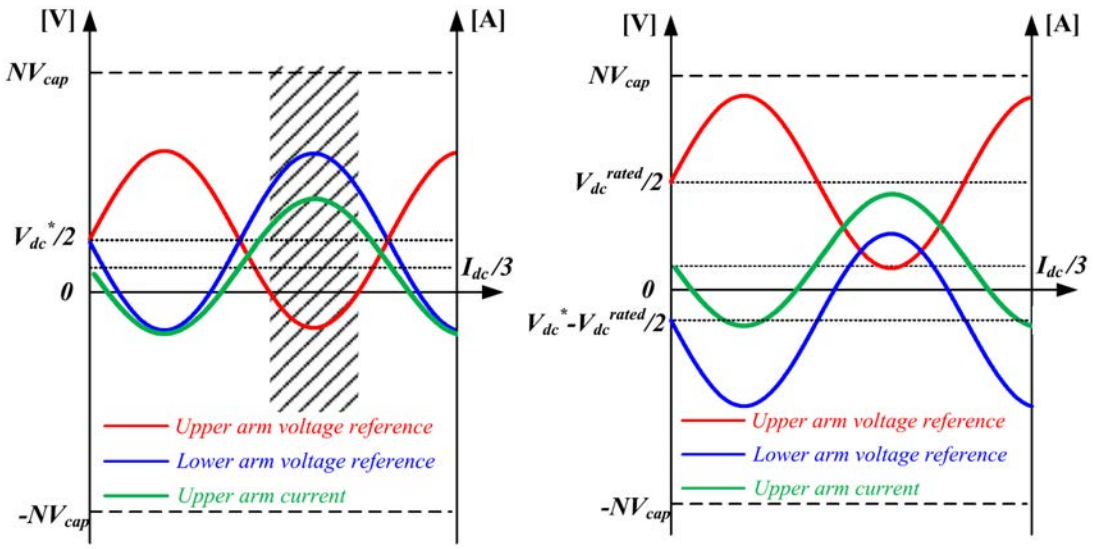

(a) Waveforms of a symmetric hybrid MMC.

(b) Waveforms of an asymmetric hybrid MMC.

Figure 5.2: Arm voltage references and arm current of symmetric hybrid MMC and asymmetric hybrid MMC. Figure from [30].

references can become negative, as has been marked in figure 5.2a for the upper arm. During such moments the HB submodules are bypassed as they are not able to produce negative voltage and the arm voltage is produced just by the FB submodules, whose capacitors get discharged while the capacitors of the HB submodules remain unchanged. This can lead to a uneven energy balance between the capacitors of FB and HB submodules, that gets larger as the V_{d} is decreased, resulting in a larger negative arm voltages references and for longer periods. Due to this reason, the lowest DC voltage that hybrid MMC can operate with is limited by maximum modulation index $m = 2$, as discussed in subsection 4.1.1, otherwise the submodules would not be balanced. It is possible to lower the AC voltage, as it has been discussed in subsection 6.1, to guarantee the operation for the full DC voltage range without exceeding m_{max}, but as it has been concluded can bring up some issues, for instance a large ripple on the capacitors.

Instead, the asymmetric hybrid MMC can maintain the upper arm voltage reference positive by keeping its DC component fixed at half the nominal DC voltage and opportunely regulate DC component of the lower arm voltage reference. As can be seen in figure 5.2b, when the asymmetric hybrid MMC is operating with lower DC voltages, only the lower arm voltage reference becomes negative, but since the lower arm is composed by only FB submodules, producing negative voltage is no longer problematic. The DC component of the lower arm voltage can be adjusted from $\frac{V_{\mathrm{d,nom}}}{2}$ to $-\frac{V_{\mathrm{d,nom}}}{2}$, with a resulting DC voltage V_{d} that ranges respectively from $V_{\mathrm{d,nom}}$ to zero. Thus the balancing of the capacitors between FB and HB submodules is guaranteed for a wide range of V_{d}, from 0 to 100% of the nominal value.

5.2 Control strategy

The control strategy adopted is nearly identical to the one employed for the hybrid MMC, described in section 4.2. The main differences are the computation of the modulations signals, which will be presented in the following subsection, and the capacitor voltage balance algorithm, that now is applied equally to all submodules of each arm.

5.2.1 Modulation signal generation

The reference arm voltages for the asymmetric hybrid MMC are computed as follows:

$$\boldsymbol{v}_{\mathrm{u,ref}} = \frac{V_{\mathrm{d,nom}}}{2} - \boldsymbol{v}_{\mathrm{s,ref}} - \boldsymbol{v}_{\mathrm{c,ref}} \tag{5.1a}$$

$$\boldsymbol{v}_{\mathrm{l,ref}} = \left(V_{\mathrm{d,ref}} - \frac{V_{\mathrm{d,nom}}}{2}\right) + \boldsymbol{v}_{\mathrm{s,ref}} - \boldsymbol{v}_{\mathrm{c,ref}}, \tag{5.1b}$$

where $V_{\mathrm{d,nom}}$ is the nominal DC voltage, while $V_{\mathrm{d,ref}}$ is the set DC voltage level, which can be adjusted from 0 to 100% of the nominal value. Using these expressions for calculating $\boldsymbol{v}_{\mathrm{u,ref}}$ and $\boldsymbol{v}_{\mathrm{l,ref}}$, guarantees that the upper voltage reference is always positive.

5.3 Handling of breakdowns

The asymmetric hybrid MMC is capable of blocking the currents from the AC side in case of short-circuit at the DC-side of the converter thanks to the FB submodules in the lower arm.

The first solution proposed in 4.3 to limit the overvoltage on the arm inductors in case of breakdown, which consists in bypassing the HB submodules instead of turning off all the IGBTs, is not applicable to the asymmetric hybrid MMC, as the bypass of the entire three upper arms would not allow to nullify the AC and DC currents.

The second solution consists in, instead of a single arm inductor, using small inductors with the purpose of splitting the overvoltage over the inductor in N parts within the rated insulation voltage of the submodules. Such solution, if proved to be feasible, could help in reducing the volume occupied by the converter.

5.4 Considerations on the hybrid asymmetric MMC

This topology reduces the number of FB to half of the total number of submodules, the remaining are HB. With the asymmetric scheme, the MMC is able to produce a DC voltage that ranges from zero to the nominal value $V_{\mathrm{d,nom}}$, which would be attractive for the operation of the NBI. To fully assess its capabilities would be necessary further study and the realisation of a model to be used for computer simulations.

In this thesis, it has been chosen to investigate in more detail the hybrid symmetric topology for two main reasons: the number of FB submodules employed are one third of the total instead of one half and it offers the possibility to partially decrease the overvoltage on the arm inductors during the second phase of the breakdown. The symmetric topology is able to nullify the arm currents by switching off the FB and bypassing the HB submodules, while the asymmetric topology, as discussed in the previous section, cannot adopt this strategy to block the arm currents.

Chapter 6

Preliminary design of the MMC

In this chapter will be estimated the parameters of the main components that would constitute the MMC-based AGPS for DTT NBI based on the hybrid topology in order to comply with the requirements in table 1.5. In section 6.1 will be determined the main parameters regarding the output voltage and current of the step-up transformers on the AC side of the converter. In section 6.2 will be calculated the number of submodules employed and the characteristics of its components. In section 6.3 will be calculated the inductance of the arm inductors. Section 6.4 will give a first estimate of the capacitance and resistance of the DC-filter placed at the DC side of the converter. All of the results obtained in this chapter will be opportunely verified in the next chapter with simulations whether they allow achieving the expected performances of the converter.

6.1 Step-up transformers

In order to size the transformers that elevate the voltage from the MV grid, the first step is to choose the voltage on the AC side of the converter. In order to keep the energy in the capacitors balanced the modulation index has to stay below 2, but since with $m = 2$ the balance is still not guaranteed, the maximum value has been chosen as $m_{\max} = 1.5$. With such modulation index, which is used for the minimal DC voltage, $V_{\mathrm{d,min}}$, the peak value of the AC voltage becomes:

$$\hat{v}_{\mathrm{s}} = m_{\max} \frac{V_{\mathrm{d,min}}}{2} = 1.5 \, \frac{167 \cdot 0.2}{2} = 25.05\,\mathrm{kV} \approx 25\,\mathrm{kV}. \tag{6.1}$$

The minimum modulation index, used at the nominal voltage, would then result:

$$m_{\min} = \frac{2 \cdot \hat{v}_{\mathrm{s}}}{V_{\mathrm{d,nom}}} = \frac{2 \cdot 25}{167} = 0.299 \approx 0.3. \tag{6.2}$$

Using equation 2.10 it is possible to compute the expected AC currents at nominal conditions as follows:

$$\hat{i}_{\mathrm{s,nom}} = \frac{2\, V_{\mathrm{d,nom}}\, I_{\mathrm{d,nom}}}{3\, \hat{v}_{\mathrm{s}}\, \cos(\varphi)} = \frac{2 \cdot 167 \cdot 70}{3 \cdot 25 \cdot 1} = 311.73\,\mathrm{A} \approx 312\,\mathrm{A}. \tag{6.3}$$

The maximum of the AC currents will be obtained at nominal conditions, for lower DC voltages the currents are expected to be lower.

From equation 2.16a is it possible to derive an expression for the voltage sources at the AC side, as follows:

$$v_{\phi} = v_{\mathrm{s}} - \frac{L}{2} \frac{\mathrm{d}i_{\mathrm{s}}}{\mathrm{d}t} - \frac{R}{2} i_{\mathrm{s}}. \tag{6.4}$$

The MMC is expected to work with unit power factor, meaning that v_{s} and i_{s} are in phase and the derivative term in equation 6.4 contributes basically with a phase shift. Also, the current i_{s} has a much smaller magnitude than the voltage v_{s}, so in the following will be assumed that, for this application, the

difference between $\hat{v}_\phi$ and $\hat{v}_s$ can be neglected, which will be verified in the next chapter with the results of the simulations.

With this preliminary considerations, the three step-up transformers would need to produce an AC voltage at their secondary of $\hat{v}_s = 25\,\text{kV}$ or about $v_{s,rms} = 18\,\text{kV}$, with a maximum current flowing in nominal conditions of $\hat{i}_{s,max} = 312\,\text{A}$ or about $i_{s,max,rms} = 221\,\text{A}$.

6.2 Design of the submodules

6.2.1 Current rating

The rated current of power semiconductors is the current that flows in nominal conditions, in case of MMC it is a combination of the DC, AC and circulating currents, respectively $I_{d,nom}$, $\hat{i}_{s,nom}$ and i_c . The flowing current in the submodules in nominal conditions can be computed as:

$$I_{SM,nom} = \frac{I_{d,nom}}{3} + \frac{\hat{i}_{s,nom}}{2} + i_c = \frac{70}{3} + \frac{312}{2} + \frac{70}{3} = 202.66\,\text{A} \approx 203\,\text{A}, \tag{6.5}$$

which has been confirmed by the simulations performed in nominal conditions. It has been selected a commercial IGBT module, manufactured by ABB, to be used as reference for choosing the main parameters of the submodules. The IGBT chosen, a LinPak phase leg IGBT module with part number 5SNG 0450X330300, is rated for a collector-emitter voltage V_{CES} of 3.3 kV and a continuous DC collector current I_C of 450 A. The complete datasheet can be found in [31]. It can sustain a peak forward current I_{FRM} of 900 A for up to 1 ms. This module is composed by the series of two IGBTs with an antiparallel diode each, so HB submodules will need one IGBT module and FB submodules will require two.

6.2.2 Number of submodules

In order to determine the number of submodules per arm is necessary to evaluate the average sum capacitor voltage per arm $v^{\Sigma}_{cap,u}$ and $v^{\Sigma}_{cap,l}$ and the average submodule capacitor voltage $V_{cap,nom}$.

The former can be determined with equation 2.24, with an additional 15% of margin results:

$$v^{\Sigma}_{cap,u} = v^{\Sigma}_{cap,l} = V_{cap,tot} = 1.15 \cdot \left(\frac{V_{d,nom}}{2} + \hat{v}_s\right) = 124.78\,\text{kV} \approx 125\,\text{kV}. \tag{6.6}$$

The latter value is chosen based on the IGBT module collector-emitter voltage V_{CES}, which has to be reduced by a safety factor of 2 as follows:

$$V_{cap,nom} = \frac{V_{CES}}{2} = 1.65\,\text{kV} \approx 1.5\,\text{kV}. \tag{6.7}$$

The safety factor takes into account mainly the Failure In Time (FIT) rate of the IGBTs and the voltage ripple on the capacitors [15]. The resulting number of submodules per arm N can now be calculated as follows:

$$N = \frac{v^{\Sigma}_{cap,u}}{V_{cap,nom}} = \frac{v^{\Sigma}_{cap,l}}{V_{cap,nom}} = \frac{125\,\text{kV}}{1.5\,\text{kV}} = 83.33 \approx 84. \tag{6.8}$$

Of the N submodules per arm, one third are FB, the remaining are HB submodules, so as follows:

$$F = \frac{N}{3} = 28 \tag{6.9a}$$

$$N - F = 56. \tag{6.9b}$$

The total number of submodules would be, for a three-phase converter with two arms per phase:

$$N_{tot} = N \cdot 2 \cdot 3 = 504. \tag{6.10}$$

The next step is to calculate how many submodules with DC-fault blocking capability are required in order for the converter to be able to successfully block the currents in case of a breakdown. The

minimum number required of submodules with DC-fault blocking capability per arm N_f, can calculated using equation 2.39, as follows:

$$N_f \geq \frac{\hat{v}_{ll}}{2 \cdot V_{cap,nom}} = \frac{\sqrt{3} \cdot 25\,kV}{2 \cdot 1.5\,kV} = 14.43 \approx 15. \tag{6.11}$$

Since the minimum number of submodules with DC-fault blocking capability N_f is lower than the number of FB submodules employed F, the converter should be already able to handle the breakdowns with the number of FB submodules already foreseen. This number could be increased in order to reduce the fault duration time, as an higher reverse voltage resulting from the increased number of capacitor in series can reduce the time needed for the fault current to get to zero. In the simulations will be verified if the chosen F can allow a blocking of the arm currents fast enough to limit the energy discharged in the accelerating grid, compatible with the requirements in table 1.5.

6.2.3 Submodule capacitance

The submodule capacitance is an important factor to determine, as a high value of capacitance has a significant impact on the total cost of the converter and a low one causes unacceptable voltage ripples. The energy that each arm has to provide every period can be calculated as [32];

$$\Delta E_{arm} = \frac{2 \cdot P_{d,nom}}{3 \cdot m\,\omega \cos(\varphi)} \left(1 - \left(\frac{m\,\cos(\varphi)}{2}\right)^2\right)^{\frac{3}{2}}, \tag{6.12}$$

and by dividing such energy for the number of submodules per arm N results the energy provided by each submodule ΔE_{SM}. To have an initial estimate of the submodule capacitance, C_{SM}, it has been used the following equation [33]:

$$\begin{aligned} C_{SM} = \frac{\Delta E_{SM}}{2 \cdot V_{cap,nom}^2\,\delta_{cap,pp}} = \frac{P_{d,nom}}{3 \cdot N\,m\,V_{cap,nom}^2\,\delta_{cap,pp}\,\omega \cos(\varphi)} \left(1 - \left(\frac{m\,\cos(\varphi)}{2}\right)^2\right)^{\frac{3}{2}} = \\ = \frac{11.69\,MW}{3 \cdot 84 \cdot 0.3 \cdot (1.5\,kV)^2 \cdot 0.1 \cdot 314 \cdot 1} \left(1 - \left(\frac{0.3 \cdot 1}{2}\right)^2\right)^{\frac{3}{2}} = 2.12\,mF \approx 2.5\,mF, \end{aligned} \tag{6.13}$$

where $\delta_{cap,pp}$ is the peak to peak voltage ripple on the capacitors normalised in respect to their nominal voltage. It has been chosen $\delta_{cap,pp} = 0.1$ to limit the ripple to an acceptable level. The simulations proved that the value calculated in equation 6.13 could guarantee the $\delta_{cap,pp}$ desired at the nominal voltage, when the voltage fluctuation on the capacitors are largest.

6.2.4 Switching frequency

It has been assumed an equivalent switching frequency of the converter equal to 10 kHz; an high frequency can reduce the ripple on the DC side with the consequence of requiring a smaller filter, which would in turn reduce the energy discharged on the accelerating grids in case of breakdown. An excessive switching frequency may result in excessive losses on the power components to an extent where submodules may need an active cooling system to dissipate the heat, which should be avoided for this application. The switching frequency of the single submodule will result:

$$f_{SM} = \frac{f_{eq}}{2 \cdot N} = \frac{10\,kHz}{2 \cdot 84} = 59.52\,Hz \approx 60\,Hz. \tag{6.14}$$

In the simulation it has been verified that increasing the equivalent switching frequency does not provide significant improvement on the performances.

6.3 Arm inductance

The arm inductors have two main roles: to limit the high-frequency components in the circulating currents and to limit the overcurrents caused by the breakdowns on the DC side, protecting the components of the submodules.

The current in case of a short circuit at the DC side must be kept under the peak collector current I_{CM}, which is the largest current that the IGBT is able to interrupt. It has to be taken into account that the detection of the fault and the subsequent IGBT switch-off are not instantaneous, but assuming a detection time of 5 µs and considering from the IGBT module datasheet, in the worst case, a turn-off delay time $t_{d,off}$ of 1.05 µs and a fall time t_f of 0.375 µs, the total delay time results about $t_d = 6.45\,\mu s$. In order to limit the rising fault current from the nominal peak value in the submodule $I_{SM,nom}$ to I_{CM} in the time t_d, the arm inductance can be calculated as:

$$L_{arm} = \frac{V_{L,max,1}\, t_d}{I_{CM} - I_{SM,nom}} = \frac{\left(V_{d,nom} + \hat{v}_{ll}\right)\, t_d}{2 \cdot \left(I_{CM} - I_{SM,nom}\right)} = \frac{\left(167\,kV + \sqrt{3} \cdot 25\,kV\right)\, 6.45\,\mu s}{2 \cdot (900 - 203)\,A} = 0.97\,mH \approx 1\,mH. \tag{6.15}$$

The dimensioning of the arm inductance can have two approaches: limiting the arm currents in case of short circuit on the DC side of the MMC and limiting the high-frequency components of the circulating currents. Typically, the former produces a larger value than for the latter, but since the chosen IGBT module has a large current rating in respect to the currents involved, the resulting inductance to limit the current is relatively low.

The circulating currents have a switching frequency component which can propagate also to the DC side of the converter. The arm inductor, when opportunely sized, can limit the peak to peak value of the high-frequency component of the circulating currents to an acceptable level. The voltage that drives the circulating current can be expressed, with unit power factor, as [34]:

$$v_c = \frac{N}{8 \cdot C_{SM}} \left(-\frac{3}{4\,\omega} m\, \hat{i}_s \sin(2\,\omega\, t) + \frac{1}{3\,\omega} m^2\, I_d \sin(2\,\omega\, t) \right). \tag{6.16}$$

Since this voltage results applied to the arm inductors for a time Δt, the peak to peak value of the circulating current can be calculated as follows:

$$i_{c,pp} = \frac{v_c}{L_{arm}} \Delta t. \tag{6.17}$$

The arm inductance has to be sized for limiting $i_{c,pp}$ to an acceptable value in the worst condition, which is for the maximum value of v_c and Δt. The maximum value assumed by v_c can be computed from equation 6.16, as follows:

$$\begin{aligned} v_{c,max} &= \frac{N}{8 \cdot C_{SM}} \left(-\frac{3}{4\,\omega} m\, \hat{i}_{s,nom} + \frac{1}{3\,\omega} m^2\, I_{d,nom} \right) = \\ &= \frac{84}{8 \cdot 2.5\,mF} \left(\frac{3}{4 \cdot 314} 0.3 \cdot 312\,A - \frac{1}{3 \cdot 314} 0.3^2\, 70\,A \right) = 910.89\,V. \end{aligned} \tag{6.18}$$

The maximum value of Δt is the switching period T_s, which is the reciprocal of f_{eq}. Therefore, the arm inductance can be estimated with:

$$L_{arm} = \frac{v_{c,max}\, T_s}{i_{c,pp,max}} = \frac{910.89\,V}{7\,A \cdot 10\,kHz} = 13.01\,mH \approx\ 15\,mH, \tag{6.19}$$

where it has been assumed to limit $i_{c,pp,max}$ to the 10% of $I_{d,nom}$.

6.4 DC-filter

The capacitance and resistance of the DC-filter, which is placed on the DC side of the converter, have to be sized carefully in order to avoid damaging the accelerating grids in case of breakdown.

The capacitor of the DC-filter has two main purposes: to eliminate part of the DC voltage ripple and to limit the overvoltage in case of beam-off. The high frequency components of the three circulating currents have no other path than to flow in the DC-filter, causing voltage ripples on the DC side of the converter. Its capacitance will be initially estimated by limiting those voltage ripples. The maximum peak to peak component of the switching frequency circulating current is expected to be at maximum:

$$i_{c,pp,max} = \frac{v_{c,max}}{L_{arm}} T_s = 6.07\,A. \tag{6.20}$$

To limit the peak to peak voltage ripple on the DC side within the 10% of the nominal value, for such value of $i_{c,pp,max}$, the capacitance of the filter has to be at least:

$$C_{filter} = \frac{3 \cdot i_{c,pp,max}\, T_s}{\Delta V_{d,max}} = \frac{3 \cdot 6.07\,\text{A}}{16.7\,\text{kV} \cdot 10\,\text{kHz}} = 107.78\,\text{nF} \approx 108\,\text{nF}. \tag{6.21}$$

The energy discharged onto the grids by the filter capacitor alone can be evaluated as follows:

$$Q_{filter} = C_{filter}(V_{d,nom} - V_{arc}) = 108\,\text{nF} \cdot (167000 - 100\,\text{V}) = 18\,\text{mC}, \tag{6.22}$$

which is below the maximum allowed in table 1.5, but it does not take into account the contribution of the AGPS. In the following chapter will be tested with simulations if the chosen value of capacitance, in combination with the charge transferred by the AGPS, does not cause an excessive discharge of energy onto the accelerating grids in case of breakdown.

The role of the resistor of the DC-filter is to limit the overcurrent from the DC-filter to the accelerating grids in case of a breakdown. Considering as the maximum admissible peak current on the grids in case of breakdown $I_{grids,max} = 3\,\text{kA}$, the resistor can be sized as follows:

$$R_{filter} = \frac{V_{d,nom}}{I_{grids,max}} = \frac{167\,\text{kV}}{3\,\text{kA}} = 56\,\Omega. \tag{6.23}$$

Chapter 7

Simulations

To verify the suitability of this topology as the AGPS for DTT NBI, it has been developed a computer simulation based on Simulink software [35]. Some screenshots of the model that has been developed are reported in appendix A. Instead of simulating all the submodules of the converter, it has been chosen to include in the model just a limited number of submodules per arm to reduce the computational cost. For the hybrid MMC it has been used 4 HB submodules and 2 FB submodules per arm, so the ratio $\frac{F}{N} = \frac{1}{3}$ is respected also in the model. The voltage has been scaled down proportionally to the number of submodules employed, while the current has been kept the same as the full-scale converter. The scaling factor K_{scale} can be defined as the ratio between N of the full converter and of the scaled version, as follows:

$$K_{\text{scale}} = \frac{N^*}{N} = \frac{6}{84} \approx 0.0714. \tag{7.1}$$

In the following, the quantities with an asterisk as superscript will refer to the scaled model.

The schematic of the model of the hybrid converter is depicted in figure 7.1; in grey are indicated some of the quantities measured, such as currents and the capacitor voltages, and the IGBTs gate signals. The measured quantities are sent to the control systems, which is not shown in the figure.

The three phase AC source has been modelled as three ideal AC voltage sources followed by an inductor each. The voltage sources produce a peak AC voltage that has been scaled down from the value of full size converter, as follows:

$$\hat{v}^*_\phi = \hat{v}_\phi \, K_{\text{scale}} \approx 1.8\,\text{kV} \qquad \text{for } \phi = \text{a, b, c.} \tag{7.2}$$

The load, which is the NBI accelerator, has been modelled as an ideal voltage-controlled current source, whose dependence on the accelerating voltage is defined by the function in equation 1.19a. The measured voltage is filtered to remove part of the voltage ripple.

In parallel to the load is present a DC-filter, which is composed by the resistance R_{filter} and the capacitance C_{filter}. These values have been scaled down from the full size converter, as follows:

$$R^*_{\text{filter}} = R_{\text{filter}} \, K_{\text{scale}} = 4\,\Omega \tag{7.3a}$$

$$C^*_{\text{filter}} = \frac{C_{\text{filter}}}{K_{\text{scale}}} = 1.5\,\mu\text{F}. \tag{7.3b}$$

The condition of breakdown has been simulated by adding an ideal switch in parallel to the load, which is switched on to simulate a short-circuit on the DC side of the converter. In series to the switch is present a DC voltage source of 100 V that represent the arc voltage of the breakdown [15].

The operating frequency of the submodules of the scaled model has to be set in order to keep an equivalent switching frequency $f_{\text{eq}} = 10\,\text{kHz}$, so the voltage ripple and the control dynamics will result

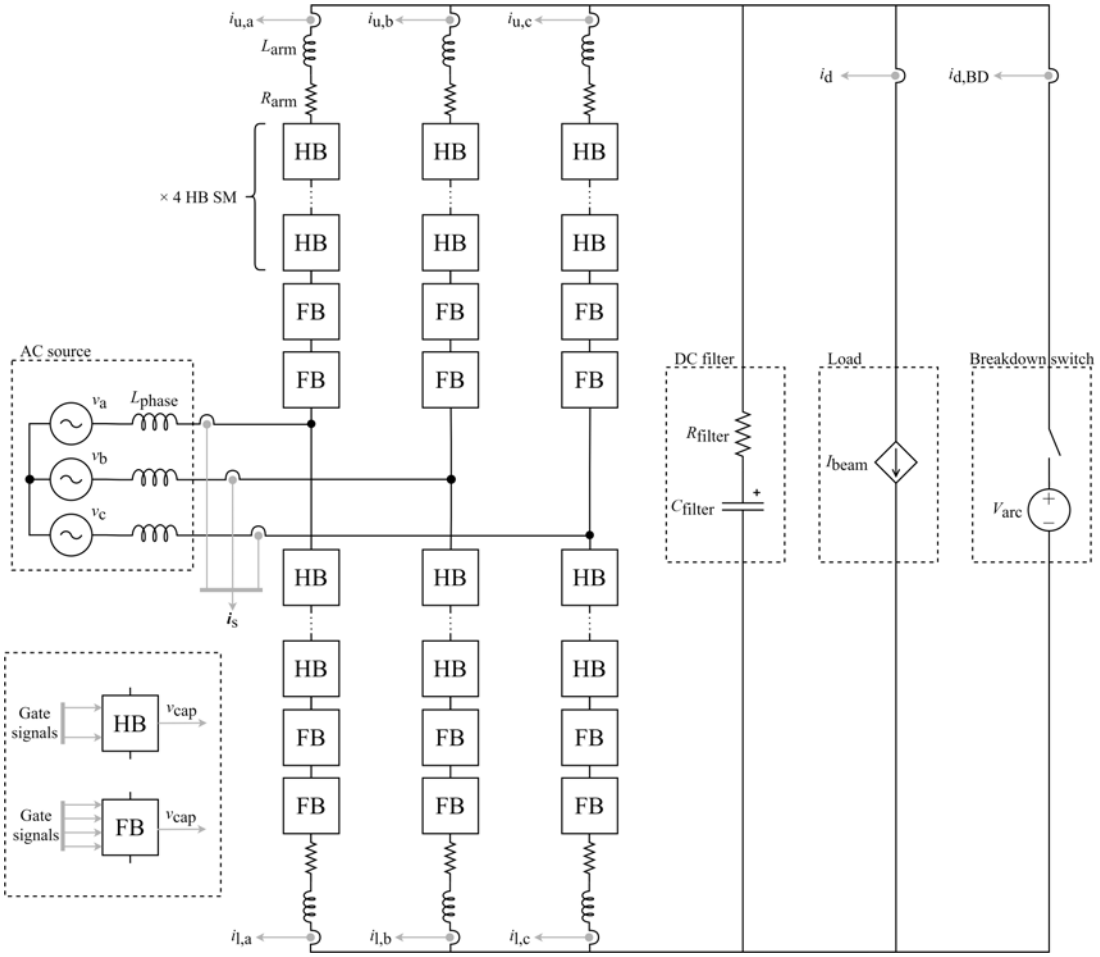

Figure 7.1: Scheme of the model used to simulate the hybrid MMC.

directly comparable with the full-scale MMC. The frequency for the scaled converter has been calculated analogously as in equation 6.14, as follows:

$$f_{SM}^{*} = \frac{f_{eq}}{2 \cdot N^{*}} \approx 833\,\text{Hz}. \tag{7.4}$$

The remaining parameters used for the simulated model are reported in table 7.1, where they can be compared with the corresponding values of the full-scale MMC.

The control scheme used is the one that has been described in section 4.2.

In the following sections will be examined the performances of the model of the hybrid MMC to verify the fulfilment of the requisites in table 1.5. Specifically, in section 7.1 will be analysed the performance at steady state at different voltage levels, in 7.2 the performance during the transients and in 7.3 the performance in case of breakdown.

7.1 Operation at steady state

For the operation at steady state will be presented the results for three different working conditions: 100%, 30% and 20% of $V_{d,nom}$, respectively the nominal DC voltage, the DC voltage with modulation index $m = 1$ and the minimum DC voltage. The DC current changed accordingly to the perveance as in equation 1.19a.

Table 7.1: Parameters of the full-scale hybrid MMC and of the scaled model.

	Full-scale MMC	Model MMC
$V_{\text{d,nom}}$ [kV]	167	12
$I_{\text{d,nom}}$ [A]	70	70
$P_{\text{d,nom}}$ [MW]	11.69	0.84
$\hat{v}_{\text{s}}$ [kV]	25	1.8
N	56	6
F	19	2
$V_{\text{cap,nom}}$ [kV]	1.5	1.5
C_{SM} [mH]	2.5	2.5
f_{SM} [Hz]	60	833
L_{arm} [mH]	15	15
R_{filter} [Ω]	56	4
C_{filter} [μF]	0.108	1.5

7.1.1 Operation at 100% $V_{\text{d,nom}}$

In figure 7.2 are presented the results from the simulation of the MMC operating at 100% of $V_{\text{d,nom}}$, to which corresponds the nominal current of 70 A. The converter is operating with a modulation index equal to 0.3. The accuracy is much lower than the required 2%. The maximum ripple allowed on the voltage is ±5% of V_{d}, so in this case the maximum oscillation allowed would be ±600 V and the resulting ripple is much lower than that, about ±50 V to the set voltage. The currents on the AC side present a Total Harmonic Distortion (THD) of about 1%. As can be seen in figure 7.2d, the average reactive power supplied from the AC source is zero. The capacitors, as can be seen in figure 7.2f, have a voltage fluctuation of about 250 V peak to peak around an average voltage of 1660 V. The capacitors, since it has not been implemented a control scheme apt to control the average voltage of the capacitors, have reached an average voltage above the nominal value. The capacitors are perfectly balanced with each other. In the DC voltage and in the DC current is present an important ripple component at 300 Hz, as it can be seen in figures 7.2g and 7.2h, where is presented a close-up view of the waveforms. In the latter figure the current flowing in the load is noted with I_{d}, while the current upstream the DC-filter is noted with $I_{\text{d,AGPS}}$. It has been hypothesised that such component could be attenuated by properly filtering it in the circulating currents control, and it will be verified in the future work. Removing this component of the ripple could reduce significantly the overall ripple, allowing to reduce the size of the arm inductors and of the DC-filter capacitance.

7.1.2 Operation at 30% $V_{\text{d,nom}}$

In figure 7.3 are presented the results from the simulation of the MMC operating at 30% of $V_{\text{d,nom}}$, 3600 V, which corresponds to a DC current of 11.5 A and a modulation index equal to 1. Also in this case the accuracy is much lower than the required ±2%, but the voltage ripple is worse than in figure 7.2a. Most of it is due to the ripple component at 300 Hz. It is still well within the allowed range, which, for the set voltage of 3600 V, is ±180 V. It figure 7.3b it can be noted a higher ripple on the AC currents, the THD is now about 4%. With a lower DC current is harder to achieve a perfect balancing of the capacitors, but nevertheless in figure 7.3d the capacitors fluctuate around values with a negligible difference. The balancing proved to be stable.

7.1.3 Operation at 20% $V_{\text{d,nom}}$

In figure 7.4 are presented the results from the simulation of the MMC operating at 20% of $V_{\text{d,nom}}$, 2400 V, which corresponds to a modulation index equal to 1.5. The accuracy of the DC voltage is always below the requested ±2%. Even in this case the ripple is within the limit, which in this case is ±120 V from the set voltage, but most of it is still due to the ripple component at 300 Hz. The currents on the AC side present a THD of about 10%. As can be seen in figure 7.4b and 7.4c, the AC and arm currents start to manifest the presence of higher harmonics. In figure 7.4d are plotted the average voltages of all

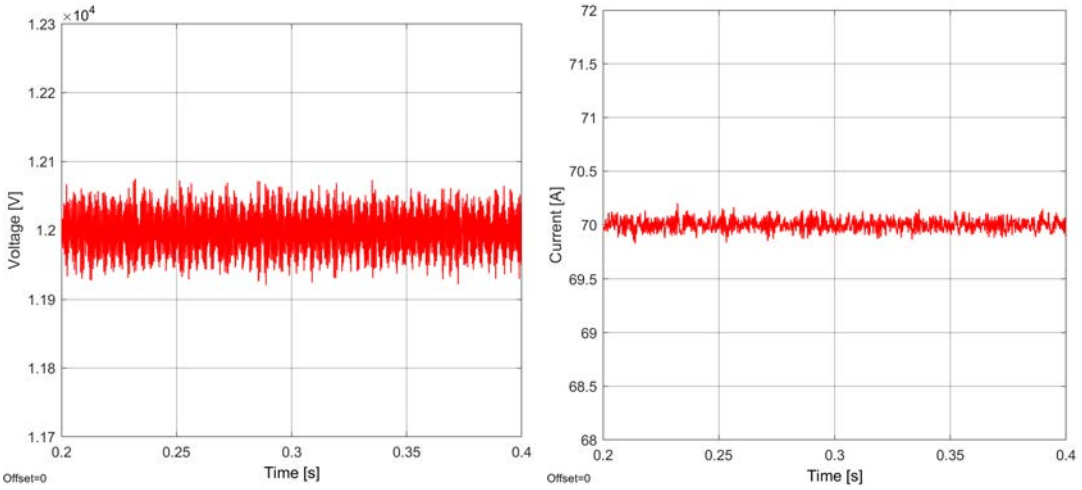

(a) Voltage on the DC side V_d.

(b) Current on the DC side I_d.

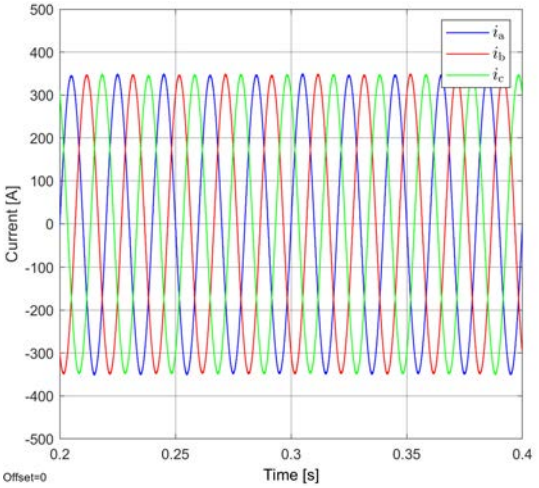

(c) Currents on the AC side $\boldsymbol{i}_\mathrm{s}$.

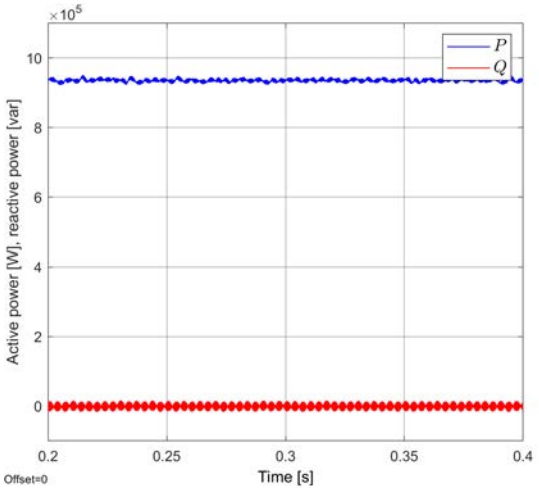

(d) Active and reactive power supplied by the AC source.

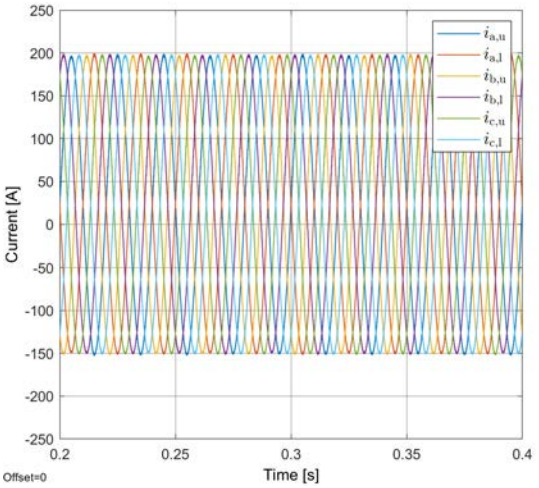

(e) Arm currents.

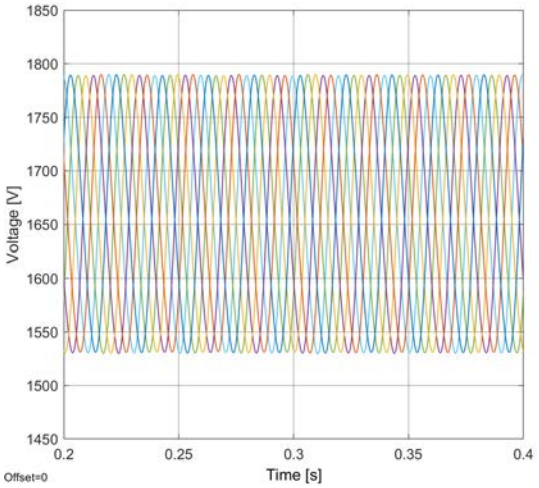

(f) Voltages of the submodule capacitors.

Figure 7.2: Operation at 100% of $V_{\mathrm{d,nom}}$, I_d of 70 A and $m = 0.3$.

FB and HB submodules. The imbalance between the two kinds of submodules, which is about 0.5 V, is negligible and they can be considered balanced.

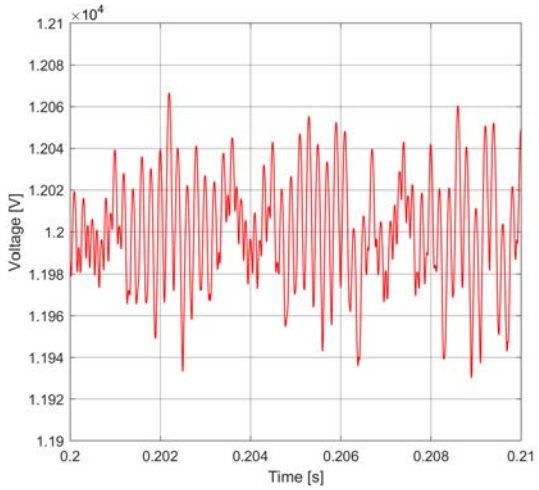

(g) Voltage on the DC side V_{d}.

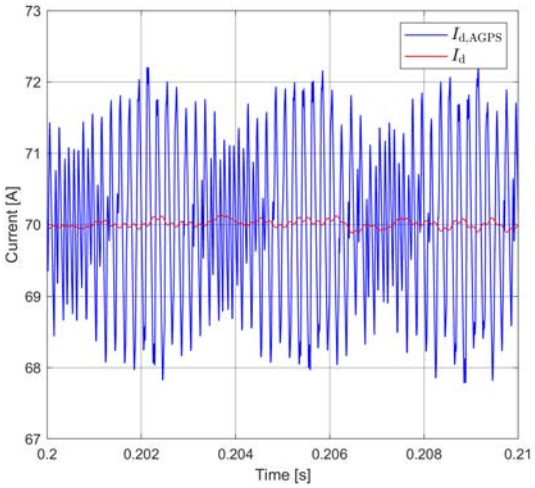

(h) Current on the DC side.

Figure 7.2: Operation at 100% of $V_{\mathrm{d,nom}}$, I_{d} of 70 A and $m = 0.3$.

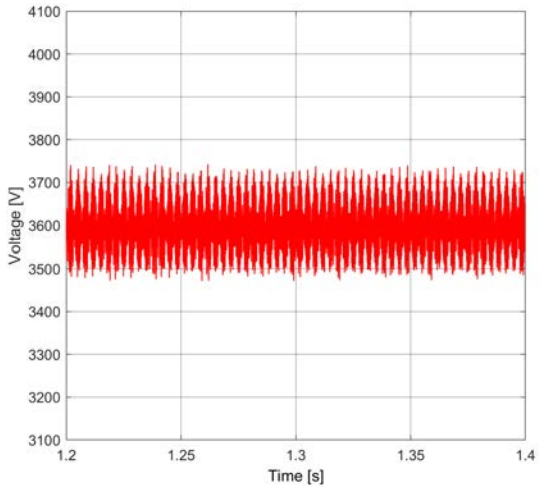

(a) Voltage on the DC side V_{d}.

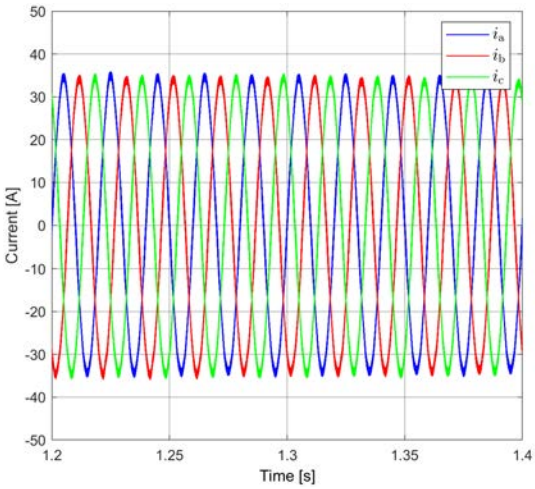

(b) Currents on the AC side $\boldsymbol{i}_{\mathrm{s}}$.

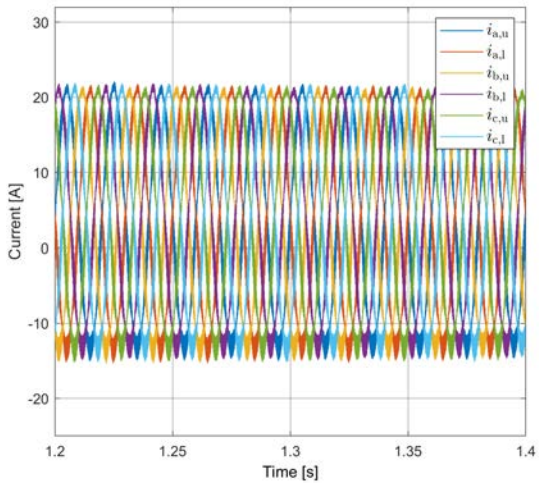

(c) Arm currents.

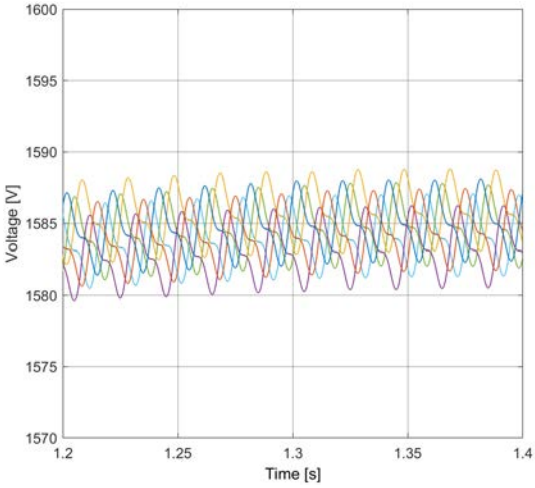

(d) Voltages of the submodule capacitors.

Figure 7.3: Operation at 30% of $V_{\mathrm{d,nom}}$, I_{d} of 11.5 A and $m = 1$.

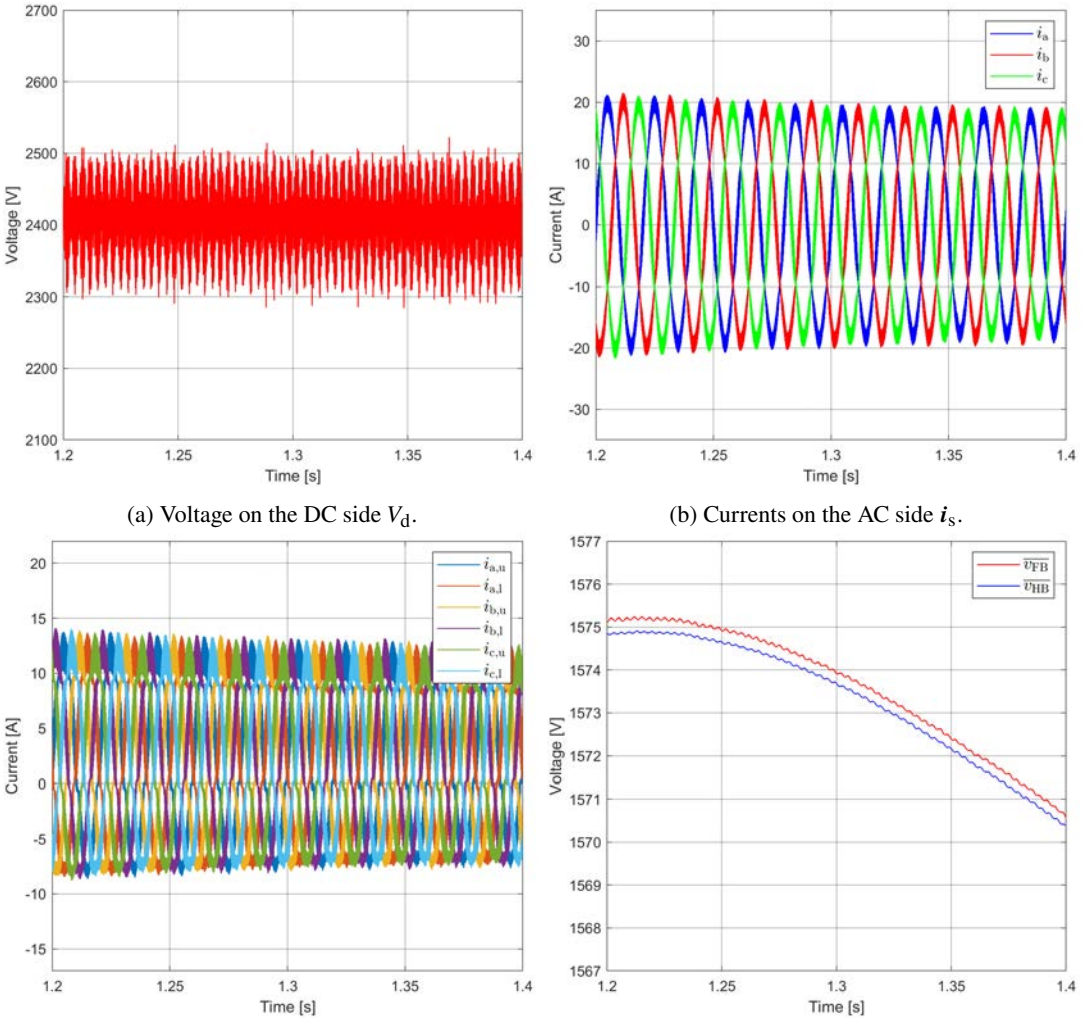

(a) Voltage on the DC side V_{d}.

(b) Currents on the AC side $\boldsymbol{i}_{\mathrm{s}}$.

(c) Arm currents.

(d) Average voltages of all FB and HB submodule capacitors.

Figure 7.4: Operation at 20% of $V_{\mathrm{d,nom}}$, I_{d} of 6.3 A and $m = 1.5$.

7.1.4 Comparison between v_{s} and v_{ϕ}

In section 6.1 it has been assumed that the difference between $\hat{v}_{\mathrm{s}}$ and $\hat{v}_{\phi}$ may be neglected. In figure 7.5 are presented the plots of v_{s} and v_{ϕ} of a single phase at the three operating points discussed above. v_{s} has been filtered to eliminate switching component due to the insertion of the submodules to display more clearly its value. As can be seen, at the nominal voltage the difference between the peak values of the two is not so negligible, as it corresponds to about 200 V, while for lower voltages the assumption seems valid. It has to be considered that in the model it has been scaled down the voltage, but not the current, so it is normal that the terms related to the current in 6.4 have a larger influence. The difference in the full-size converter would result much lower, since the terms related to the current should remain at the same magnitude.

7.2 Study of the dynamic performances

The dynamic performances of the model of the converter have been assessed for two possible scenarios: the perveance matching start-up and start-up at maximum voltage, as described in section 1.4.3. Both situations have been simulated at the nominal conditions of DC voltage and current.

The perveance matching start-up scenario is depicted in figure 7.6. As can be seen in figure 7.6a the rise

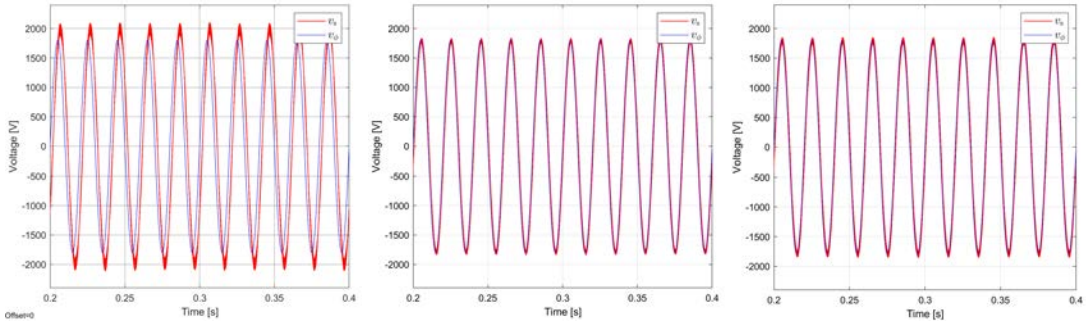

(a) 100% of $V_{\mathrm{d,nom}}$, I_{d} of 70 A. (b) 30% of $V_{\mathrm{d,nom}}$, I_{d} of 11.5 A. (c) 20% of $V_{\mathrm{d,nom}}$, I_{d} of 6.3 A.

Figure 7.5: Comparison between v_{s} and v_{ϕ}.

time of the voltage can be accomplished in much faster times than the maximum required in table 1.5, which is 80 ms.

The start-up at maximum voltage scenario is depicted in figure 7.7. The beam current is kept off until the DC voltage reaches its maximum value, then is ramped up in 20 ms to the value resulting from equation 1.19a. The voltage undershoot resulting from the sudden increase of the load is well below the maximum allowed of 15%. There is a slight overvoltage due to the fact that the control system regulate the DC voltage by varying the reference of the AC current and not directly the insertion indices of the submodules, thus during the transients the control system may be relatively slow to react to overshoots and undershoots. This would be avoided by bringing opportune changes to the control systems.

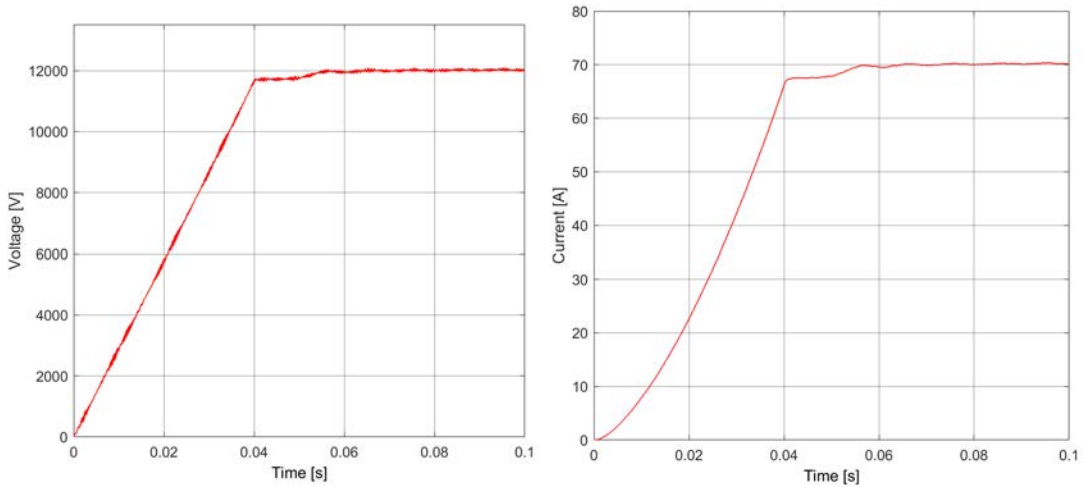

(a) Voltage on the DC side V_{d}. (b) Current on the DC side I_{d}.

Figure 7.6: Operation during the start-up in perveance matching of the converter.

7.3 Operation in case of breakdown

The breakdown has been simulated at $t = 0.1$ s, and the IGBT have been turned off after 6.45 µs, as determined in section 6.3. The simulations have been performed at the nominal voltage, which is the worst scenario both for the energy discharged onto the accelerating grids and for the overvoltage on the arm inductors. The IGBTs of the FB submodules have been turned off, while the HB submodules have been commanded into the bypass state.

In figures 7.8 are presented the results of a simulated breakdown and a following restart of the converter after 20 ms. At the restart of there are fluctuations on the DC voltage, those are caused by the imbalance

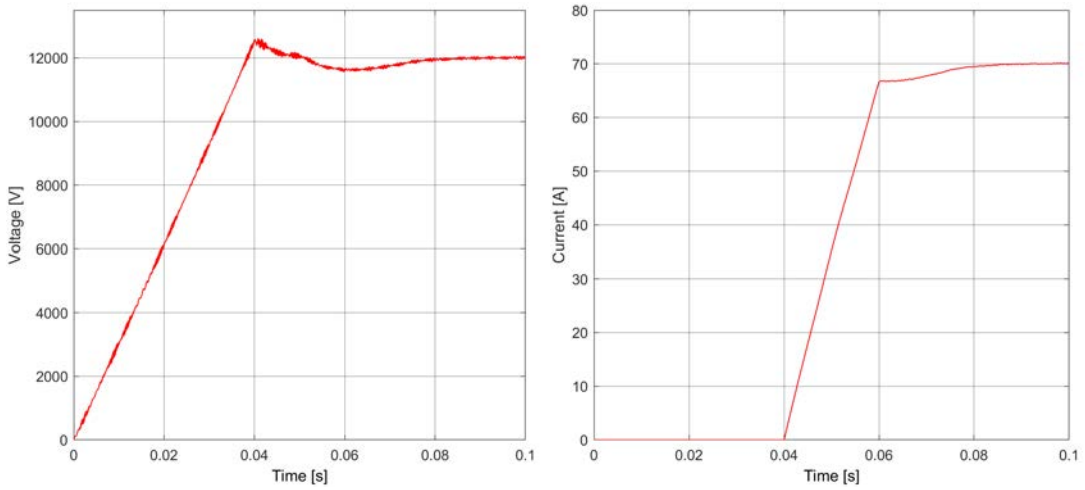

(a) Voltage on the DC side V_d.

(b) Current on the DC side I_d.

Figure 7.7: Operation during the start-up at the maximum voltage of the converter.

of the total capacitor voltage between different arms. In fact, immediately after the breakdown, the operation is stopped and the capacitors remain at approximately the voltage level they were in the instant the breakdown take place. As can be seen in figure 7.8b, the capacitors result with significant voltage differences between each other; this imbalance is adjusted over time by the control system once the converter restarts the operation. The resulting ripple on the DC voltage is still within the acceptable limits set in table 1.5. When operating with lower DC voltages the imbalance resulting after a breakdown will be lower, as the ripple on the capacitors is smaller. In the future work will be investigated methods to solve this issue, for example by restarting the control before the 20 ms to restore the balance between the capacitors and allow a more stable restart of the converter.

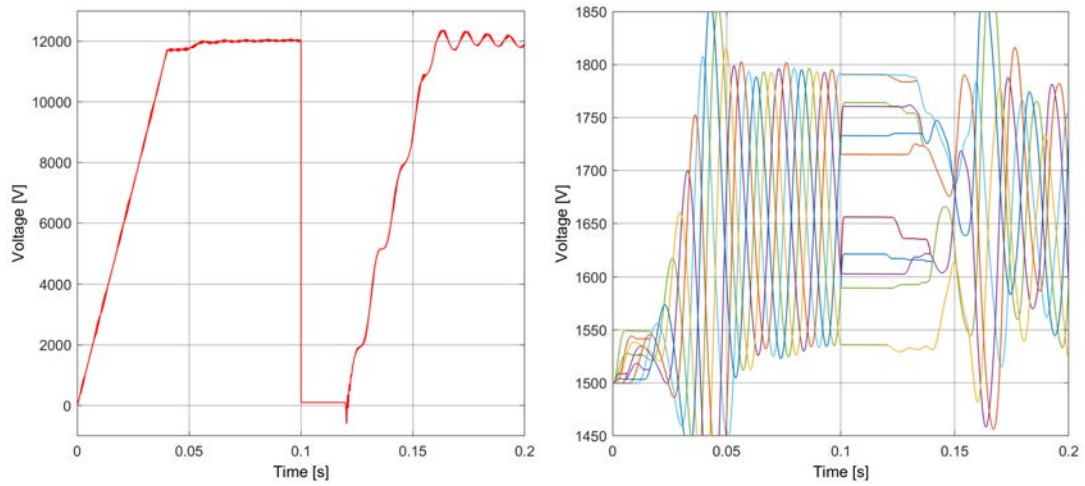

(a) Voltage on the DC side V_d.

(b) Voltages of the submodule capacitors.

Figure 7.8: Operation in case of breakdown and following restart of the converter.

The voltage on the arm inductor is plotted in figure 7.9a. From the picture it is possible to distinguish the two phases described in section 4.3. The first phase starts at $t = 0.1$ and it lasts for 6.45 µs. The second phase lasts until the arm currents are nullified. In this picture the voltage reached are below the maximum possible values that have been estimated in section 4.3.

As can be seen in figure 7.9d the arm currents increase slightly in the first phase of the breakdown, while the submodules are still in operation. Once the FB submodules switch off, the currents start to decrease

until they become zero.

In figure 7.9e is presented the charge transferred to the arc during the breakdown. The total charge, in figure noted as $\int i_{\text{tot}}\,\mathrm{d}t$, reaches about 74 mC, which is lower than the maximum allowed of 250 mC. In figure are also plotted the single contributions of the AGPS, noted with $\int i_{\text{AGPS}}\,\mathrm{d}t$ and of the DC-filter, noted as $\int i_{\text{filter}}\,\mathrm{d}t$. The contribution of the DC-filter is confirmed to be about 18 mC, while the contribution of the AGPS without considering the filter is about 56 mC, which could be lowered by reducing the inductance of the arm inductors.

In figure 7.9f are plotted the average voltages of all FB and HB submodules. The capacitors of the HB submodules, which are bypassed after the breakdown, remain unchanged, while the capacitors of the HB submodules are charged until the currents have been nullified.

The high peak current reached, which is mainly due to the discharge of the DC-filter, as can be seen in figure 7.9b, it does not go above 3 kA.

7.4 Considerations on the hybrid MMC

A large fraction of submodules employed in the converter are HB modules, which are more compact and require half of IGBTs and diodes than the FB. It would provide the possibility to reduce the overvoltage on the inductors in the second phase of the breakdown, once the IGBTs of the FB submodules are turned off, by bypassing the HB submodules, as discussed in 4.3.

The converter is not as flexible as a FB-based MMC, but it is still capable of producing a DC voltage in the range 20 to 100% of $V_{\text{d,nom}}$. To guarantee the operation in this voltage range was necessary to use a relatively low AC voltage, which causes larger fluctuation on the capacitor voltages. Since the converter proved to maintain a negligible imbalance between FB and HB submodules at a modulation index of 1.5, it would be possible to investigate its operation even for higher m and lower DC voltages.

The model of the hybrid MMC proved to be capable of achieving the performances required in table 1.5. The main issue encountered was a significant ripple with a frequency of 300 Hz: it has been hypothesised that it could be solved by properly tuning the circulating current control. If such component will be reduced, it would be possible to further reduce the arm inductors and the DC-filter capacitance; consequently, the energy discharged onto the accelerating grids would be decreased.

With the proper adjustments to the control scheme, the hybrid MMC seems to be a promising solution as the AGPS of the NBI of DTT.

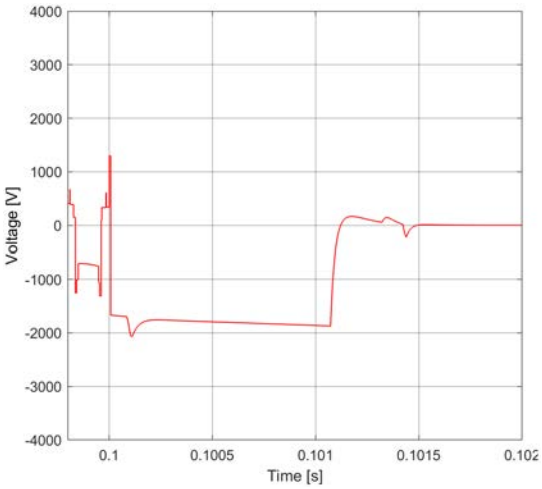

(a) Voltage on the arm inductor.

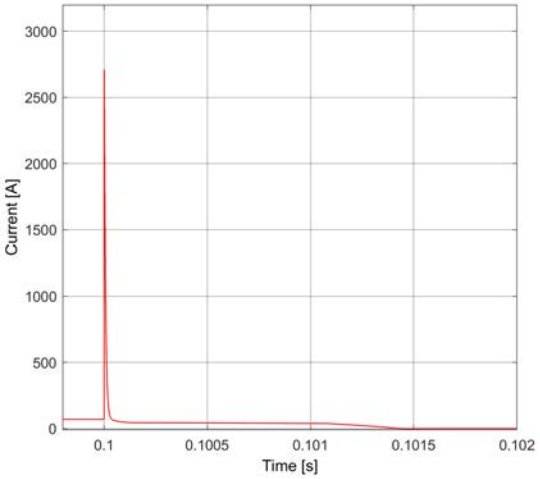

(b) Current on the DC side I_{d}.

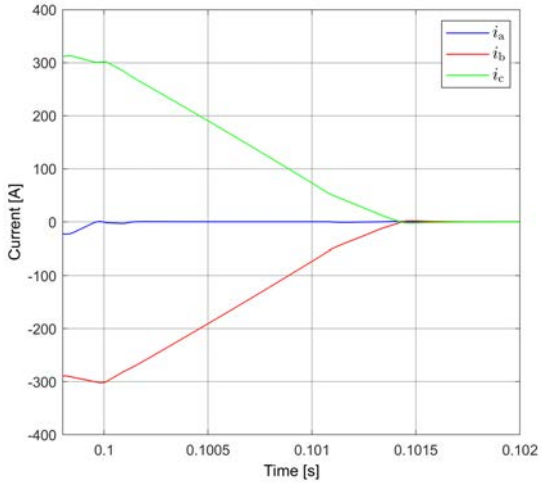

(c) Currents on the AC side $\boldsymbol{i}_{\mathrm{s}}$.

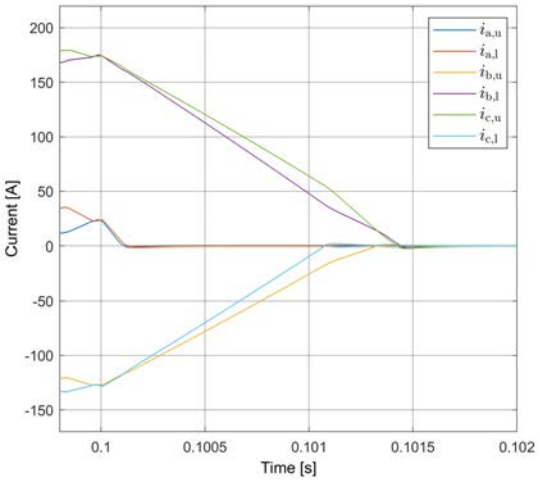

(d) Arm currents.

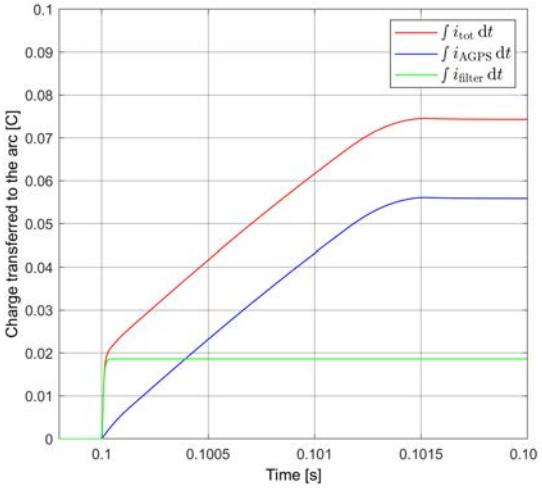

(e) Charge delivered to the grids.

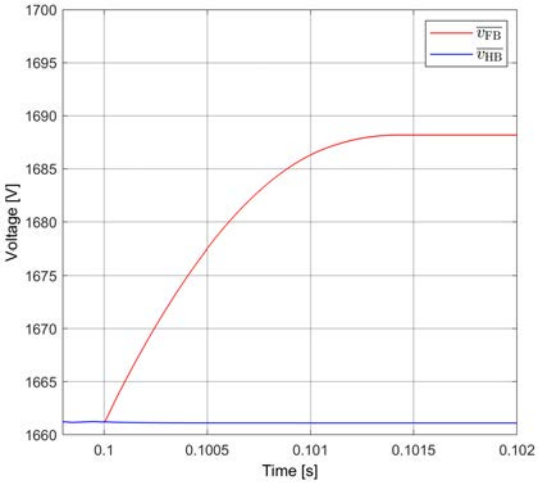

(f) Average voltages of all FB and HB submodule capacitors.

Figure 7.9: Operation in case of breakdown.

Chapter 8

Conclusions

8.1 Results obtained

In this thesis, studies on the preliminary design of the Acceleration Grid Power Supply (AGPS) of the DTT Neutral Beam Injector (NBI) based on the Modular Multilevel Converter (MMC) scheme have been carried out. This approach is another option with respect to the two-stage scheme adopted in MITICA and ITER NBIs, and in principle would present a set of advantages, as described in section 1.4.6. In alternative to the classical scheme with all Full-Bridge (FB) or Half-Bridge (HB) bidirectional submodules, already studies in a previous thesis for the NBI of the DEMO plant [15], three possible topologies have been investigated: the unidirectional MMC, the hybrid symmetric MMC and the hybrid asymmetric MMC. Their capability to satisfy all the preliminary requirements of the Acceleration Grid Power Supply of DTT NBI has been analysed, through analytical calculations and simulations. One of the most demanding constraints is the need to generate a stable DC output voltage in the range from 20 to 100% of the nominal voltage, with a voltage ripple within ±5% of the actual voltage reference. Another important requirement is the capability to withstand to frequent short-circuits at the output (due to arc breakdowns among the accelerating grids), limiting the current transferred to the arc and being capable to ramp-up again the voltage in 20 ms. These specifications are related to this specific application, and does not apply typically on the industrial HVDC power conversion systems. In addition, the installation in the existing buildings of DTT site pose severe limits on the available space.

The unidirectional MMC seemed appealing because it make use of very compact submodules with a small number of power components and it lacks the arm inductors, which take up a significant fraction of the whole converter volume. However, it has been proved that their operational range is too limited for the requisites of the AGPS. In particular, it is not possible to adjust the DC voltage below the total arm capacitor voltage: to ramp-up the DC voltage, the capacitors would have to be charged in a too small time frame.

In the hybrid symmetric MMC, of the total number of submodules, just a third are FB and the remaining are HB. This topology can operate with a maximum theoretical modulation index equal to 2, but to maintain the capacitors balanced should be somewhat lower, around 1.5. To produce a low DC voltage, the voltage on the AC side has to be set relatively low, in comparison with common applications; this causes increased currents at AC side and significant voltage fluctuations on the capacitors when operating around the nominal DC voltage and current. The hybrid symmetric MMC, in case of arc breakdown, can bypass the HB submodules instead of turning them off as the FB submodules, which would result in a reduced consequent overvoltage on the arm inductors in the second phase of the breakdown.

The hybrid asymmetric MMC foresees only HB submodules in the upper arms and only FB submodules in the lower arms. This topology would allow the converter to produce a voltage from zero to the nominal DC voltage, which would result useful for the operation of the NBI of DTT. However, bypassing the HB submodules instead of turning off all the IGBTs, is not applicable in this case, as it would bypass the entire three upper arms, and so the breakdown current would not be nullified.

In this thesis most of the study has been carried out on the hybrid symmetric topology, since it makes use of a lower number of FB submodules and it offers the possibility to limit the overvoltage on the arm inductors by bypassing the HB submodules.

It has been made a preliminary design of the converter that would be used as AGPS of the NBI of DTT. Based on the such design, it has been developed a scaled-down model of the converter to be used for assessing its performances with computer simulations.

The simulations proved that the model could produce the required voltage range; the voltage ripple is below the limit of ±5% for every set voltage. It resulted a significant ripple component at 300 Hz, which it has been attributed to an improvable tuning of the circulating currents control. The model proved to be able to reach the nominal DC voltage in a period much shorter than the maximum time required, for both the start-up in perveance matching condition and the start-up at full voltage. It has been simulated also the event of breakdown among accelerating grids: the model proved able to restart the operation 20 ms after the breakdown, with some oscillations due to the imbalance between the capacitor voltages resulting immediately after the interruption of the operation. The charge transferred to the accelerating grids resulted well below the maximum allowed, but there is still some margin for improvement to reduce the contribution due to the AGPS itself, optimizing the value of arm inductor and output DC-filter capacitor.

It can be concluded that the hybrid MMC proved to have performances which makes it suitable to be employed as the AGPS for the NBI of DTT.

8.2 Future work

In this final section will be presented the future work that is associated with the design of a MMC-based AGPS for the NBI of DTT.

The asymmetric converter could be further investigated, also with the development of a model to be used in simulations, since it could provide a wider operation range with respect to the symmetric topology.

In regards to the hybrid symmetric configuration, it is necessary to improve the control system to filtrate the ripple component at 300 Hz to guarantee better performances, especially at lower DC voltages. If the ripple will be attenuated, it would be possible to reduce the inductance of the arm inductor and the capacitance of the DC-filter, which would in turn lower the energy discharged onto the accelerating grids in case of breakdown. It has to be studied a method to handle the imbalance of the capacitors right after the breakdown, to allow a more stable restart of the converter. Also, the control system should be adjusted to react faster to overshoots and undershoot at the start-up of the converter.

It shall be conducted a thermal analysis on the switching and conduction losses of the power components, which in this thesis have not been considered, to verify if the natural convection would be enough as a heat-removal source, as proposed in [15].

It will have to be assessed the actual feasibility of dealing with the breakdowns by bypassing the HB submodules and switching off just the IGBTs of the FB submodules. Another solution that would help reducing the overall volume occupied by the converter would be using smaller inductors split among the submodules; such solution would need to be further investigated.

Finally, it will be necessary to estimate the volume occupied by the AGPS based on the MMC technology: it will be determined the size of the components involved, the distances that they require to guarantee the insulation and it will be outlined a possible layout of the converter that hopefully would fit inside the space allocated in the designated building at the DTT site.

Appendix A

Simulink model

In the following figures will be presented some screenshots of the main parts of the model of the hybrid MMC that has been developed with the Simulink software.

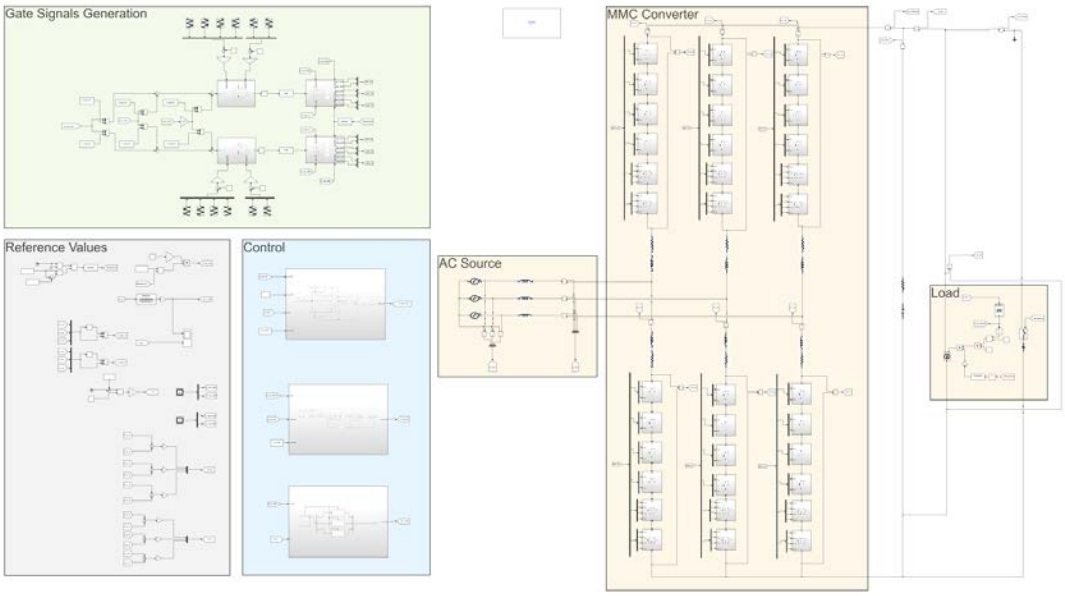

Figure A.1: Overall view of the model.

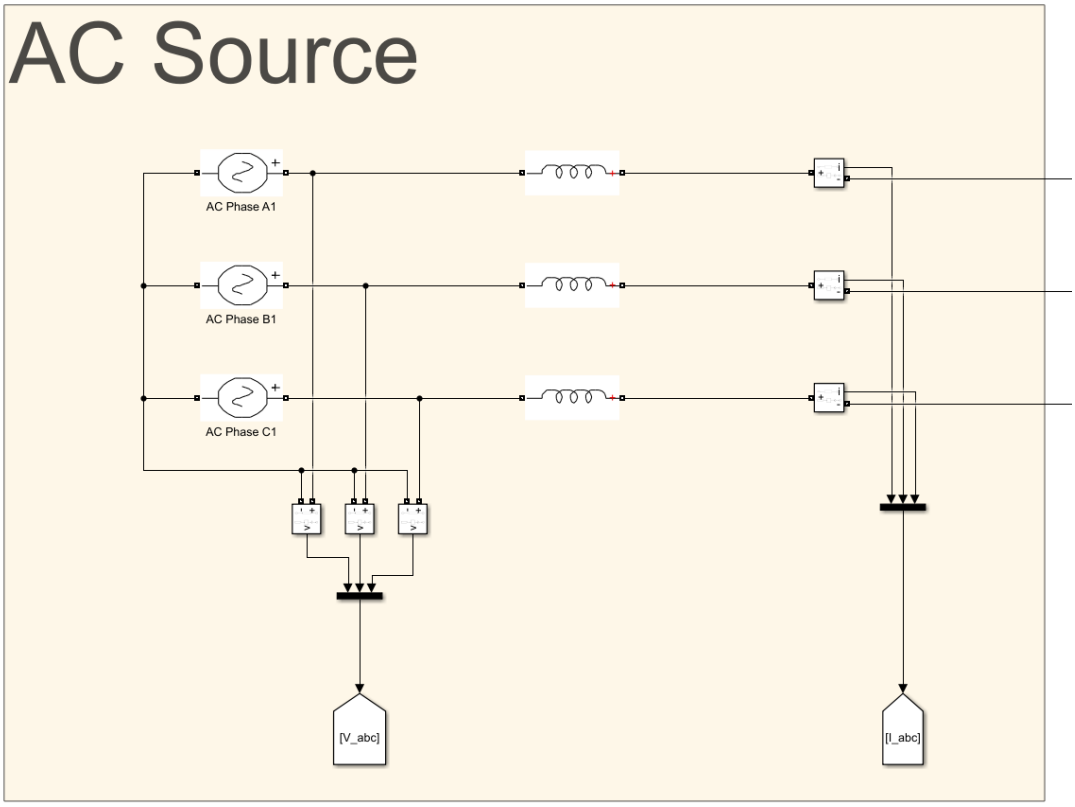

Figure A.2: View of the AC source.

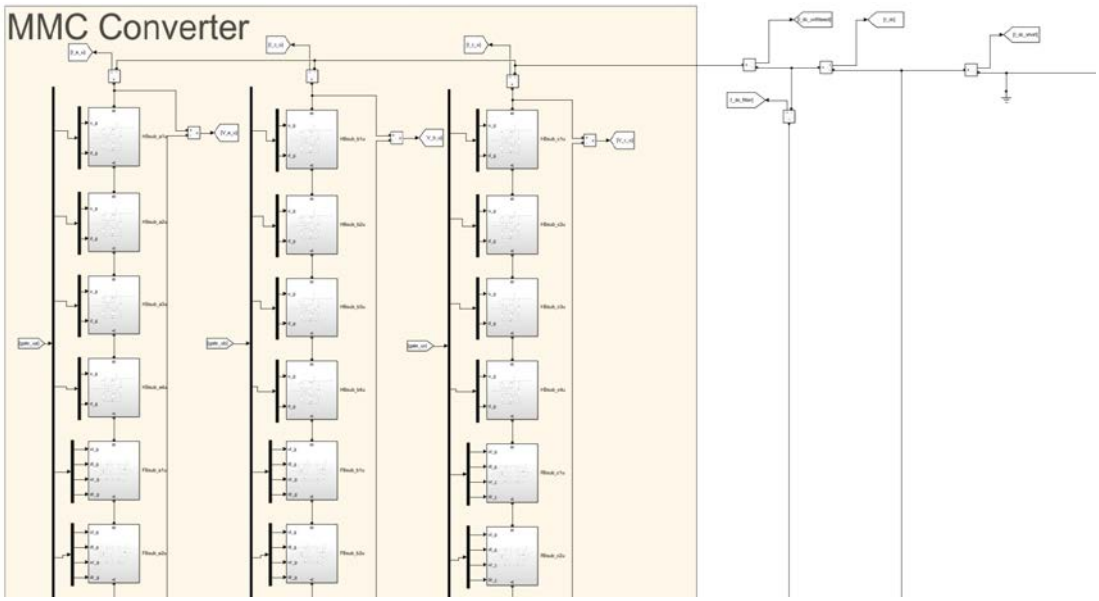

Figure A.3: View of the upper arm of the converter.

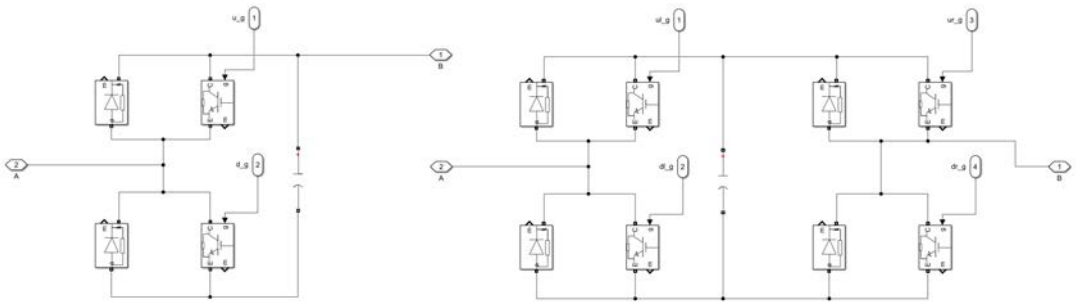

Figure A.4: View of the HB and FB submodules, respectively on the left and on the right.

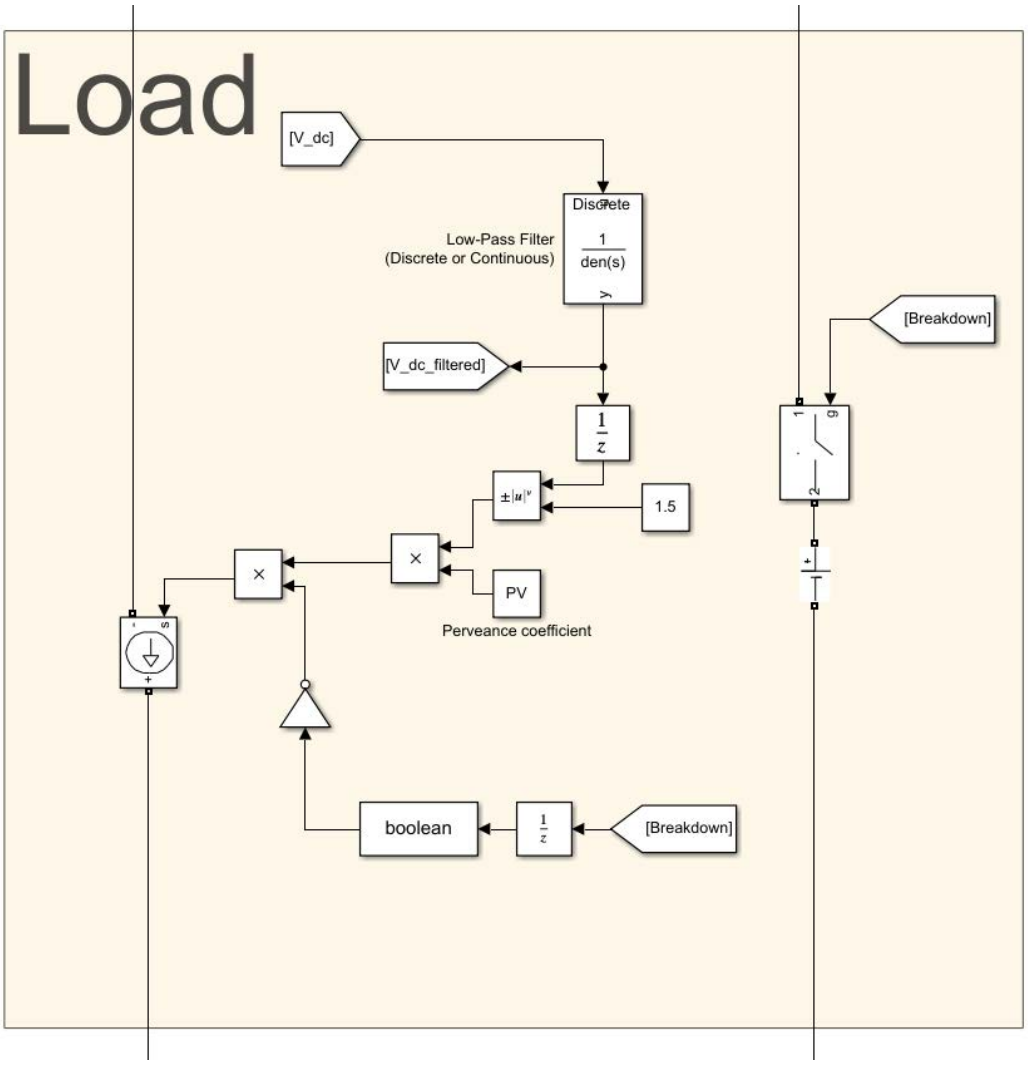

Figure A.5: View of the load.

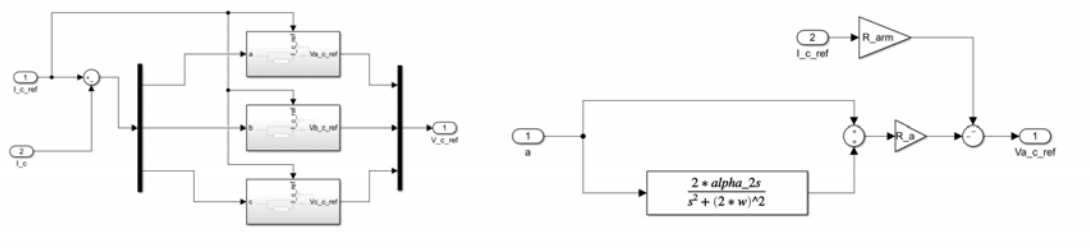

Figure A.6: View of the circulating current control.

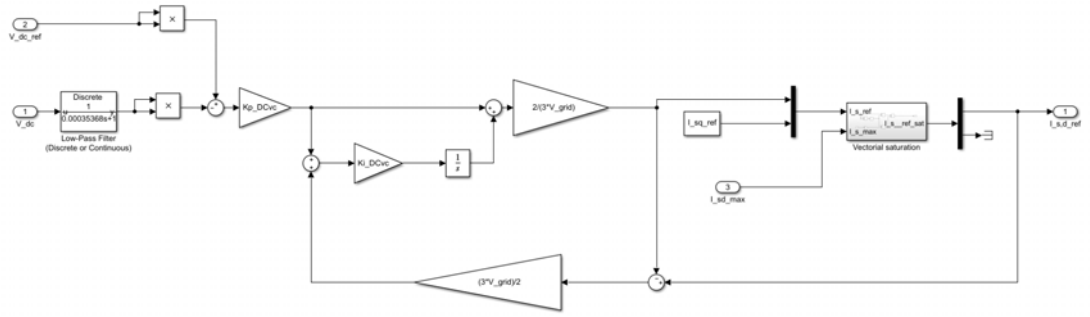

Figure A.7: View of the DC-bus current control.

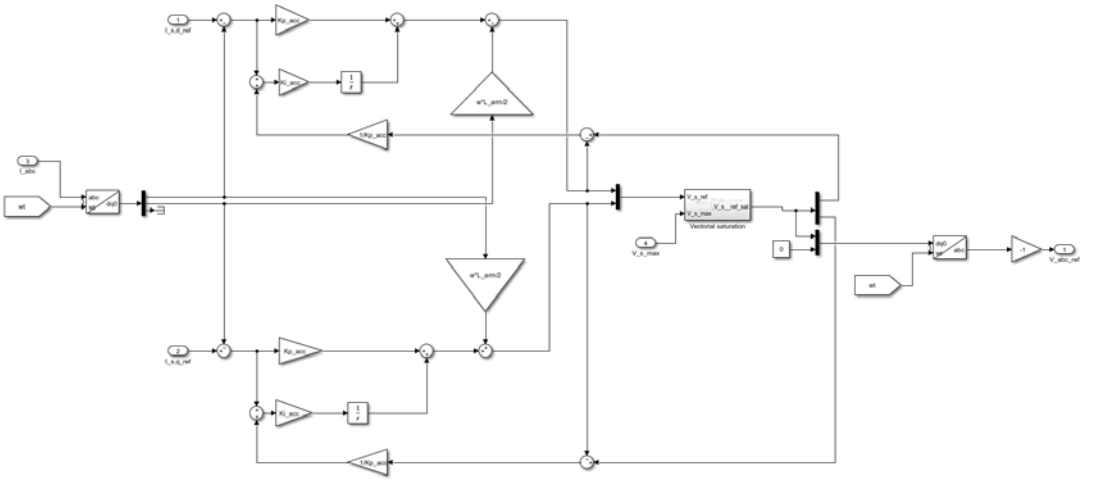

Figure A.8: View of the AC current control.

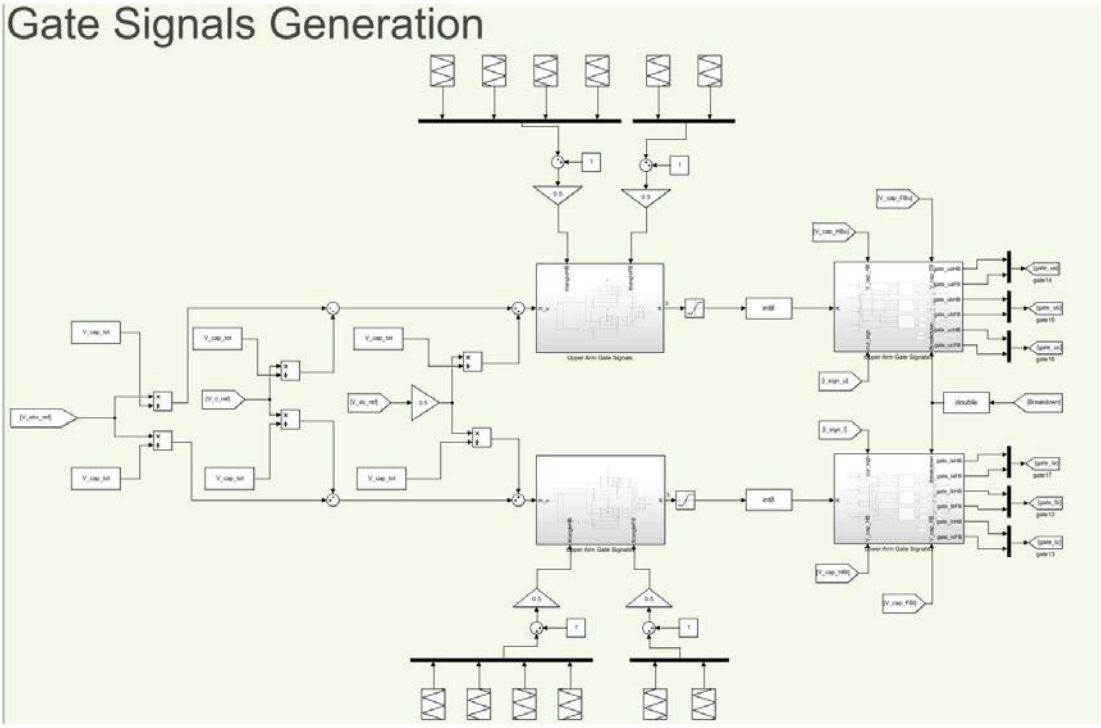

Figure A.9: View of the gate signal generator.

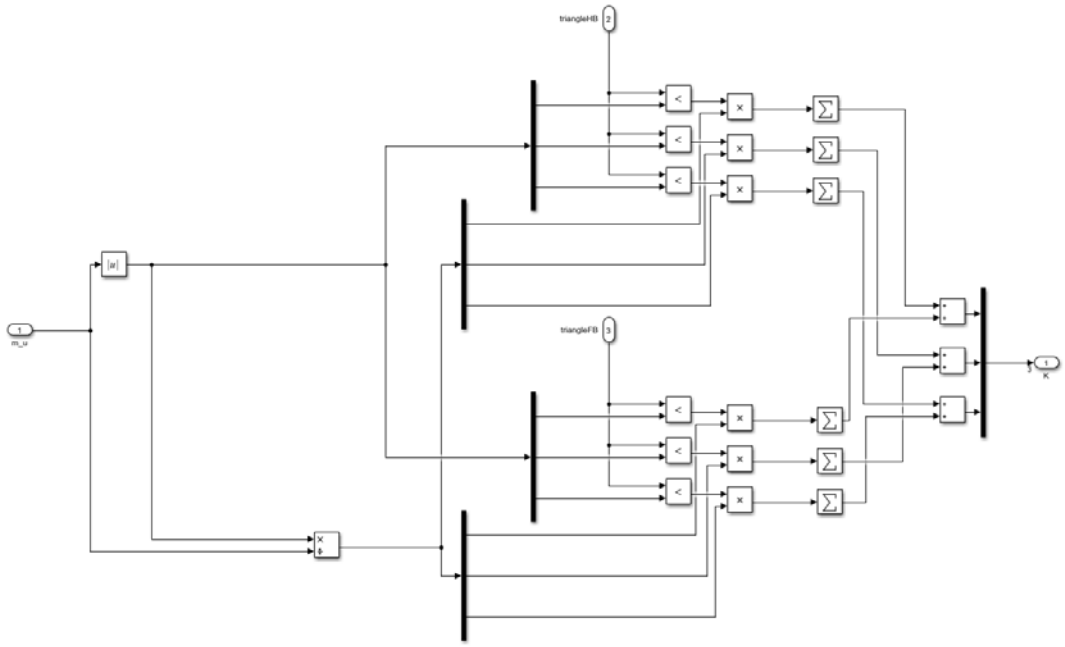

Figure A.10: View of the PS carrier modulation.

Bibliography

[1] J. P. Freidberg. *Plasma physics and fusion energy*. Cambridge university press, 2008.

[2] J. Wesson. *Tokamaks*. Clarendon Press, 2004.

[3] R. Pitts, R. Buttery and S. Pinches. "Fusion: the way ahead". In: *Physics World* 19.3 (Mar. 2006), pages 20–26.

[4] URL: www.euro-fusion.org.

[5] URL: www.iter.org.

[6] A. Mimo. "Optimization of Caesium Dynamics in Large and Powerful RF Sources for Negative Hydrogen Ions". PhD thesis. Universität Augsburg, 2018, page 152.

[7] R. Hemsworth and T. Inoue. "Positive and negative ion sources for magnetic fusion". In: *IEEE Transactions on Plasma Science* 33 (2005), pages 1799–1813.

[8] A. Ferro. "Study of the power supply system for the acceleration grids of the ITER Neutral Beam Injector". PhD thesis. Università degli Studi di Padova, Jan. 2011.

[9] M. Shimada et al. "Chapter 1: Overview and summary". In: *Nuclear Fusion* 47.6 (June 2007), S1–S17.

[10] R. S. Hemsworth et al. "Overview of the design of the ITER heating Neutral Beam Injectors". In: *New Journal of Physics* 19.2 (Feb. 2017), page 025005.

[11] V. Toigo et al. "The PRIMA Test Facility: SPIDER and MITICA test-beds for ITER Neutral Beam Injectors". In: *New Journal of Physics* 19.8 (Aug. 2017), page 085004.

[12] E. Gaio et al. "The alternative design concept for the ion source power supply of the ITER Neutral Beam Injector". In: *Fusion Engineering and Design* 83.1 (2008), pages 21–29. ISSN: 0920-3796.

[13] L. Zanotto et al. "Final design of the acceleration grid power supply conversion system of the MITICA Neutral Beam Injector". In: *Fusion Engineering and Design* 123 (2017). Proceedings of the 29th Symposium on Fusion Technology (SOFT-29) Prague, Czech Republic, September 5-9, 2016, pages 376–380. ISSN: 0920-3796.

[14] L. Zanotto, A. Ferro and V. Toigo. "Assessment of performance of the acceleration grid power supply of the ITER Neutral Beam Injector". In: *Fusion Engineering and Design* 84.7 (2009). Proceeding of the 25th Symposium on Fusion Technology, pages 2037–2041. ISSN: 0920-3796.

[15] D. Ratti. "Application of Modular Multilevel Converter technology to HV power supplies of Neutral Beam injector". Master's thesis. Università degli Studi di Padova, Sept. 2019.

[16] *DTT Divertor Tokamak Test facility. Interim Design Report. A milestone along the roadmap to the realisation of fusion energy*. ENEA, May 2019. URL: www.dtt-dms.enea.it/share/s/avvglhVQT2aSkSgV9vuEtw.

[17] R. Ambrosino. "DTT - Divertor Tokamak Test facility: A testbed for DEMO". In: *Fusion Engineering and Design* 167 (2021), page 112330. ISSN: 0920-3796.

[18] P. Agostinetti et al. *Technical summary of the injector for the DTT NBI system*. Technical report NBI-TEC-54000_1.0. DTT S.c.a.r.l., 2021.

[19] A. Ferro et al. *Conceptual design of the power supplies for DTT Neutral Beam Injector*. In: *Fusion Engineering and Design*, under review. 31st edition of the Symposium on Fusion Technology (SOFT 2020) 20-25 September, 2020.

[20] T. Donné and W. Morris. *European Research Roadmap to the Realisation of Fusion Energy. EUROfusion Programme Management Unit*. 2018.

[21] J. Qin et al. "Hybrid design of modular multilevel converters for HVDC systems based on various submodule circuits". In: *IEEE Transactions on Power Delivery* 30.1 (2014), pages 385–394.

[22] X. Yu, Y. Wei and Q. Jiang. "New submodule circuits for modular multilevel current source converters with DC fault ride through capability". In: *2016 IEEE Applied Power Electronics Conference and Exposition (APEC)*. IEEE. 2016, pages 1468–1474.

[23] K. Sharifabadi, L. Harnefors et al. *Design, control, and application of modular multilevel converters for HVDC transmission systems*. John Wiley & Sons, 2016.

[24] G. J. M. de Sousa. "Estudo de conversores modulares multiníveis (MMC) uni-e bidirecionais". Universidade Federal de Santa Catarina, Florianópolis, 2014.

[25] G. J. M. de Sousa and M. L. Heldwein. "Modular multilevel converter based unidirectional medium/high voltage drive system". In: *IECON 2013-39th Annual Conference of the IEEE Industrial Electronics Society*. IEEE. 2013, pages 1037–1042.

[26] G. J. M. de Sousa and M. L. Heldwein. "Three-phase unidirectional modular multilevel converter". In: *2013 15th European Conference on Power Electronics and Applications (EPE)*. IEEE. 2013, pages 1–10.

[27] R. Zeng et al. "Design and operation of a hybrid modular multilevel converter". In: *IEEE Transactions on power electronics* 30.3 (2014), pages 1137–1146.

[28] W. Lin et al. "Full-Bridge MMC Converter Optimal Design to HVDC Operational Requirements". In: *IEEE Transactions on Power Delivery* 31.3 (2016), pages 1342–1350.

[29] C. Xu et al. "An Improved Phase-Shifted-Carrier Technique for Hybrid Modular Multilevel Converter With Boosted Modulation Index". In: *IEEE Transactions on Power Electronics* 35.2 (2020), pages 1340–1352.

[30] J. Jung et al. "A New Topology of Multilevel VSC Converter for a Hybrid HVDC Transmission System". In: *IEEE Transactions on Power Electronics* 32.6 (2017), pages 4199–4209.

[31] URL: search.abb.com/library/Download.aspx?DocumentID=5SYA%201456&$LanguageCode=en&DocumentPartId=&Action=Launch.

[32] R. Marquardt et al. "Modulares stromrichterkonzept für netzkupplungsanwendung bei hohen spannungen". In: *ETG-Fachtagung, Bad Nauheim, Germany* 114 (2002).

[33] S. Debnath et al. "Operation, Control, and Applications of the Modular Multilevel Converter: A Review". In: *IEEE Transactions on Power Electronics* 30.1 (2015), pages 37–53.

[34] Y. Li, E. A. Jones and F. Wang. "Circulating Current Suppressing Control's Impact on Arm Inductance Selection for Modular Multilevel Converter". In: *IEEE Journal of Emerging and Selected Topics in Power Electronics* 5.1 (2017), pages 182–188.

[35] URL: www.mathworks.com.